Thesis Plague.pdf

Delhi Technological University

Document Details

Submission ID
trn:oid:::27535:120349869

Submission Date
Nov 8, 2025, 10:15 PM GMT+5:30

Download Date
Nov 8, 2025, 10:18 PM GMT+5:30

File Name
Thesis Plague.pdf

File Size
7.6 MB

140 Pages

28,802 Words

170,033 Characters

2% Overall Similarity

The combined total of all matches, including overlapping sources, for each database.

Filtered from the Report

- Bibliography
- Small Matches (less than 14 words)

Exclusions

- 6 Excluded Sources

Match Groups

27 Not Cited or Quoted 2%
Matches with neither in-text citation nor quotation marks

0 Missing Quotations 0%
Matches that are still very similar to source material

0 Missing Citation 0%
Matches that have quotation marks, but no in-text citation

0 Cited and Quoted 0%
Matches with in-text citation present, but no quotation marks

Top Sources

1% Internet sources
1% Publications
2% Submitted works (Student Papers)

Integrity Flags

0 Integrity Flags for Review

No suspicious text manipulations found.

Our system's algorithms look deeply at a document for any inconsistencies that would set it apart from a normal submission. If we notice something strange, we flag it for you to review.

A Flag is not necessarily an indicator of a problem. However, we'd recommend you focus your attention there for further review.

Match Groups

- **27** Not Cited or Quoted 2%
  Matches with neither in-text citation nor quotation marks
- **0** Missing Quotations 0%
  Matches that are still very similar to source material
- **0** Missing Citation 0%
  Matches that have quotation marks, but no in-text citation
- **0** Cited and Quoted 0%
  Matches with in-text citation present, but no quotation marks

Top Sources

1% Internet sources
1% Publications
2% Submitted works (Student Papers)

Top Sources

The sources with the highest number of matches within the submission. Overlapping sources will not be displayed.

1	Submitted works	University of Pittsburgh on 2014-07-15 <1%
2	Submitted works	Heriot-Watt University on 2017-03-21 <1%
3	Publication	Elias N. Glytsis. "Optical Science and Engineering", CRC Press, 2025 <1%
4	Publication	Maksym Zhelyeznyakov, Johannes Fröch, Anna Wirth-Singh, Jaebum Noh, Junsuk ... <1%
5	Publication	Ubaid Ur Rahman Qureshi, M Ismail Khan, Bin Hu. "Realizing efficient THz circular... <1%
6	Internet	escholarship.org <1%
7	Internet	www.researchgate.net <1%
8	Publication	Hai Liu, Senhao Duan, Cong Chen, Hongzhong Cui, Peng Gao, Yaowei Dai, Zongya... <1%
9	Submitted works	Cranfield University on 2013-01-07 <1%
10	Submitted works	Monash University on 2025-06-23 <1%

11 Internet

aip.scitation.org <1%

12 Internet

spectrum.library.concordia.ca <1%

1

CHAPTER

Introduction

- *Give introduction of metasurfaces as novel nanophotonic structures featuring emerging potential in controlling in the electromagnetic field by artificial subwavelength inclusions.*
- *Organizes metasurfaces by symmetry in the composition, separating them into polarization-insensitive and polarization-selective types.*
- *Presents the concept of polarization-dependent metasurfaces providing spin-dependent transmission, reflection and absorption of circularly polarized light.*
- *Explores the critical optical processes of dichroism and polarization controlled optical activity which drive the operational performance of asymmetric metasurfaces.*
- *Describes application potentials of the metasurface technology, such as high-sensitive biosensing, polarization-based optical logic, and spin-resolved image projection for secure photonic information processing.*

1.1. Metamaterials:

Metamaterials are artificial arrangements of elements engineered to yield electromagnetic properties not naturally available in materials [1,2]. The unusual behaviour exhibited by metamaterials originates not from the chemical composition, but from the periodic or aperiodic configuration of subwavelength resonant elements called meta-atoms[1,3]. Metamaterials allow significant independence in the design of these structural units and herald a new era of wave control, offering unprecedented ability to create artificial materials with desired value of phase, amplitude, polarization and direction of propagation of light[4,5].

Unlike conventional materials, which are characterized by intrinsic optical parameters such as permittivity (ε) and permeability (μ), metamaterials can be designed to exhibit effective macroscopic parameters, including negative permittivity, negative permeability, or even a negative refractive index. This flexibility has led to transformative applications in controlling light–matter interactions, facilitating functionalities such as negative refraction, superlensing, cloaking, and tailored wavefront manipulation[3,5–7].

1.2. Introduction to Metasurfaces:

The two-dimensional analogue of bulk metamaterials are metasurfaces[8,9]. They are composed of a two-dimensional grating of subwavelength resonators designed to produce sharp and strong variations in the phase, amplitude, and polarization of the incoming electromagnetic waves[10]. Metasurfaces, compared to the 3-D structures, present several merits including the same order of periodicities yet less material losses and easier fabrication process, in particularly at the optical frequencies[8,11].

In metasurfaces, the refraction behaviour is more accurately described by the generalized laws of reflection and refraction, which modify conventional Snell's law by incorporating a spatially varying phase gradient imparted by the metasurface[12]. The generalized refraction condition is given by:

$$n_i \sin\theta_i - n_t \sin\theta_t = \frac{\lambda}{2\pi}\frac{d\varphi}{dx} \tag{1.1}$$

where n_i and n_t represent the refractive indices of the incident and transmitted (or refracted) media, respectively, while θ_i and θ_t denote the corresponding angles of incidence and transmission (or refraction) measured from the normal to the interface and $\frac{d\varphi}{dx}$ represents the imposed phase gradient along the metasurface interface. This equation highlights how metasurfaces enable precise manipulation of wavefront direction, independent of bulk material properties.

By applying generalized boundary conditions, metasurfaces can modulate wavefronts in unconventional ways, enabling applications such as flat lenses (metalenses), beam deflectors, holographic displays, and advanced polarization control devices. Because of their unique structural feature with the ease of scalable fabrication, metasurfaces have played an important role in nano photonics, and are believed to be crucial for future integrated photonic devices[13].

1.3. Historical Development and Negative Refraction:

The chronological progression of these developments, from Veselago's theoretical prediction to the modern realization of metasurfaces, is illustrated in Fig. 1.1. The historical evolution of negative refraction and metasurfaces, began with the theoretical prediction of negative refractive index media by Veselago in 1968[14]. Veselago postulated that materials exhibiting

simultaneous negative values of permittivity ($\varepsilon < 0$) and permeability ($\mu < 0$) would support electromagnetic wave propagation with a negative refractive index ($n < 0$). This would lead to remarkable physical phenomena such as reversed Snell's law, inverted Doppler shift, and reversed Cherenkov radiation[15].

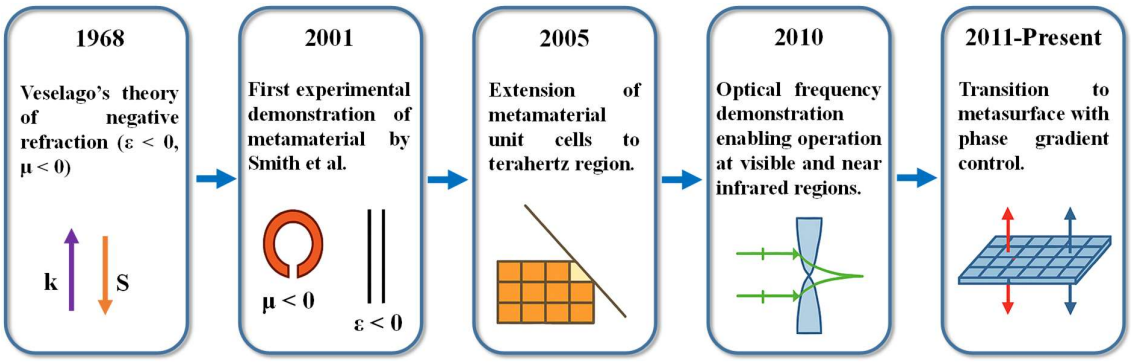

Fig. 1.1 Timeline of Negative Refraction and Metasurface Development.

In conventional positive-index materials (where $\varepsilon > 0$ and $\mu > 0$), the refractive index is given by:

$$n = \sqrt{\varepsilon\mu} \tag{1.2}$$

which yields real and positive values, ensuring forward energy propagation.

In contrast, Veselago proposed that if both ε and μ are negative, the refractive index becomes:

$$n = -\sqrt{|\varepsilon||\mu|} \tag{1.3}$$

Under these conditions, the refracted wave bends to the opposite side of the normal, a phenomenon referred to as negative refraction. Despite the negative sign, the energy flow, represented by the Poynting vector **S**, remains directed away from the interface, while the

wavevector **k** points in the reverse direction[5,15]. This anti-parallel alignment satisfies the relation: $S.k < 0$, which is a defining feature of negative index media.

For decades, negative refraction was considered a theoretical curiosity, as no naturally occurring materials exhibited the necessary electromagnetic properties. This changed in the early 2000s with the advent of artificial metamaterials. Pendry et al introduced structured composites, such as split-ring resonators (SRRs) to achieve negative permeability and metallic wire arrays to produce negative permittivity at microwave frequencies[1]. These meta-atom building blocks enabled the first experimental demonstration of negative refraction by Smith et al. in 2001[2]. Further developments included the operation bandwidth up to the terahertz and optical regimes, downscaling from bulky 3D structures to planar metasurfaces with decreased loss and additional functionality. The idea of negative refraction is still basic to the understanding of light propagation in artificial materials and continues to suggest new photonic devices.

The negative refraction principle is still the cornerstone of wavefront manipulation, and the development of advanced photonic devices. Since Veselago's original proposal, modern platforms like metasurfaces that allow negative refractive indices have led to significant developments in flat optics towards the development of compact lenses, beam deflectors and other wave shaping devices.

1.4. Wave Propagation and Phase manipulation in metasurfaces

The central capability that makes metasurfaces distinct from conventional optical components is their ability to arbitrarily control the spatial distribution of electromagnetic wave characteristics amplitude, phase, and polarization over a subwavelength-thick interface. Unlike

bulky optical elements, where wavefront shaping is achieved through gradual phase accumulation over a propagation distance, metasurfaces realize the same effect (and more) through abrupt phase discontinuities imposed by arrays of engineered subwavelength scattering elements known as meta-atoms[8,10].

Each meta-atom acts as a localized scatterer whose interaction with incident light is governed by its geometry, orientation, and material properties. These parameters dictate the element's complex scattering coefficient, thereby determining the magnitude and phase of transmitted or reflected waves. By spatially varying the scattering response across the metasurface plane, one can directly prescribe the desired transformation of the optical wavefront[9,12].

1.4.1. Interaction of Electromagnetic Waves with Meta-atoms

When a plane wave of wavelength λ is incident on a metasurface, the local response of a meta-atom in transmission and reflection can be described as:

$$t(\lambda) = |t(\lambda)|e^{i\varphi_t(\lambda)}, r(\lambda) = |r(\lambda)|e^{i\varphi_r(\lambda)} \quad (1.4)$$

where, $|t|$ and $|r|$ represents the transmission and reflection amplitudes, and φ_t and φ_r are the corresponding phase shifts imparted to the scattered wave[16].

The underlying physics of wavefront shaping in metasurfaces can be interpreted through Huygens' principle, which states that every point on a wavefront can be considered as a secondary source of spherical wavelets. The new wavefront is formed by the tangential envelope of these secondary waves. In a metasurface, each meta-atom behaves as a *designed Huygens' source*, where the amplitude, phase, and polarization of the emitted wavelets are determined by the meta-atom's geometry, orientation, and material properties[17]. By tailoring both the electric and magnetic dipole moments of each meta-atom, it is possible to satisfy the

so-called Huygens' condition: $E_{forward} >> E_{backward}$, thereby eliminating unwanted backward scattering while enabling complete 0–2π phase coverage in the forward direction.

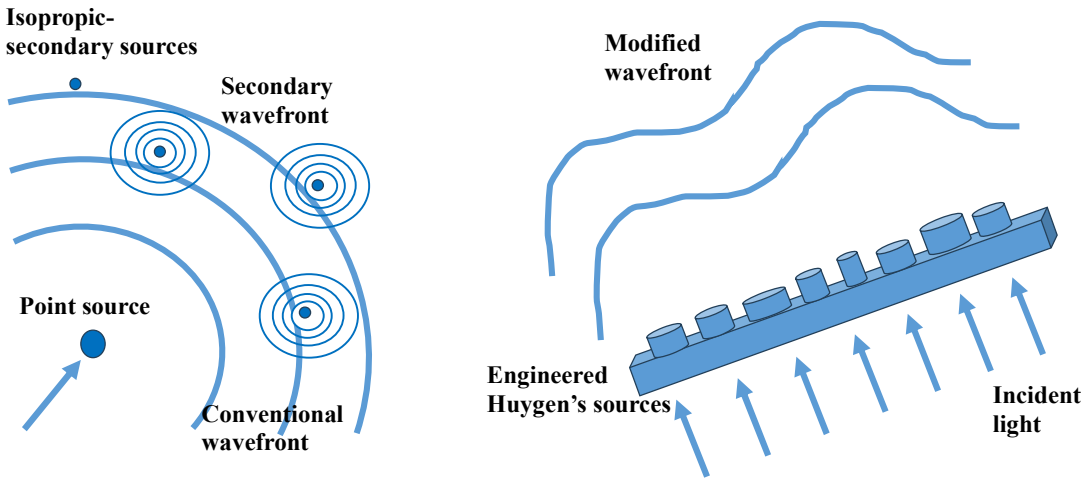

Fig. 1.2 Illustration of Huygens' Principle and Wavefront Manipulation in Metasurfaces

This concept is illustrated schematically in Fig. 1.2, where the left side shows a conventional continuous wavefront with isotropic secondary sources emitting spherical wavelets, and the right side depicts a metasurface in which the isotropic sources are replaced by engineered meta-atoms. These meta-atoms are shown with electric and magnetic dipole moments, producing directional emission that combines to reshape the emerging wavefront. Here, the coordinated phase distribution across the metasurface results in a deflected planar wavefront, in agreement with the generalized Snell's law.

1.4.2. Phase Control Mechanisms

The phase shift imparted by a metasurface can arise from different physical origins, each associated with a distinct method of controlling the optical path or the polarization state. The choice of mechanism depends on the desired bandwidth, polarization sensitivity, and

fabrication constraints of the device. While these mechanisms are conceptually distinct, all rely on precise tailoring of the meta-atom geometry as the primary design variable.

The physical mechanisms responsible for generating these phase shifts fall broadly into three categories: resonant phase control, geometric (Pancharatnam–Berry) phase, and propagation phase[10,18].

1.4.2.1. Resonant Phase Control

Resonant phase control exploits the dispersive nature of localized electromagnetic resonances in meta-atoms. Near the resonance wavelength λ_0, the phase response follows a Lorentzian-like dependence[18]:

$$\varphi(\lambda) = \arctan\left(\frac{\lambda-\lambda_0}{\gamma}\right) \quad (1.5)$$

where γ is the resonance linewidth determined by material absorption and radiation losses.

By varying the dimensions of a plasmonic or dielectric resonator for example, its length, width, or gap size the resonance frequency can be tuned, thereby controlling the phase shift imparted to the incident wave. This approach enables complete 2π phase coverage, but the resulting phase response is inherently wavelength-dependent, making broadband operation challenging without multi-resonant or dispersion-engineered designs.

1.4.2.2. Geometric (Pancharatnam–Berry) Phase

The geometric, or Pancharatnam–Berry (PB), phase mechanism originates from the transformation of the polarization state of light in anisotropic meta-atoms. For circularly polarized incident light, rotating an anisotropic element by an in-plane angle θ imparts a phase shift[16]:

$$\varphi_{PB} = \pm 2\theta \tag{1.6}$$

with the sign determined by the handedness of the incident wave. Unlike resonant phase control, the PB phase is independent of wavelength for a given polarization, as it is purely geometric in nature.

In practice, this mechanism is implemented by arranging identical anisotropic meta-atoms with systematically varying orientations across the metasurface. The PB phase is inherently spin-dependent, enabling functionalities such as polarization-multiplexed holography, spin-controlled beam deflection, and chiral imaging.

1.4.2.3. Propagation Phase Control

In propagation phase control, each meta-atom functions as a truncated optical waveguide, with the imparted phase delay(φ) determined by the accumulated optical path length within the structure[12]:

$$\varphi = \frac{2\pi n_{eff} h}{\lambda} \tag{1.7}$$

where n_{eff} is the effective refractive index of the guided mode, h is the height of the meta-atom, and λ is the operating wavelength.

Adjusting the cross-sectional geometry modifies n_{eff}, while changing the height directly alters the propagation length. This mechanism is particularly effective in high-aspect-ratio dielectric metasurfaces, which offer low loss and broadband phase control, making them ideal for applications such as achromatic metalenses.

1.4.3. Integration of Phase Mechanisms in Design

In practical metasurface implementations, these phase control mechanisms are often combined to exploit their complementary strengths[9,12,19]. A dielectric metalens may primarily utilize propagation phase for broadband focusing, supplemented by resonant phase tuning to correct chromatic aberrations. Similarly, polarization-multiplexed devices may integrate PB phase for spin selectivity with propagation phase for additional dispersion management.

Through careful engineering of the meta-atom's geometry, orientation, and material composition, metasurfaces can achieve near-arbitrary control over wave propagation, enabling multifunctional flat-optical devices that far exceed the capabilities of conventional optics.

1.5. Classification of Metasurfaces

Metasurfaces can be classified according to their structural symmetry, polarization response, operational domain, and phase-control mechanism. Metasurfaces are broadly classified into achiral and chiral types, depending on whether mirror symmetry is preserved or broken. Among these, symmetry plays a pivotal role in determining the interaction of a metasurface with incident light and whether it exhibits chiral optical effects.

1.5.1 Achiral Metasurfaces

Achiral metasurfaces possess mirror symmetry, meaning that their mirror image can be perfectly sup whetheron or translation. In such designs, the optical response remains identical for opposite polarizations, unless deliberate anisotropy is introduced.

A useful analogy can be drawn from natural objects that remain unchanged when reflected in a mirror. For example, a perfectly symmetric bottle or a square tile is identical to its mirror image and can be superimposed without distinction. This principle is illustrated in Fig. 1.3 (a),

where a bottle and its mirror counterpart demonstrate the concept of achiral symmetry. Similarly, achiral metasurfaces are composed of unit cells with high in-plane symmetry, such as squares, circles, or crosses, which exhibit identical optical responses under left- and right-handed circularly polarized (LCP and RCP) light. Owing to this polarization-insensitive behavior, achiral metasurfaces are particularly suitable for applications requiring broadband and uniform phase control, including achromatic metalenses, holographic projection, and beam deflection.

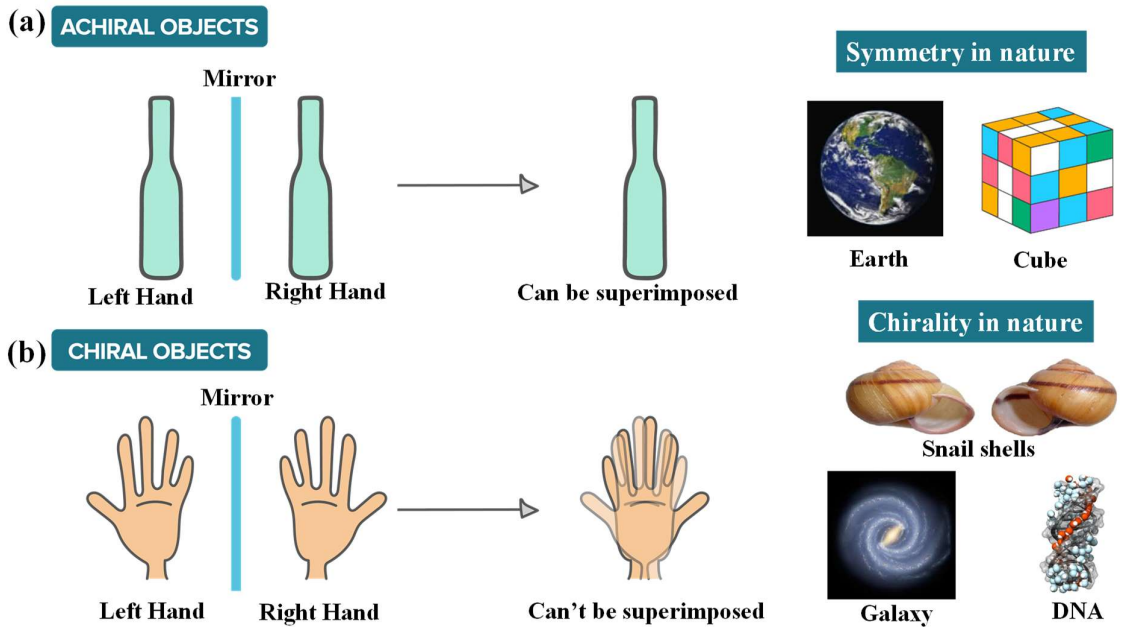

Fig. 1.3. Illustration of achiral and chiral objects with examples. Achiral objects, such as a bottle, remain superimposable on their mirror images, whereas chiral objects, such as human hands, cannot be superimposed on their mirror images. Symmetry and chirality are also abundantly observed in nature, as seen in examples like Earth, crystals, shells, galaxies, and DNA.

In the context of this thesis, the first study demonstrates an achiral metasurface with highly symmetric dielectric meta-atoms, achieving polarization-independent broadband focusing and showcasing the strengths of achiral designs for general-purpose optical manipulation.

1.5.2. Chiral Metasurfaces

Chiral metasurfaces, in contrast to their achiral counterparts, lack mirror symmetry and therefore exhibit distinct optical responses depending on the handedness of incident circularly polarized light. This principle is clearly illustrated in Fig. 1.3 (b), where a human hand and its mirror image cannot be superimposed, demonstrating the essence of chirality. Analogously, chiral metasurfaces are constructed by deliberately breaking the in-plane symmetry of the meta-atoms or their arrangement, thereby inducing enantiomeric sensitivity. Such structures give rise to phenomena including circular dichroism (CD), optical activity (OA), asymmetric transmission, and spin-dependent absorption or emission. The ability of chiral metasurfaces to differentiate between left- and right-handed circular polarizations has positioned them as promising platforms for polarization-sensitive devices, biosensing, optical information encoding, and secure photonic communication[20].

Chiral metasurfaces are further sub-categorized based on their interaction modes. Some designs work in reflection, where a back-reflector layer (often metal) enhances resonant interactions and allows efficient polarization-selective absorption. Other designs operate in transmission, enabling spin-selective filtering or focusing functionalities. Chiral metasurfaces play a vital role in modern photonics, with applications spanning biosensing, enantioselective detection, polarization-controlled imaging, holography, optical security, and information encoding.

1.5.2.1 Polarization Basis

To mathematically describe the chiroptical response, the Jones matrix formalism is widely adopted. In the linear polarization basis, the reflection and transmission matrices are:

$$R = \begin{bmatrix} r_{xx} & r_{xy} \\ r_{yx} & r_{yy} \end{bmatrix}, \qquad T = \begin{bmatrix} t_{xx} & t_{xy} \\ t_{yx} & t_{yy} \end{bmatrix} \tag{1.8}$$

where $r_{xx}(t_{xx})$ (x-polarised to x-polarised) and $r_{yy}(t_{yy})$ (y-polarised to y-polarised) describe co-polarized reflection (transmission) components, and $r_{xy}(t_{xy})$ (y-polarised to x-polarised), $r_{yx}(t_{yx})$ (x-polarised to y-polarised) capture polarization conversion between handedness states.

In the circular polarization basis, they become:

$$R = \begin{bmatrix} r_{RR} & r_{RL} \\ r_{LR} & r_{LL} \end{bmatrix}, \qquad T = \begin{bmatrix} t_{RR} & t_{RL} \\ t_{LR} & t_{LL} \end{bmatrix} \tag{1.9}$$

where $r_{RR}(t_{RR})$ (RCP to RCP) and $r_{LL}(t_{LL})$ (LCP to LCP) describe co-polarized reflection (transmission) components, and $r_{RL}(t_{RL})$ (RCP to LCP), $r_{LR}(t_{LR})$ ((LCP to RCP)) capture polarization conversion between handedness states.

1.5.2.2 Definition of Linear and Circular Dichroism

Chiral metasurfaces are further sub-categorized based on their interaction modes. Some designs work in reflection, where a back-reflector layer (often metal) enhances resonant interactions and allows efficient polarization-selective absorption. Other designs operate in transmission, enabling spin-selective filtering or focusing functionalities.

For structures with negligible transmission, such as metal-backed reflective metasurfaces or absorbers, circular dichroism (CD) is evaluated through the difference in absorptions of right- and left-circularly polarized light as:

$$CD = A_R - A_L \tag{1.10}$$

where A_L and A_R denotes LCP and RCP light absorptions, respectively.

Similarly, linear dichroism (LD) is evaluated through the difference in absorptions of x- and y-polarized light as:

$$LD = A_y - A_x \tag{1.11}$$

where A_x and A_y denotes x and y polarised light absorptions, respectively.

For transmissive or partially transmitting metasurfaces, CD is quantified from the transmitted and reflected intensities as:

$$CD_T = (t_{LL}^2 + t_{RL}^2) - (t_{RR}^2 + t_{LR}^2), \quad CD_R = (r_{LL}^2 + r_{RL}^2) - (r_{RR}^2 + r_{LR}^2) \tag{1.12}$$

Similarly, under linearly polarized excitation, polarization-dependent dichroism can be described as:

$$LD_T = \left(t_{yy}^2 + t_{xy}^2\right) - \left(t_{xx}^2 + t_{yx}^2\right), \quad LD_R = \left(r_{yy}^2 + r_{xy}^2\right) - \left(r_{xx}^2 + r_{yx}^2\right) \tag{1.13}$$

Here, CD_T (LD_T) represents the transmission circular dichroism (linear dichroism), quantifying the difference in total transmitted intensity between LCP and RCP (x and y) illumination, while CD_R (LD_R) denotes the reflection circular dichroism (linear dichroism), capturing the analogous difference in reflected intensity.

Chiroptical responses in metasurfaces originate from asymmetric current distributions and tailored electromagnetic resonances. These include electric dipole, magnetic dipole, and higher-order multipole excitations that couple differently to LCP and RCP light. Structural parameters such as cavity depth, resonator shape, and substrate refractive index critically influence CD magnitude and spectral position. Chiral metasurfaces play a vital role in modern

photonics, with applications spanning biosensing, enantioselective detection, polarization-controlled imaging, holography, optical security, and information encoding.

1.5.3 Types of Chirality in Metasurfaces

Chirality in metasurfaces can be broadly classified into intrinsic and extrinsic categories based on its origin:

1.5.3.1 Intrinsic Chirality

Intrinsic chirality arises from the inherent lack of mirror symmetry within the structure of individual meta-atoms or the overall unit cell. Such structures remain chiral irrespective of the angle of incidence. Intrinsic chirality can be categorized as either three-dimensional or two-dimensional. 3D intrinsic chirality occurs in volumetric structures, such as helical configurations or twisted bilayer metastructures, where asymmetry exists in all three spatial dimensions. In contrast, 2D intrinsic chirality is observed in planar metasurfaces whose meta-atoms lack in-plane mirror symmetry, as seen in gammadion-shaped or L-shaped designs. These planar metasurfaces exhibit chiral responses even at normal incidence, enabling strong circular dichroism within compact geometries.

1.5.3.2 Extrinsic Chirality

Extrinsic chirality emerges from the specific orientation between the metasurface and the incident electromagnetic wave. Even metasurfaces with geometrically symmetric unit cells can exhibit chiral optical responses if illuminated at an oblique angle or with broken symmetry in the surrounding environment (such as different superstrate and substrate materials). In such configurations, the oblique incidence creates a perceived asymmetry in the interaction

geometry, giving rise to asymmetric polarization responses like extrinsic circular dichroism (ECD).

Extrinsic chirality provides design flexibility since polarization selectivity can be dynamically controlled by adjusting the incidence angle or surrounding medium properties without altering the physical metasurface geometry.

This thesis demonstrates examples of both intrinsic and extrinsic chirality. The dielectric metalens (Chapter 2) remains polarization-insensitive due to its symmetry, while the remaining chapters explore various chiral metasurface architectures covering both reflection and transmission configurations, exploiting symmetry breaking, resonance engineering, and wave incidence configuration to achieve polarization-selective functionalities.

1.6 Practical Applications of Metasurfaces

Building on their unique ability to precisely tailor electromagnetic responses at the subwavelength scale, metasurfaces have emerged as a transformative technology with wide-ranging applications across both fundamental research and applied photonic systems. A key area of advancement involves the replacement of bulky, conventional optical components with

compact and planar alternatives. Metasurface-based flat optics have enabled the realization of ultrathin lenses, beam deflectors, and holographic elements capable of high-efficiency wavefront shaping, broadband achromatic focusing, and complex image formation in the visible and near-infrared spectral ranges[16,21]. In parallel, their ability to support strong localized resonances and enhanced light–matter interaction has been extensively utilized in the field of optical sensing, where metasurfaces serve as sensitive transducers for chemical and

biological detection, capable of identifying minute changes in refractive index or absorption signatures[22].

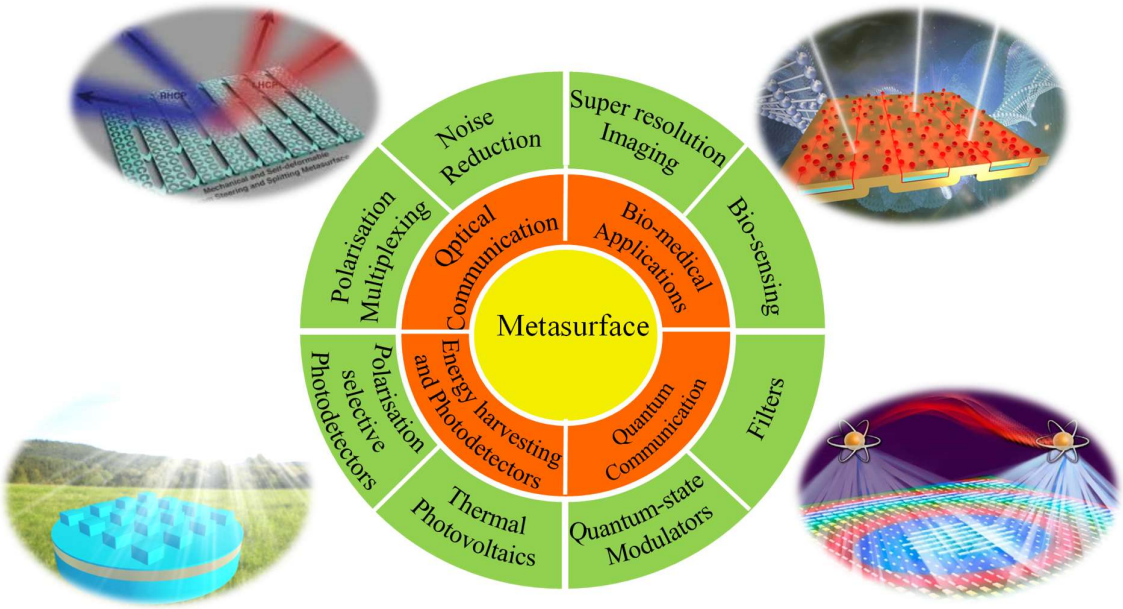

Fig. 1.4 Broad Spectrum of Applications Enabled by Optical Metasurfaces

Another critical application domain involves the use of metasurfaces for polarization and spin control. By introducing structural asymmetry or tailored anisotropy, metasurfaces facilitate selective manipulation of light's polarization state, leading to the development of advanced polarization filters, spin-dependent beam routing elements, and polarization-encoded optical information processors[23,24]. Beyond these static functionalities, recent research has focused on dynamic and reconfigurable metasurfaces, where external stimuli such as electrical bias, thermal tuning, or phase-change materials enable active modulation of optical responses, fostering innovations in tunable lenses, beam steering devices, and dynamic holography[25,26]. Furthermore, metasurfaces have been successfully integrated into security and encryption systems, where polarization- and wavelength-specific responses allow for

controlled concealment or selective projection of optical patterns, contributing to secure data encoding and anti-counterfeiting technologies[27]. The convergence of multifunctionality, compactness, and design flexibility firmly establishes metasurfaces as a pivotal technology in the advancement of next-generation photonic systems, spanning applications in imaging, sensing, information processing, and optical communication.

1.7 Objectives of the thesis:

The objectives of the thesis are as follows:

- To design a dielectric concentric-cylinder metasurface inspired by the human eye for broadband, polarization-independent achromatic focusing.
- To study and develop a metal–perovskite–metal metasurface exhibiting both linear and circular dichroism for polarization discrimination.
- To realize a triple-band perovskite-based metasurface biosensor with high sensitivity.
- To implement a metasurface-based optical chiral encoder for wide-range polarization-encoded information processing.
- To integrate metalens and circular dichroism principles for secure polarization-multiplexed focusing and background suppression.
- To design meta-coded firewall for polarization-selective image projection enabling object concealment and friend–foe identification.

To achieve the above objectives, this thesis is divided into eight chapters, each focusing on a particular stage of the research. The chapters are arranged in a logical sequence, beginning with the fundamentals of metasurfaces and gradually progressing toward advanced chiral designs and their practical applications. This flow ensures a smooth transition from achiral to chiral metasurfaces, covering both reflective and transmissive configurations.

Chapter 1 introduces the fundamental concepts underlying metamaterials and metasurfaces, tracing their historical development from Veselago's theory of negative refraction to the advent of planar metasurfaces. It discusses the classification of metasurfaces based on symmetry, distinguishing between achiral designs that exhibit polarization-insensitive responses and chiral designs that enable spin-dependent transmission, reflection, and absorption. The chapter also emphasizes key optical processes such as circular dichroism (CD), linear dichroism (LD), and polarization-controlled optical activity, which serve as the foundation for the subsequent chapters. Finally, it highlights the wide-ranging applications of metasurfaces in areas such as biosensing, optical logic, quantum communication, and secure information projection.

Chapter 2 establishes the first design platform by presenting an achiral dielectric metalens inspired by the optical structure of the human eye. Using concentric cylindrical dielectric resonators, the proposed lens achieves full 2π phase coverage with reduced aspect ratio, mitigating fabrication challenges commonly associated with high-aspect-ratio dielectric metasurfaces. Comparative modelling across different dielectric core materials (GaN, GaP, and SiO_2) demonstrates optimized performance in terms of phase control, transmission, and focusing efficiency. The chapter further shows the achromatic focusing capability of the design in the near-infrared regime, validating its potential for robust flat-optics integration. This work positions achiral metasurfaces as scalable solutions for lensing and imaging systems, providing a natural transition to more complex chiral structures in subsequent chapters.

Chapter 3 marks the beginning of the exploration of chiral metasurfaces, focusing on extrinsic chirality induced under oblique incidence. A multilayer metal–perovskite–metal (MPM)

absorber is designed to achieve simultaneous circular and linear dichroism. By leveraging polarization-dependent resonant cavity excitation, the structure supports tunable chiroptical responses without altering the physical geometry. Results confirms the interplay between mirror-symmetry breaking and polarization-dependent absorption, resulting in distinct CD and LD peaks. The integration of perovskite, with its tunable refractive index and strong absorption, enhances light–matter interaction and provides flexibility for functional design. This chapter establishes oblique-incidence chiral metasurfaces as versatile candidates for polarization-sensitive applications.

Chapter 4 advances this direction by presenting a triple-band perovskite-based chiral metasurface that functions as a multifunctional biosensor. Through careful engineering of pseudo-starfish-shaped resonators and embedded resonant cavities, the device achieves strong CD at three distinct wavelengths spanning the visible, near-infrared (NIR), and mid-infrared (MIR) regimes. Each band is demonstrated for a specific biosensing application: hemoglobin concentration detection in blood in the visible range, glucose sensing in aqueous solutions in the NIR, and cancer cell identification in the MIR. The analysis of refractive index sensitivity confirms high values exceeding 2000 nm/RIU for cancer detection, demonstrating the exceptional potential of chiral metasurfaces in biomedical diagnostics. By integrating CD-based chiral sensing with resonance tunability, this chapter highlights the ability of metasurfaces to combine multi-band operation and multifunctionality within a single compact platform.

Chapter 5 transitions from extrinsic to intrinsic chirality by addressing the challenge of achieving strong CD under normal incidence. A chiral metasurface composed of concentric semi-circular rings of varying height is introduced. The structure achieves near-perfect

absorption (>99%) at 1510 nm and a maximum CD value of 0.81, demonstrating broadband operation across the S and C communication bands. Importantly, the metasurface exhibits remarkable angular stability, retaining high CD values over incidence variations from –25° to +25° and across wide azimuthal ranges. Additionally, a 4×4 array combining the structure with its mirror image is employed to demonstrate secure image encryption, where spin-selective light reveals or conceals patterns. This chapter underscores the feasibility of achieving robust chiroptical performance under normal incidence, a key requirement for practical communication and imaging applications.

Chapter 6 builds upon this concept by combining chiral metasurfaces with metalens functionality to realize a reflective spin-multiplexed metalens. The proposed design employs enantiomeric Ω- and mirror-Ω-shaped resonators within an Au–SiO_2–Au trilayer architecture. This configuration achieves spin-selective focusing, directing left- and right-circularly polarized beams into distinct focal spots at spatially separated locations, while suppressing background contributions. Numerical simulations confirm high diffraction efficiencies exceeding 75% for both spin channels, stable across a broad mid-infrared spectral range. The device further demonstrates dual-beam operation under mixed polarization input, supporting polarization-multiplexed imaging and secure optical communication. By integrating spin-selective absorption, polarization conversion, and wavefront shaping into a compact reflective platform, this chapter demonstrates multifunctionality in a single metasurface device.

Chapter 7 culminates the thesis by presenting a transmission-based chiral metasurface for secure authentication and information concealment. Unlike previous reflection-based architectures, this all-dielectric meta-coded firewall employs a 41×41 array of double-sided chiral resonators. The metasurface transmits LCP light across a wide spectral range but reflects

it narrowly at 1250 nm, while RCP light transmits nearly unimpeded except for reflection at 1239 nm. This dual resonance generates two CD peaks of opposite chirality, enabling spin-dependent optical gating. By encoding a "V"-shaped pattern within the metasurface, selective visualization is achieved: the pattern appears only under specific polarization–wavelength conditions, remaining concealed otherwise. Furthermore, integration with graphene introduces tunable control through Fermi energy modulation, allowing dynamic switching between visibility states. This chapter establishes a programmable, reconfigurable optical firewall for applications in secure tagging, friend-or-foe identification, and photonic encryption.

Chapter 8 concludes with a summary of contributions and future outlook. Emphasis is placed on integrating active and nonlinear materials for tunable operation, scalable fabrication for large-area deployment, and potential extensions toward quantum communication and adaptive biomedical sensing.

Overall, the chapters together present a complete study that begins with the basic understanding of metasurfaces and extends to their real-world applications in polarization control, sensing, and secure optical communication. The progression from achiral to chiral and from reflection-based to transmission-based metasurfaces highlights the versatility and growing potential of these structures in modern photonic technologies.

2

CHAPTER

Design and Modeling of Human Eye Inspired Metalens

- *This chapter presents the concept, design methodology, and modelling of a dielectric metalens inspired by the optical architecture of the human eye.*
- *It introduces the design principle of concentric cylindrical meta-atoms aimed at reducing aspect ratio while maintaining complete 2π phase coverage.*
- *The chapter discusses comparative performance analysis for different inner core materials (GaN, GaP, SiO_2) with respect to transmission, phase response, and focusing efficiency.*
- *It highlights the achromatic focusing behavior of the designed metalens in the near-infrared regime, along with its potential advantages for robust and scalable flat-optics applications.*

2.1 INTRODUCTION:

The rapid advancement of flat optics has positioned metasurfaces as a compelling alternative to conventional bulky optical components. Unlike refractive lenses, which rely on gradual phase accumulation through material thickness, metasurfaces enable wavefront manipulation through engineered subwavelength structures. Among the various classes of metasurfaces, achiral dielectric configurations are particularly advantageous for imaging applications where polarization-independent performance is essential, making them well suited for designing efficient and broadband metalenses.

In the rich fabric of nature's design, the eyes of certain insects and animals stand out as remarkable examples of optical sophistication. Compound eyes, composed of numerous individual lenses known as ommatidia [28], allow these creatures to perceive their surroundings as a mosaic of images, with each lens capturing a slightly different perspective. These natural optical architectures have long inspired scientists and engineers to investigate new ways of controlling and manipulating light. Building upon these inspirations, a groundbreaking technology known as the metalens has emerged in recent years. Unlike conventional bulky refractive lenses, metalenses are flat, ultrathin devices constructed from carefully engineered nanostructures that impose designed phase shifts on incident light. Lin et al. [29] first demonstrated a silicon nanorod-based dielectric gradient metasurface in 2014, implementing phase control through the Pancharatnam–Berry phase [30,31] and propagation phase principles [32–34]. Much like the compound eyes of insects, the functionality of a metalens arises from the collective behaviour of its unit cells, which are arranged in specific patterns to shape the wavefront of light with high precision.

Over the past decade, metalenses have demonstrated immense versatility in a wide variety of applications[8,33,35–37]. They have been successfully employed in nonlinear dynamics [38], light beam shaping [39–42], high-dimensional holography [43–46], polarization control and analysis [47–49], and even futuristic concepts such as invisibility cloaks [50]. Recent progress has further highlighted the use of symmetry transformations in quadratic phase metasurfaces, enabling planar metalenses to achieve wide fields of view comparable to those of traditional rotationally symmetric lenses [51–53]. Such advancements open up new possibilities for compact imaging devices, portable optical sensors, and wearable displays. The implications of these developments extend far beyond laboratory demonstrations. Potential real-world applications include next-generation medical imaging systems, portable diagnostic tools, advanced virtual and augmented reality (VR/AR) platforms, and ultrathin cameras for consumer electronics. In addition, metalenses hold promise for aerospace and defence applications where size, weight, and efficiency are critical. Despite these remarkable advantages, certain practical limitations persist. One major challenge is the high aspect ratio of the nanostructures, which can lead to fabrication difficulties, structural fragility, and reduced efficiency under mechanical or thermal stress. Balancing fabrication feasibility with optical performance remains a critical area of research. Moreover, integrating metalenses with existing optical platforms requires careful optimization to ensure robustness and scalability.

The amazing fusion of biological inspiration and human invention is revealed as we explore further into the realm of metalenses. Here in this chapter we demonstrate a metalens with human eye mimetic meta-atom. For the first time a metalens is designed with highly reduced and constant aspect ratio giving it higher mechanical stability, ease of integration and also resistance to environmental factors. The designed meta- atom is made up of two concentric

cylinders with outer cylinder made of amorphous Si. For comparison the material of inner core has been varied as GaN, GaP and SiO_2 and their transmission and phase profile characteristics have been studied. Compared with previously reported metalenses, the human eye mimetic metalens shows better focusing efficiency of 52% with highly reduced aspect ratio of as low as 1.4 for a high numerical aperture of 0.4. The designed metalens also eliminates the chromatic aberration for a continuous range of 1300 nm–1500 nm.

2.2 Design principle and theory:

The structural design of proposed unit cell is inspired from human eye. The human eye is a complex optical system with several structures, each with its own refractive index. The refractive indices of these structures play a critical role in bending and focusing light to create a clear image on the retina. It can be considered as a gradient lens with a structure formed from a finite number of shells (nanolayers) where the refractive index of each shell varies from 1.3 to 1.4 [54] as depicted in Fig. 2.1(a).

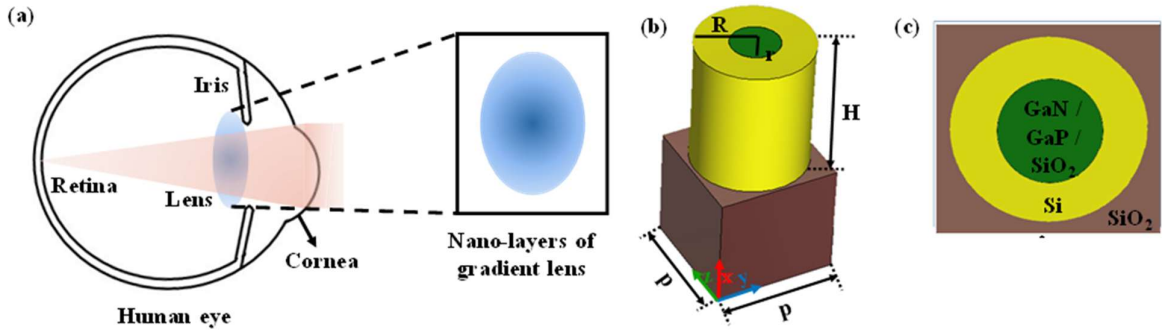

Fig 2.1 Schematic illustration of (a) the single chambered Human eye with graded lens (The inset figure shows the graded lens consisting of nano-layers of different refractive index). (b) Three dimensional view of the metalens unit cell. (c) Top view of the metalens unit cell.

Inspired from the structural design of human eye lens, a meta atom made up of two concentric cylinders of two different materials representing two shells of different refractive indices has been designed. As by taking two concentric shells of different materials the effective refractive index of the meta-atom is increased and thus the height of the meta-atom is highly reduced according to waveguide model $\emptyset = 2\pi n_{eff} H/\lambda_d$, where 'n_{eff}' is the effective refractive index, 'H' denotes the height of meta-atom and 'λ_d' is the incident wavelength[55]. The aspect ratio of our designed meta-atom is highly reduced where the aspect ratio is defined as the ratio of height and minimum radius of the unit cell.

The outer cylinder of the proposed design is made up of amorphous Si (Pierce and Spicer; n = 3.49, k = 0). Three different materials namely GaN (Barker and Illegens; n = 2.32, k = 0), GaP (Adachi; n = 3.13, k = 0) and SiO_2 (Ghosh; n = 1.52, k = 0) have been selected for the inner core of the cylinder which is mounted on SiO_2 substrate as shown in Fig. 2.1(b) and (c) to test their phase response and transmission characteristics. The working wavelength for the designed structure is 1400 nm. For comparative study radius of the outer cylinder is kept constant for all the three different unit cells. The period (p) of the designed meta atom array has been taken to be 832 nm.

Such devices can be experimentally fabricated by photolithography process followed by reactive-ion etching[56–58]. GaN/GaP material can be deposited on SiO_2 substrates using techniques Metal-Organic Chemical Vapor Deposition (MOCVD) or Molecular Beam Epitaxy (MBE) followed by Electron Beam Lithography (EBL) whereas for SiO_2 inner core Chemical Vapor Deposition (CVD) techniques, including Plasma-Enhanced Chemical Vapor Deposition (PECVD) techniques could be used[59,60]. Reactive-ion etching can then be used to etch the inner core material where it is exposed, creating the inner cylinder. These methods allow for

the precise control of the thickness and composition of the inner core material. After this, Silicon can be deposited around the inner core cylinder using Chemical Vapor Deposition (CVD), ensuring uniform coverage around the structure. A second round of EBL, followed by reactive-ion etching, can define the outer dimensions of the Si cylinder.

2.3 Results and Discussion:

The designed structure has been modelled and analysed using the finite element method (FEM) based COMSOL Multiphysics software, where a plane wave is incident on the structure propagating along z-axis. The incident plane wave has electric field polarized along x axis and is incident from substrate side.

The radius of inner cylinder has been swept to cover the complete 2π phase of incident light. Table 2.1 shows the optimised parameters (period 'p', height 'H' and outer radius 'R') of the three different meta-atoms with different inner core materials.

Table 2.1 Parameters of three different concentric cylindrical meta-atoms.

Parameters	Inner Material GaN (nm)	Inner Material GaP (nm)	Inner Material SiO_2 (nm)
p	801	801	801
H	880	1000	935
Outer Radius (R)	304	304	304
Aspect Ratio $(H/2R)$	1.4	1.6	1.5

The comparative normalized transmission and phase response for the wavelength 1400 nm by varying the inner radius of three different meta-atoms keeping the outer radius constant at 304 nm are shown in Fig. 2.2 (a) and (b). The meta-atom with inner core as GaN shows higher normalized transmission with two resonance dips and smooth phase coverage from –π to π.

The meta-atom with inner core as SiO_2 covers the complete phase but with many resonance dips whereas the meta atom with inner core as GaP material shows high transmission but the maximum phase coverage is exhibited for small radius range i.e. 185 nm to 205 nm. Thus meta-atom with inner core material as GaP is not suitable for designing complete metalens structure as the maximum phase variation is seen for small radius range.

The electric field distribution of meta-atom with inner core as GaN for small, medium and large inner core radius are shown in Fig. 2.2 (c), (d) and (e) respectively. The radii for the inner core are taken as 28 nm, 161 nm and 247 nm. The dashed line represents the diameter of inner core represented by 2r. For r = 28 nm and 247 nm i.e. for extreme radii resonance centres on the side surface of the concentric nanopillars and between inner core and outer cylinder. This type of surface resonance results in a significant reduction in transmission efficiency as well as excessive reflection which is induced due to the narrowed gap between adjacent nanopillars. However, for r = 161 nm (intermediate range of r) the high transmission efficiency is achieved which is in agreement with normalized transmission graph shown in Fig. 2.2 (a).

Further, it demonstrates that the human eye mimetic meta-atom with GaN as inner core is highly transmissive and capable of accumulating the 2π phase by effectively reducing the height of the nanopillar and thus highly reducing the aspect ratio of the meta-atom. Further, the aspect ratio of the three designed meta-atoms remains constant at 1.4, 1.6 and 1.5 for inner cylinder material as GaN, GaP and SiO_2 respectively throughout as the outer radius is kept fixed. A comparison of few aspect ratio for various dielectric metalenses used in previous research is shown in Table 2.2.

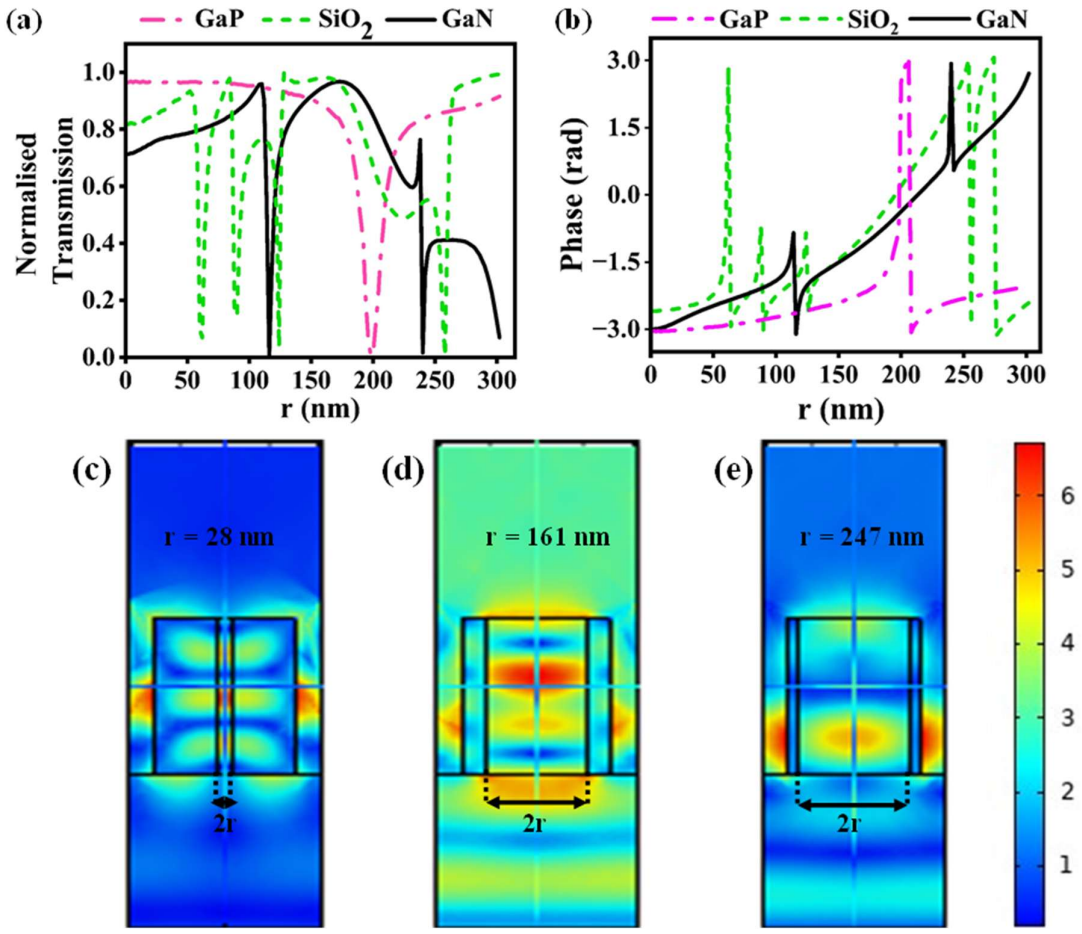

Fig 2.2 Comparative results of (a) Normalised Transmission and (b) phase profile as a function of inner core radius for different meta-atoms. Electric field distributions of meta atom with inner core as GaN for radius (c) r = 28 nm (d) r = 161 nm and (e) r = 247 nm

Table 2.2 Overview of Aspect Ratios for dielectric Meta-atoms

Materials	λ (nm)	Height (nm)	Aspect Ratio	Ref.
α-Si	1310	750	9.4	[61]
SiO_2	633	1500	6	[36]
TiO_2	532/405	600	7.5/10	[62]
TiO_2-Si	632	300	3	[63]
GaN	450	800	5.7	[64]
Si-GaN	1400	880	1.4	This work

The basic purpose of an optical lens is to focus incident light on a specific point. To demonstrate the focusing capability of a human eye mimetic metalens with an inner core constructed of GaN material, the FDTD simulations under x-polarized plane wave illumination have been performed. The diameter (d) of the designed metalens is 23.3 μm with a focal length (f) of 23 μm. A metalens with meta-atom whose inner core is of SiO_2 having the same diameter and focal length (i.e., d = 23.3 μm and f = 23 μm) is also designed. The other parameters are set the same according to the designed meta-atoms as mentioned in Table. 2.1. As shown in Fig. 2.3(a), the building blocks are selected to obtain the functionality that each meta-atom at the position (x) must impart the target phase given[65]:

$$\varphi = \frac{-2\pi}{\lambda}\left(\sqrt{x^2 + f^2} - f\right) \tag{2.1}$$

where 'x' denotes the position of associated meta-atom, 'λ' is the intended wavelength, and 'f' denotes the prescribed focal length set at 23 μm. Fig. 2.3(b) and (c) shows the transmission (red curve) and phase imparted (blue curve) by the 29 meta-atoms selected to design the two different metalens with inner core as GaN and SiO_2 respectively. The working wavelength for designed structure is 1400 nm. By changing the inner radius of nanopillars in relation to their position, it is possible to change the effective index of the propagating mode and achieve the desired phase profile (x, y) with fixed outer radius as 304 nm. The designed metalens shows a high numerical aperture (N.A.) of 0.43, which is calculated using the formula $N.A. = n \sin\left(\tan^{-1} \Re/_f\right)$ where 'n' denotes the refractive index of background , '$\Re$' denotes the radius of designed metalens and 'f' is its focal length.

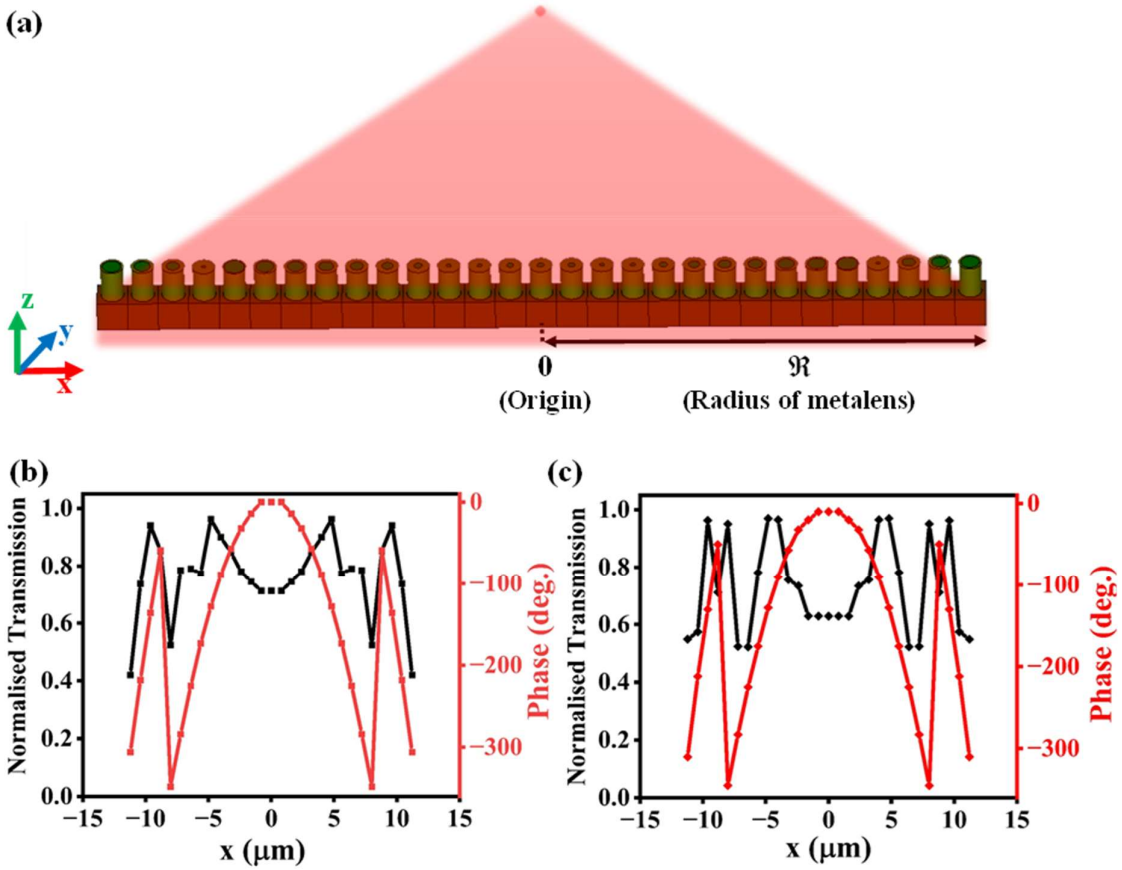

Fig 2.3 (a) Schematic of dielectric metalens in x-z plane made by an array of human eye mimetic meta-atom. Normalised Transmission and phase (deg.) imparted the meta-atoms placed along x-axis for the metalens with inner core as (b) GaN and (c) SiO_2

The focusing results of the designed human eye mimetic dielectric metalens with inner core made of GaN and SiO_2 in x-z plane are shown in Fig. 2.4 (a) and (b) respectively. The designed metalens has been tested for a wide wavelength range of 1300 nm to 1500 nm. In order to detect the chromatic behavior, Fig. 2.4 illustrates their focal spot for wavelengths 1300 nm, 1350 nm, 1400 nm, 1450 nm and 1500 nm. The inset curves in Fig. 2.4 show the normalized intensity profile at each incident wavelength.

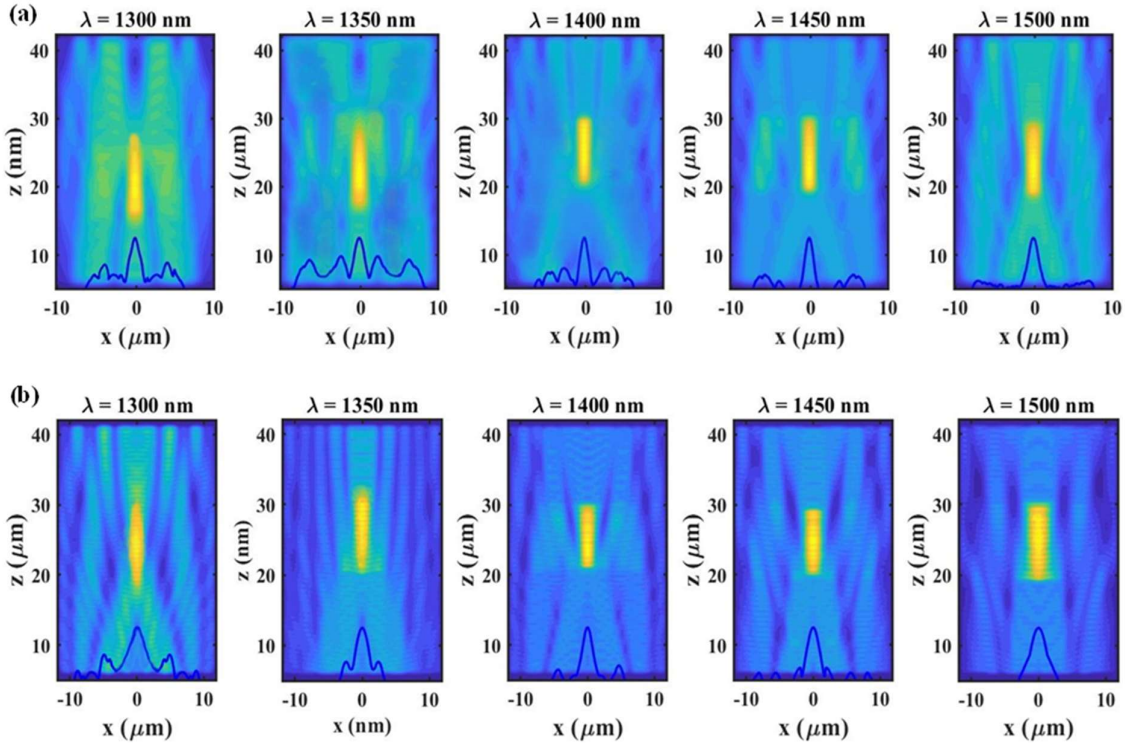

Fig 2.4 Focusing properties and FWHM of the simulated metalens along x-z plane with inner core as (a) GaN and (b) SiO_2 irradiated by incoming light beam of wavelengths 1300 nm, 1350 nm, 1400 nm, 1450 nm and 1500 nm travelling along z direction.

The focal length remains nearly same with the increase in wavelength and hence the designed metalens shows achromatic behavior. Fig. 2.5(a) illustrates the connection between the incoming wavelength and the achromatic focal length. The maximum focal length variation (Δf) over the broadband range for the metalens with inner core as GaN is 1.4 μm whereas for metalens with inner core as SiO_2 is 2 μm. This achromatic behavior could be due to the combined effect of two overlying shells of different refractive index. The focus spots are much brighter and clear with high intensity for the metalens with inner core made of GaN whereas for the metalens with SiO_2 core, the focus spots have minor gaps and have low intensity profile. This could be due to the many dips obtained for the meta-atom with inner core as SiO_2 as shown in Fig. 2.2(a) resulting in sharp decline of transmission efficiency. Also because of the

meta-atoms' circular arrangement and isotropic structure, the achromatic behaviour is independent of the state of the polarisation of the incident light.

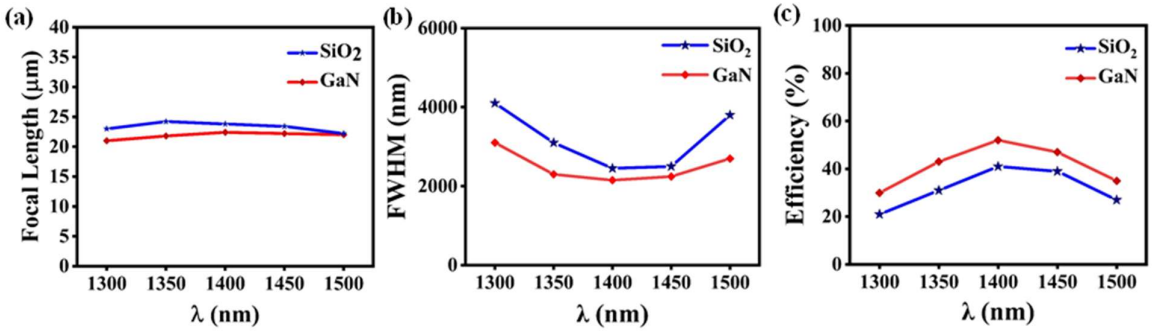

Fig 2.5 (a) Focal length variation with the incident wavelength (b) FWHM of the focus spots and (c) focusing efficiency for the metalens with inner as SiO_2 and GaN for different wavelengths.

As illustrated in Fig. 2.5 (b) and (c), full-width at half-maximum (FWHM) and operational focusing efficiency are assessed at the near-IR region to further investigate the functioning performance of the developed metalens. The observed light intensity is fitted with a Gaussian function along the focus line to determine the FWHM, which is defined as the beam waist of the normalised light intensity at 0.5. All observed FWHMs are in the 1.5λ to 2λ range, which is essentially diffraction limited. The FWHM of metalens with GaN as inner core is 2.15 μm whereas for metalens with inner core as SiO_2 is 2.45 μm for incident wavelength of 1400 nm.

2.4 Summary:

In this chapter, a dielectric metasurface lens inspired by the optical functionality of the human eye has been presented. By employing an achiral concentric-cylinder configuration, the proposed metalens achieves broadband achromatic focusing with high transmission efficiency. The use of dielectric materials minimizes losses compared to plasmonic platforms, while the

concentric arrangement provides a systematic approach for phase compensation across the aperture. The numerical investigations confirm that the metasurface lens reproduces key features of the human eye, such as wide-field focusing and reduced chromatic dispersion, while offering the added benefits of miniaturization and planar integration. These results demonstrate the feasibility of translating natural optical design principles into practical flat-optics implementations. The outcomes of this study highlight the potential of achiral dielectric metasurfaces for a wide range of applications, including compact imaging systems, wearable optics, and biomedical instrumentation. The chapter thus establishes a foundation for extending the concept of biologically inspired metasurfaces toward multifunctional devices, bridging the gap between fundamental physics and practical photonic technologies.

3

CHAPTER

Chiral Perovskite based Metasurface for Circular and Linear Dichroism

- *Introduces chiral metasurfaces with emphasis on oblique-incidence induced extrinsic chirality.*
- *Demonstrates a metal–perovskite–metal (MPM) multilayer design supporting both circular dichroism (CD) and linear dichroism (LD).*
- *Explores the dual dichroic response as a route to polarization-sensitive devices for sensing and information processing.*
- *Highlights the role of perovskite integration in enhancing tunability and light–matter interaction in metasurface*

3.1. INTRODUCTION

In the previous chapter, the emphasis was placed on achiral metasurfaces, which provide polarization-insensitive functionalities such as broadband and achromatic focusing. While such designs are essential for general-purpose light control, they remain limited in their ability to discriminate between different polarization states. To address this limitation, the research focus shifts towards chiral metasurfaces, which introduce polarization selectivity and enable richer forms of light–matter interaction.

Polarization-resolved phenomena such as circular dichroism (CD) and linear dichroism (LD) are of central importance in modern optics, as they underpin applications in molecular spectroscopy, biosensing, communication, and information processing [10,66–68]. In natural systems, these effects are typically weak; however, artificially engineered metasurfaces provide a versatile route to significantly enhance and tailor dichroic responses in ultrathin geometries. By exploiting symmetry breaking, resonance engineering, and anisotropic coupling, metasurfaces can achieve strong polarization-sensitive interactions across designed spectral ranges [69–71].

The core of our investigation is to study and enhance circular as well as linear dichroism in metasurfaces. However, producing significant levels of both linear dichroism (LD) and circular dichroism (CD) in the same structure is challenging due to the intrinsic link between linear and circular polarisation. A range of planar chiral metasurfaces structures have been studied to provide remarkable circular dichroism for polarisation control and characterisation[13,71–77]; nanowire-grid gratings and nanorods have been often used to produce high linear dichroism[78–81]. Through the implementation of various geometric stages, metasurfaces provide a comprehensive range of phenomena of circular dichroism. Unfortunately, the use of

nanostructures is severely limited since a single nanostructure of a particular dimension can only provide a single capability with either linear dichroism or circular dichroism. However, there is still dearth of research in this field, calling for more thorough study.

To realize such functionalities, hybrid architectures combining metals with active or dispersive dielectrics have been increasingly explored. Among these, perovskite materials have emerged as promising candidates owing to their high refractive index, tunable bandgap, and strong optical dispersion [82–86]. Their integration into metasurfaces not only strengthens light–matter interaction but also introduces new degrees of freedom for spectral and polarization engineering.

In this chapter, a Metal-Perovskite-Metal (MPM) based optical chiral absorber that performs differential absorption for the dual wavelength bands of 500-700 nm and 3250-3750 nm has been presented. In order to achieve multifunctionality, the absorber's geometrical design is inspired from a pseudo star fish configuration having eight arms with inbuilt resonant cavities. This structure is unique in the sense that it produces significant dichroism responses to both linearly and circularly polarised photons as it emits two distinct resonances over distinct structural periods. Further the examination of the field distributions inside the resonator structure, provides additional insight into the fundamental mechanism of selective absorption. This work shows it is possible to establish an autonomous control of each resonance wavelength by varying the parameters in the various resonance cavities. With remarkable design freedom, the dual band multifunctional absorber that has been created has the potential to enhance molecular detection and optical switching applications. Ultimately, the extraordinary adaptability of these multifunctional metasurfaces, which enable a seamless combination of circular and linear dichroism in one go, in addition to other functionalities like

beam-steering, phase modulation, and spectral filtering, have the potential to completely transform optical communication systems.

3.2. Structural Design and Theoretical Analysis

The metasurface under investigation is based on a metal–perovskite–metal (MPM) architecture, which serves as the fundamental platform for achieving polarization-selective absorption. The top layer consists of patterned gold resonators arranged in an anisotropic geometry as shown in Fig. 3.1, designed to induce symmetry breaking and enable the excitation of polarization-sensitive modes. Resonant cavities are embedded both within and between the periodic metallic elements, allowing distinct excitation pathways depending on the incident polarization state. By tuning the input polarization, specific resonant channels are activated, giving rise to strong circular and linear dichroism.

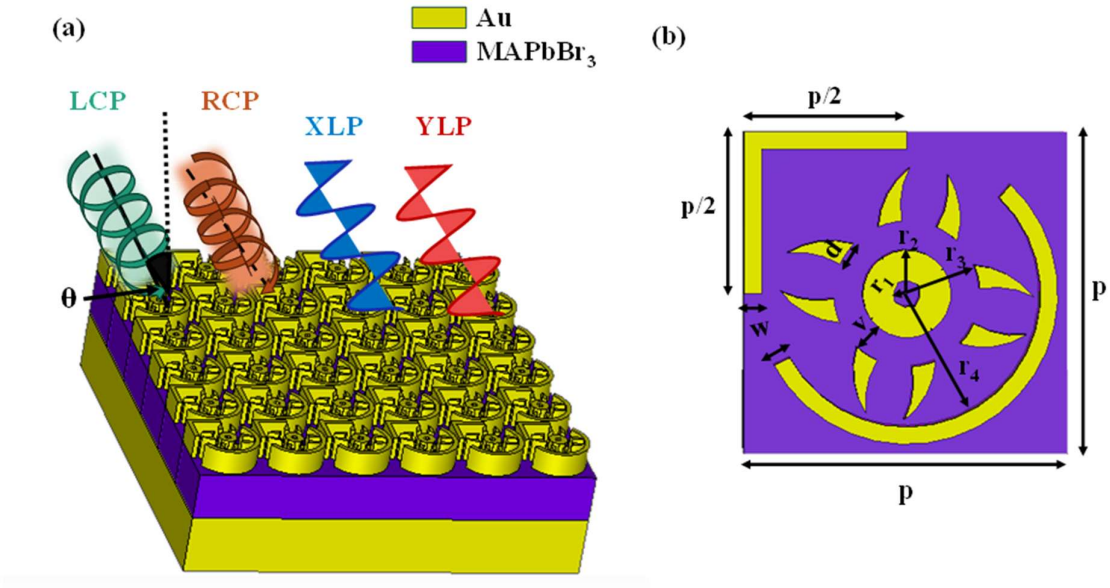

Fig 3.1 (a) Schematic of the proposed MPM based chiral metasurface subjected to LCP, RCP, x-polarised(XLP) and y-polarised(YLP) light (θ=70°) (b) top view of the proposed unit cell.

The designed absorber is composed of three layers: a gold resonator array on the top surface, a perovskite spacer layer of 200 nm thickness, and a continuous gold film of 100 nm thickness is used acting as a back reflector as shown in Fig. 3.1(b). The perovskite material is [Methyl Ammonium lead Tri-bromide($MAPbBr_3$)], with dielectric properties adopted from Ishteev et al. 2022[87], while gold permittivity values are taken from Babar and Weaver (2015) [88]. The unit cell parameters were optimized to period 'p' = 280 nm, width of outer ring 'w' = 15 nm, width of cylindrical cavity 'v' = 20 nm and various radii 'r_1' = 10 nm, 'r_2' = 65 nm, 'r_3' = 85 nm, 'r_4' = 130 nm.

From a fabrication perspective, the proposed structure can be realized using standard nanofabrication processes [86,89,90]. The bottom metallic layer may be deposited using sputtering or thermal evaporation, followed by spin coating to deposit the perovskite film. The top patterned gold resonators can then be fabricated using electron beam lithography (EBL), where the resist is patterned, and gold is deposited to define the meta-atom features.

Numerical modeling was performed in CST Microwave Studio using periodic boundary conditions along the in-plane (x and y) directions, while the z-direction was assigned an open boundary with perfectly matched layers (PMLs). Wave propagation was assumed along the z-axis, and oblique incidence was introduced by varying the angle of excitation. It was found that an incident angle of 70^{o} maximized dichroism, as oblique incidence provides the required extrinsic chirality by breaking additional geometric symmetries of the structure [91]. Since the presence of the metallic backplane suppresses transmission, the analysis was restricted to reflection and absorption characteristics.

The dichroic responses of the metasurface are quantified in terms of linear dichroism (LD) and circular dichroism (CD). LD is defined as the difference in absorption between y- and x-polarized light:

$$LD = A_y - A_x \tag{3.1}$$

where A_y and A_x represent the structure's absorbance for x and y polarised light. The positive value of LD represents more absorption of y-polarised light whereas its negative value shows higher absorption of x-polarised light. The absorptions A_x and A_y may be represented as:

$$A_x = 1 - R_{yx} - R_{xx} \tag{3.2}$$

$$A_y = 1 - R_{xy} - R_{yy} \tag{3.3}$$

here R_{yx} (R_{xy}) denotes the square of cross-polarized reflection coefficient $r_{yx}(r_{xy})$ when the incident light is x polarised(y polarised) whereas R_{xx} (R_{yy}) denotes the square of co-polarized reflection coefficient $r_{xx}(r_{yy})$.

The difference in the absorption of chiral metasurface under two separate rotationally circularly polarised (CP) light sources is referred to as "CD". The formula for computing the coefficient of CD is as follows:

$$CD = A_R - A_L \tag{3.4}$$

where A_L and A_R denotes left circularly polarised (LCP) and right circularly polarised (RCP) light absorptions, respectively. The positive value of CD represents more absorption of RCP light whereas its negative vaue shows higher absorption of LCP light. The chiral metasurface absorption equations are

$$A_L = 1 - R_{RL} - R_{LL} \tag{3.5}$$

$$A_R = 1 - R_{LR} - R_{RR} \tag{3.6}$$

here R_{LR} (R_{RL}) denotes the square of cross-polarized reflection coefficient r_{LR}(r_{RL}) when the incident light is RCP (LCP) whereas R_{RR} (R_{LL}) denotes the square of co-polarized reflection coefficient r_{RR}(r_{LL}).

3.3. Optimisation and Analysis:

The optimization and electromagnetic analysis of the proposed chiral metasurface was carried out over a broad spectral window ranging from 500–5000 nm using the Finite Element Method (FEM). A stepwise evolution of the unit cell design was employed to systematically introduce symmetry breaking and enhance dichroic responses.

As shown in Fig. 3.2, the optimization process begins with a pseudo–starfish-shaped resonator comprising four inward-bent arms with a central aperture[Fig. 3.2(a)]. Although such a geometry supports multiple resonant channels, the inherent axial symmetry inhibits significant circular dichroism, resulting in negligible CD values [Fig. 3.2(b)]. To address this limitation, a split-ring element of thickness *w* with a narrow gap was incorporated into the design, effectively breaking mirror symmetry. This modification enabled a CD value of approximately 0.6 [Fig. 3.2(c)], consistent with the well-established principle that mirror-symmetry violation alone can induce circular dichroism and optical activity [92–95]. Finally, the left half of the split ring was replaced with a half-square ring, introducing an additional degree of asymmetry. This yielded strong polarization-dependent absorption under left- and right-circularly polarized (LCP/RCP) illumination, with the maximum CD increasing to 0.76 [Fig. 3.2(d)]. The final geometry thus integrates rotational asymmetry from the central blades with mirror-symmetry breaking from the outer curved and L-shaped elements, collectively reinforcing the chiral response [96,97].

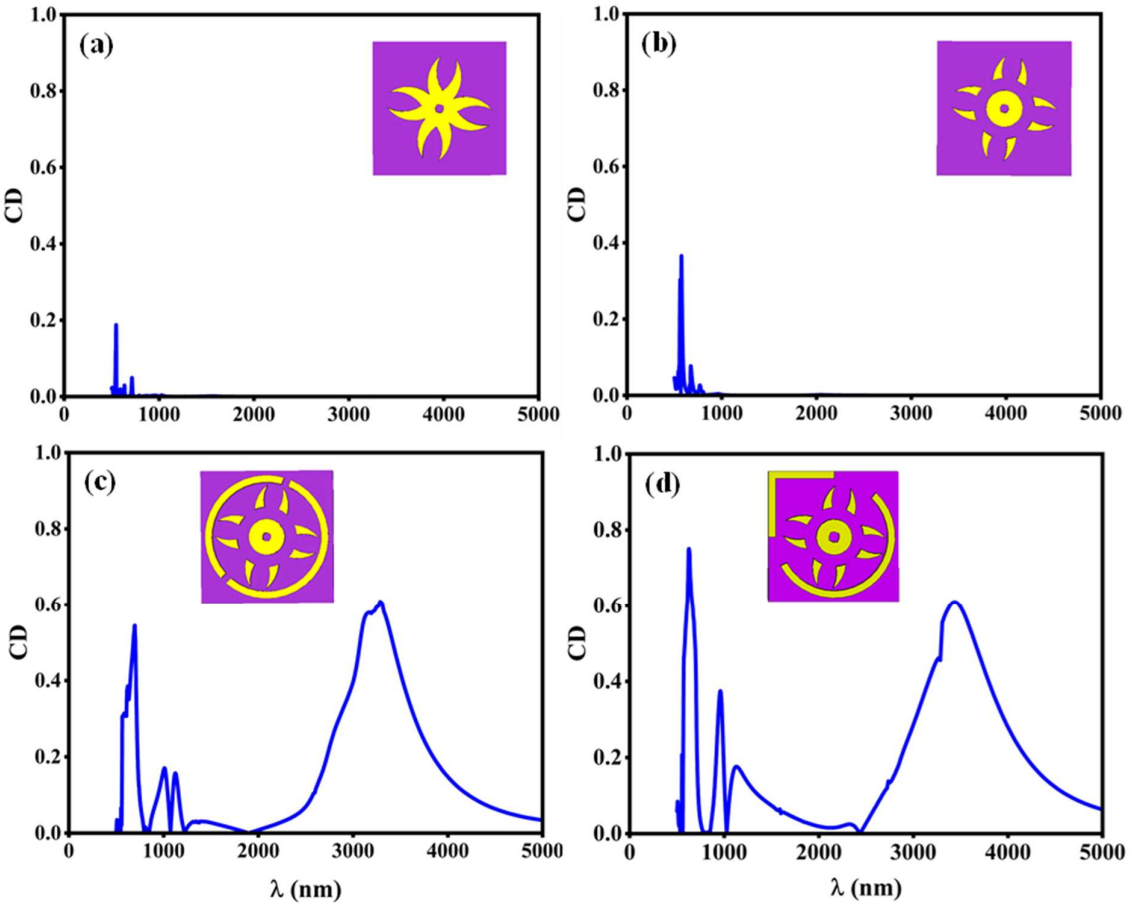

Fig 3.2. Structural analysis of the unit cell leading to the proposed chiral structure. (a), (b), (c) and (d) shows the variation of CD with the wavelength for the different variation in the geometry shown in the inset figure, leading to the final structure.

The absorption of the chiral structure when subjected to circularly polarised light and linearly polarised light are shown in Fig. 3.3 (a) and (b) where A_L, A_R represents absorption when subjected to LCP light and RCP light whereas A_x and A_y denote absorption when subjected to x-polarised light and y-polarised light. It is clear from the figure that the absorption band is restricted to the 600–650 nm range under LCP light incidence, with an absorption peak at 624 nm and $A_L = 0.81$ giving the circular dichroism value of 0.76 whereas, the absorption happens in the 3200–3800 nm range when exposed to RCP light, peaking at 3325 nm with maximum

absorption of $A_R = 0.72$ giving the circular dichroism value of 0.69 as shown in Fig. 3.4(a). On the other hand, when subjected to linearly polarized light two absorption bands are obtained with peaks at 564 nm and 962 nm with highest absorption value of 0.96 and 0.61 giving the linear dichroism value of 0.9 and 0.6 as shown in Fig. 3.4(b).

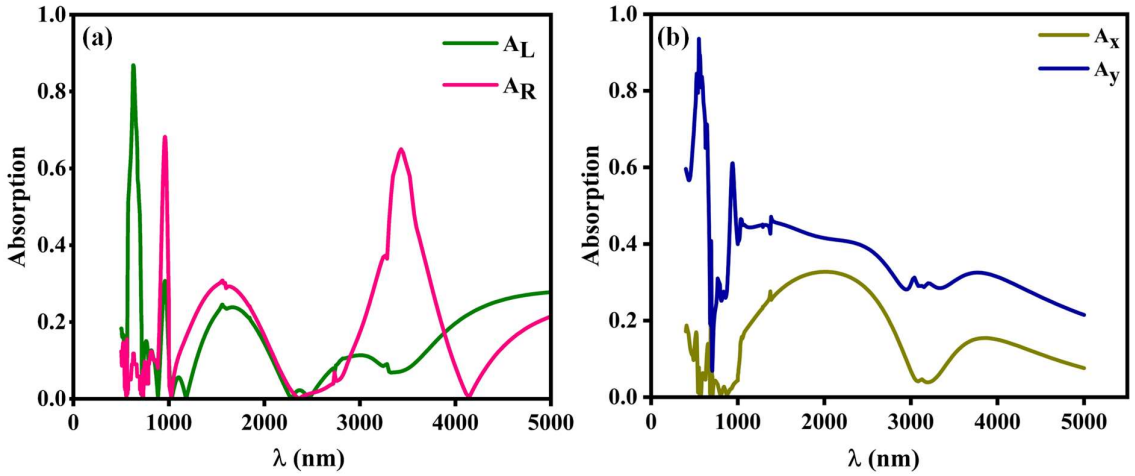

Fig 3.3 (a) The absorption curve of the chiral metasurface structure when subjected to CP light. (b) The absorption of chiral structure when subjected to LP light.

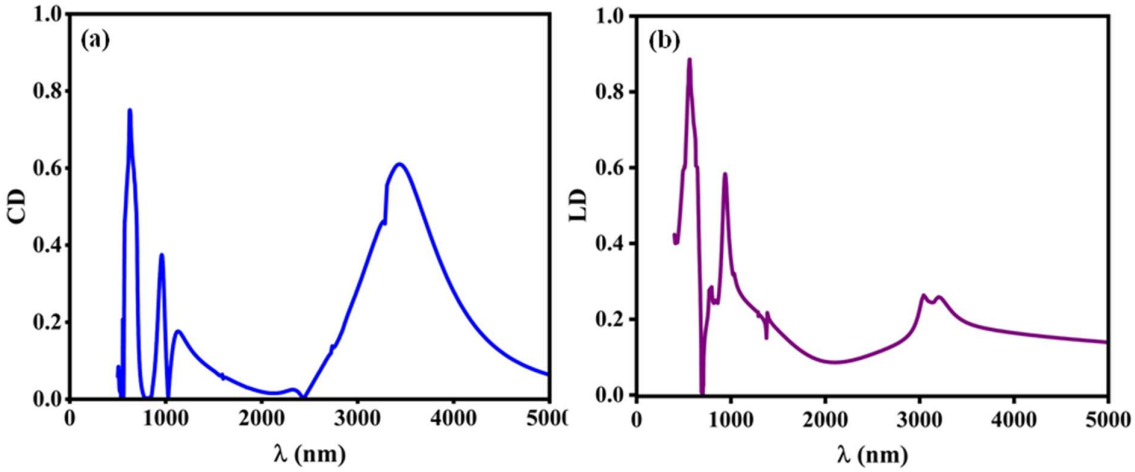

Fig 3.4 Variation of (a) circular dichroism with wavelength (b) linear dichroism with wavelength for the proposed structure.

The differing magnitudes of LD and CD originate from the distinct interaction mechanisms of linearly and circularly polarized light with chiral nanostructures. Maximizing circular dichroism requires pronounced chirality, which inherently reduces anisotropy for linear polarizations, thereby lowering linear dichroism [98]. Nonetheless, the proposed design achieves a favourable balance, sustaining high values of both CD and LD (up to 0.81 and 0.95, respectively), making it suitable for multifunctional polarization-selective devices.

To further characterize the polarization conversion properties, the ellipticity (E) and elliptical angle (ψ) of the reflected light were calculated under linearly polarised illumination:

$$E = \frac{2|R_{xy}||R_{yy}|\sin(2\Delta\varphi)}{{R_{xy}}^2+{R_{yy}}^2} \tag{3.7}$$

$$\psi = 0.5\sin^{-1}(E) \tag{3.8}$$

where $\Delta\varphi$ represents the phase difference between reflection coefficients Rxy and Ryy. For LP reflection, E≈0, whereas perfectly CP light corresponds to E = +1 (LCP) or −1 (RCP), with ψ = ±45°.

Fig 3.5 shows the ellipticity and elliptical angle values when the metasurface is subjected to linearly polarised(LP) light. For wavelengths < 1000 nm the reflected light is LP with ellipticity nearly 0. Also, it is observed that in two bands, from 1500 nm to 2480 nm and from 3200 nm to 3910 nm, the ellipticity is close to +1 with ψ nearer to 45° (highlighted by pink region). This shows that the polarisation conversion from LP to LCP is good. Conversely, from 2570 nm to 2980 nm ellipticity of -1 and ψ = -45° is observed indicating excellent polarisation conversion from LP to RCP (highlighted by green region). This indicates the good polarisation conversion from LP light to CP light.

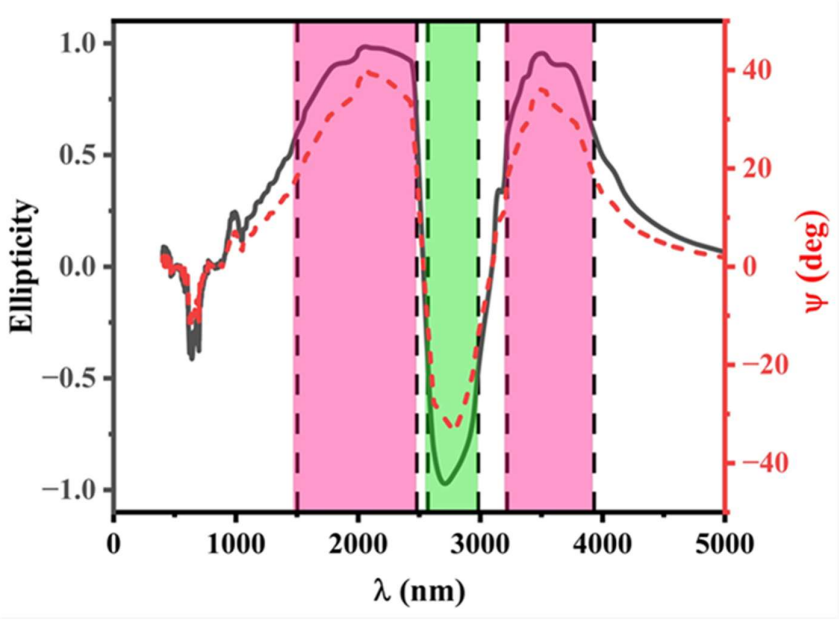

Fig 3.5 Variation of Ellipticity and elliptical polarization angle with wavelength for LP light.

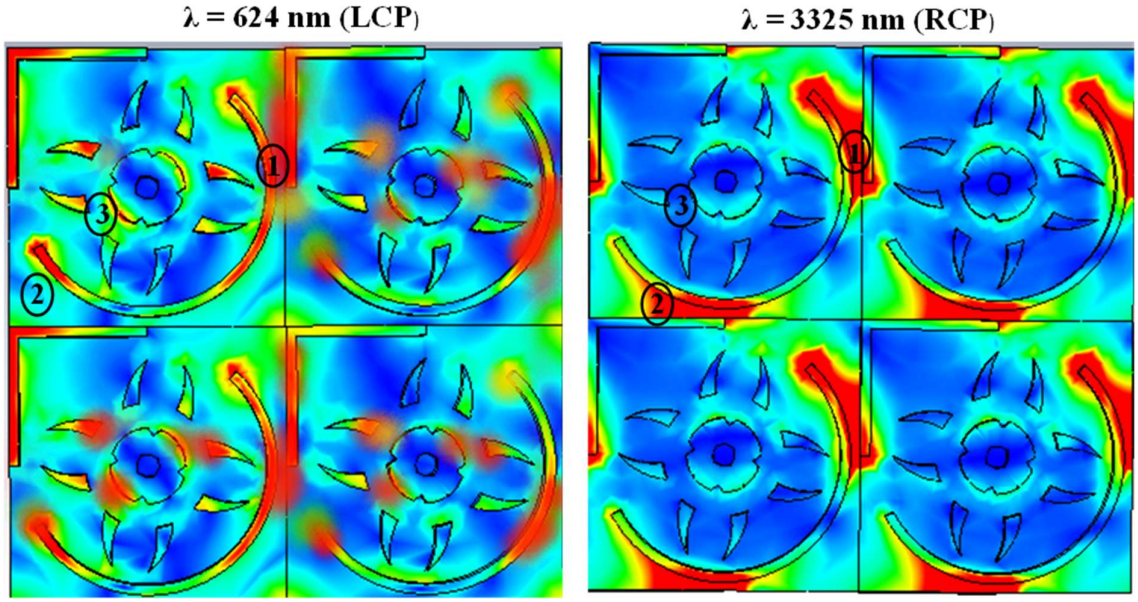

Fig 3.6 (a) Electric field distribution for the intended metasurface structure at 624 nm under incoming LCP light. (b) Electric field distribution for the intended metasurface structure at 3325 nm under incident RCP light.

Strong localised surface plasmon resonance (LSPR) is produced amidst the cavities created denoted by ①, ② and ③ within the periodic structure under LCP incidence at 624 nm, as shown in Fig. 3.6(a). On the other hand, under RCP incidence, the matching resonant mode is largely suppressed and only marginally retained around the borders of the right-leaning rectangular bars. The absolute differential absorption for LCP and RCP is the outcome of this dichotomy, and at this point, the CD value is at its maximum, 0.76. As shown in Fig. 3.6(b), only RCP light is able to completely excite the resonances inside the respective cavities at 3325 nm, producing significant coupling. Primarily, the resonance modes disappear when converted to LCP light. Therefore, at 3325 nm, a CD value of up to 0.69 is achievable.

The observed dual-band dichroism can be interpreted using the Fabry–Pérot cavity model, where cavity-induced multiple reflections enhance resonance absorption. The reflection function of a resonator can be expressed as [99–101]:

$$r(f) = \frac{r_0}{1 - re^{-\frac{i4\pi fd}{c}}} \tag{3.9}$$

where 'r_0' is the amplitude of reflected light, 'r' is the reflection attenuation coefficient, 'f' is frequency, 'd' is the cavity length, and 'c' is the speed of light. Resonance wavelengths are therefore tunable via cavity length modification.

Initially, results were analysed by varying 'p' from 275 nm to 290 nm using increments of 5 nm to investigate its impact on circular dichroism and linear dichroism, as shown in Fig. 3.7(a) and (b). Results show that for the first peak there is shift in the value of CD only whereas for the second peak there is blue shift is observed in the resonance wavelength with the increase in the value of 'p' giving the maximum value of CD for p=280 nm. Also, the linear dichroism value increases with the increase in value of 'p' accompanied by the blue shift for the emerging

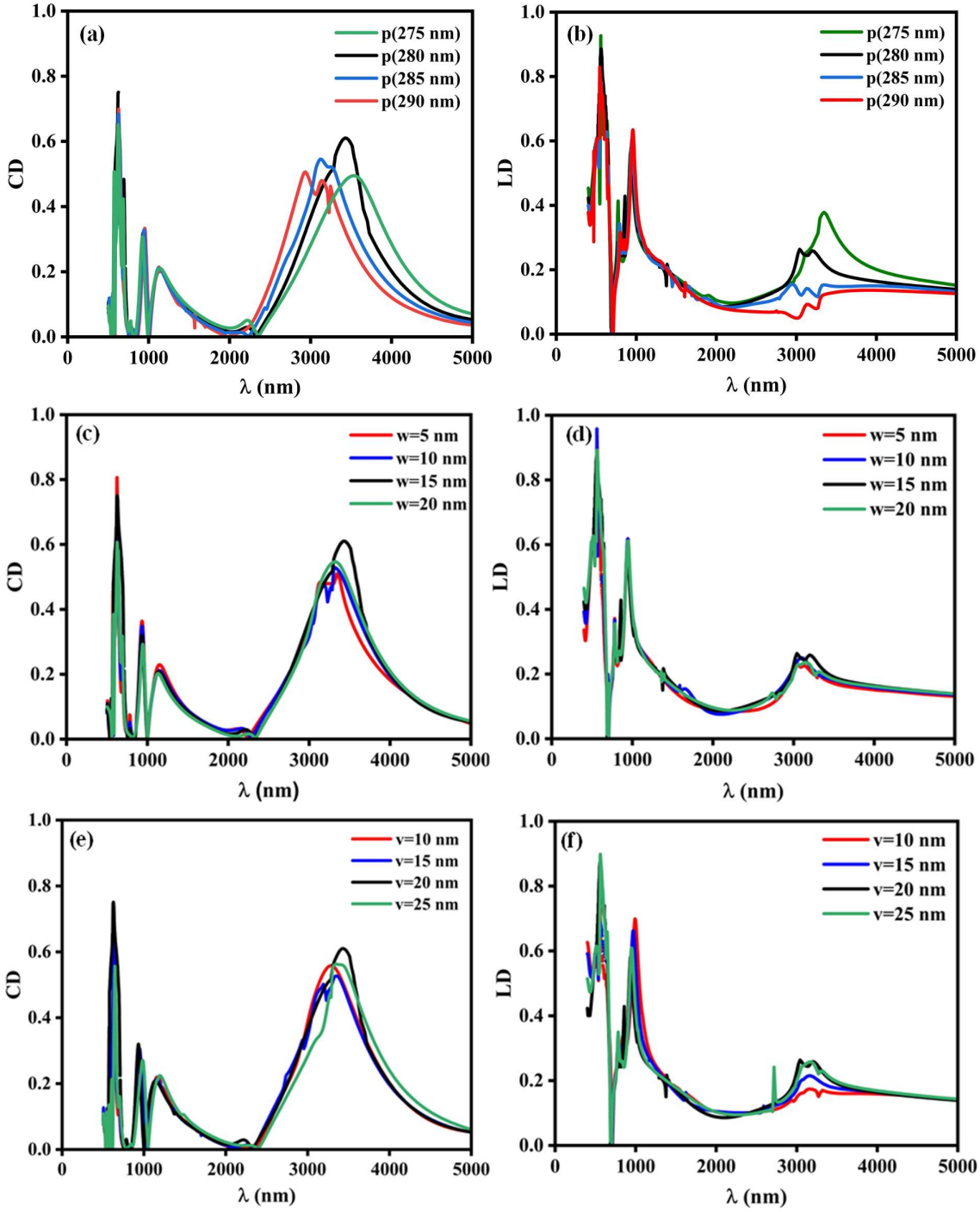

Fig. 3.7 Alterations in the CD versus wavelength curve with the variation of geometric parameter 7(a) p 7(c) w 7(e) v. Alterations in the LD verses wavelength curve with the variation of geometric parameter 7(b) p 7(d) w 7(f) v.

third peak of linear dichroism. The results are in agreement as for the Fabry–Pérot cavity, the resonance wavelength is linearly dependent on the cavity length.

Fig. 3.7(c) and (d) show the variation in circular dichroism and linear dichroism curves by varying the parameter 'w' from 5 nm to 20 nm. By comparing Fig. 3.7(a) and (b) with Fig. 3.7(c) and(d), it becomes evident that while maintaining 'w' constant and varying 'p', the first dichroism peak does not vary significantly. Therefore, it can be inferred that the localised surface plasmon resonance occurring at cavity ① is associated with the absorption value observed for incident RCP light. In contrast, alteration in 'w' causes significant variation in the first dichroism peak for LCP light. Also, the cavities ① and ② are interlinked and are affected by both the parameters 'p' and 'w'. The value of circular dichroism for the first peak decreases with the increase in the value of 'w' accompanied by the minor red shift for the second wavelength. The circular dichroism value reaches maximum of 0.81 for w=5 nm ascribed to the resonance coupling of cavities ① and ② which turns out to be more acceptable if the single peak is considered. Both peaks have a balanced circular dichroism value at w = 15 nm. Similarly, the value of both the peaks for linear dichroism is maximum for w=15 nm whereas for w=10 nm the first peak gives the maximum linear dichroism value of 0.95.

Fig. 3.7(e) and (f) show the circular and linear dichroism curves for different values of 'v' in the range 10 nm to 25 nm. With the increase in the value of 'v' first the circular dichroism value increases and then decreases for v=25 nm. Similarly, the linear dichroism curve increases linearly with the increase in value of 'v'. This happens due to the enhanced field in the gap, stronger absorption happens with a bigger 'v' size.

It is evident from the results that the parameter 'p' affects the differential absorption at the macroscopic scale majorly giving the shift in resonance wavelength whereas the parameters

'w' and 'v' affect the cavities at microscopic value thus majorly giving the shift in peak values of circular dichroism and linear dichroism. The effect of these parameter changes on circular dichroism and linear dichroism makes it clear that the position and size of absorption peaks may be precisely adjusted by adjusting 'p', 'w', and 'v' separately. This demonstrates how the device's flexible architecture allows it to be used in a variety of application settings.

Table 3.1. Comparison of relevant chiral metasurfaces exhibiting dichroism

Ref	Operating band	Dual Peak	Max. CD	Max LD
[102]	Terahertz	No	0.89	-
[103]	Terahertz	Yes	0.8	-
[74]	Infrared	Yes	0.75	-
[104]	Infrared	No	0.86	0.81
This work	Visible-Infrared	Yes	0.81	0.95

Finally, Table 3.1 presents a comparison of the performance of the suggested chiral metasurface with that of other research reported recently, in terms of CD and LD. Upon conducting a comparison analysis, two main benefits of our design are identified. First, it offers notable linear and circular dichroism with strong chiral asymmetry. Also, it has the ability to retain a high dichroism value while inducing distinct peaks under different(linear/circular) incident polarisations making it more versatile.

3.4. Summary:

In this chapter, a chiral metal–perovskite–metal (MPM) metasurface absorber has been proposed and systematically analysed. The design employs a pseudo–starfish resonator integrated with resonant cavities that break both rotational and mirror symmetries, thereby enabling strong chiral optical responses under oblique incidence. Through careful geometric

tuning, the structure simultaneously achieves high circular dichroism (CD) and linear dichroism (LD), a feature rarely demonstrated in a single device. The study highlights that the observed dichroism originates from polarization-dependent interference between neighboring resonant cavities, supported by localized surface plasmon resonances and Fabry–Perot type cavity modes. By selectively exciting these resonances with different incident polarizations, distinct absorption peaks for circularly and linearly polarized light are obtained, reaching maximum absolute CD and LD values of 0.81 and 0.95, respectively. Furthermore, the analysis of ellipticity and elliptical angle demonstrates efficient polarization conversion, with reflected LP light nearly transformed into pure CP states in defined spectral bands.

Overall, this work establishes hybrid perovskite–based MPM architectures as a powerful platform for achieving dual dichroism functionalities in a single metasurface. Such devices hold strong potential for advanced photonic, optoelectronic, and spintronic applications where simultaneous manipulation of linear and circular polarization is required.

4

CHAPTER

Triple-Band Perovskite-Based Chiral Metasurface for Biosensing Applications

- *Development of a perovskite-based chiral metasurface exhibiting strong triple-band circular dichroism response.*
- *Integration of metal–perovskite–metal architecture to achieve enhanced optical chirality and spectral selectivity.*
- *Realization of biosensing functionality through refractive index sensitivity and resonance shift analysis.*
- *Potential for next-generation photonic and biomedical devices combining chirality with tunability.*

4.1. INTRODUCTION

Having established the fundamental differences between achiral and chiral metasurfaces in the preceding chapters, we now extend the discussion towards their application in biosensing. Metasurfaces, owing to their subwavelength structuring, offer unprecedented capabilities to manipulate electromagnetic waves and have been demonstrated as powerful platforms for label-free biosensing applications [105–107]. Specifically engineered surfaces can enhance light–matter interactions, thereby improving sensitivity toward biomolecules associated with vital biological processes [66,108]. Depending on the material choice and optical design, metasurfaces have been successfully employed for surface-enhanced Raman spectroscopy (SERS), fluorescence enhancement, and refractive index sensing [109–111]. Their planar form, compatibility with lab-on-chip devices, and real-time operation potential make them highly promising for next-generation biomedical systems [112,113].

An important feature of metasurfaces lies in their multifunctional capability. By tailoring the nanostructure design, a single metasurface can be engineered to detect multiple biomarkers or physical properties such as pH, temperature, or chirality simultaneously [114–116]. Moreover, the ability to support multiple resonances across distinct spectral regions allows a single device to perform diverse biosensing tasks. This multispectral capacity is crucial for advanced medical diagnostics, continuous monitoring of complex biological processes, and the realization of highly integrated, compact biosensors.

Chiral metasurfaces are particularly advantageous in this regard, as they exploit circular dichroism (CD) to achieve highly selective and sensitive detection of chiral analytes [20,117,118]. Since chirality is a fundamental property of many biomolecules, CD-active metasurfaces provide a sensitive, label-free approach for probing enantioselective interactions.

The enhancement of weak molecular CD signals is made possible by carefully engineered structural asymmetries, which strongly couple to circularly polarized light, particularly under oblique incidence. This makes such metasurfaces powerful tools for studying chirality-dependent phenomena including drug interactions, protein folding, and disease-related biochemical pathways [119,120].

In this chapter, we present a perovskite-based optical chiral metasurface that exhibits selective absorption across three spectral bands - visible, near-infrared (NIR), and mid-infrared (MIR). The structural design employs a pseudo-starfish configuration with six arms containing resonant chambers, thereby enabling triple-band functionality. Finite-element simulations reveal that localized electric and magnetic field enhancements within these cavities are responsible for the strong dichroism, and by tuning structural parameters, each resonance can be independently controlled. Importantly, the multifunctional nature of this metasurface allows its use in diverse biosensing scenarios: detection of hemoglobin concentration in the visible range, glucose sensing in the NIR, and cancer cell detection in the MIR. Thus, the proposed perovskite-based chiral metasurface biosensor demonstrates the potential of multifunctional chiral photonic devices, uniting broadband spectral selectivity, enhanced light–matter interaction, and integrability into compact biomedical diagnostic platforms.

4.2. Structural Design and Analysis of Chiral Metasurface:

The architecture of the proposed metasurface absorber is illustrated in Fig. 4.1(a). The design is based on a metal–perovskite–metal (MPM) configuration, which has proven to be an efficient platform for amplifying light matter interaction. The bottom layer consists of a 100 nm thick gold film deposited on a dielectric substrate. This continuous metallic backplane plays a crucial role by eliminating transmission and creating Fabry–Perot type cavity conditions,

thereby allowing multiple internal reflections of the incident wave. On top of this reflective layer, a perovskite film of approximately 200 nm thickness is deposited. The dielectric properties of methylammonium lead tribromide ($MAPbBr_3$), obtained from Ishteev et al. [87], ensure strong absorption and a tunable bandgap, while its high refractive index supports resonant electromagnetic modes, further enhancing the coupling with incoming light. The top layer comprises gold (Au) resonators patterned into a pseudo-starfish geometry with six arms of arc radius R = 130 nm and thickness 100 nm. The optical constants of gold are taken from Babar and Weaver [88]. The arms are not uniform but instead include carefully engineered cavities bounded by semicircular arcs and rectangular bars. These cavities serve as localized hot-spots where plasmonic resonances are strongly confined, amplifying the absorption of incident polarized waves. More importantly, the inclusion of both circular and rectangular elements breaks the in-plane symmetry of the unit cell, which is a prerequisite for achieving strong chiroptical effects.

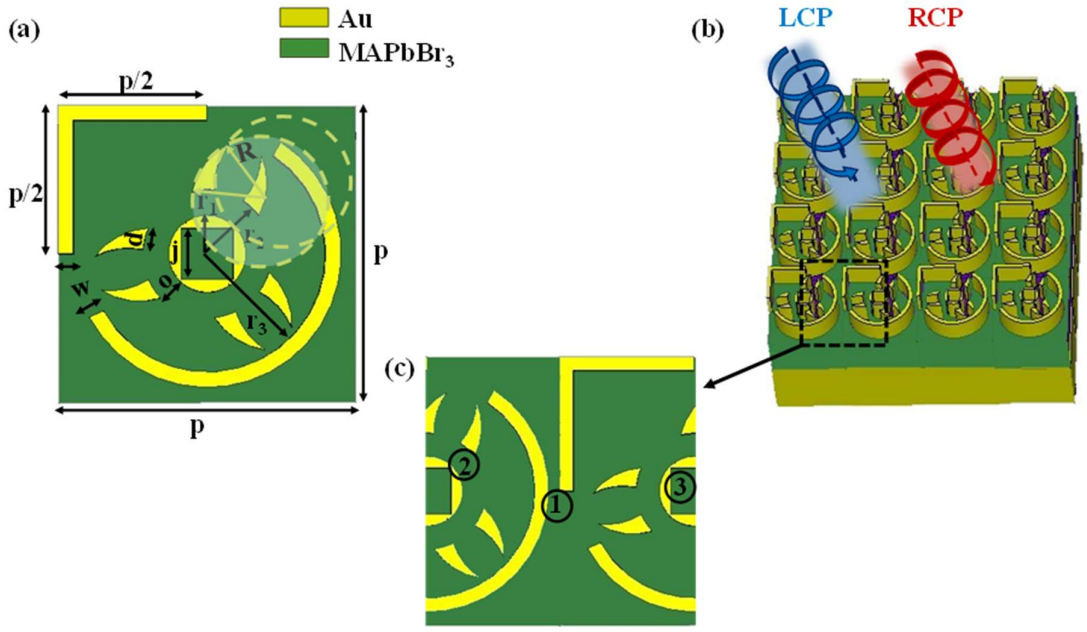

Fig. 4.1 (a) Top view of the proposed unit cell (b) 3D view of the designed metasurface and (c) Representation of the inbuilt cavities in the proposed structure.

The design of the metasurface in its final optimized form was developed through a systematic evolution. Initially, a simple six-armed pseudo-starfish resonator was considered. However, due to its preserved axial symmetry, the resulting circular dichroism was negligible. In a second iteration, a central circular cavity of width '*o*' was introduced, leading to partial symmetry breaking and a modest CD value of approximately 0.4. To further enhance the asymmetry, a split-ring resonator of thickness *w* with a narrow gap was incorporated along with L-shaped bars, thereby breaking mirror symmetry and increasing CD to about 0.6. It is important to note that in order to realize significant chiroptical response, both n-fold rotational symmetry (n > 2) and mirror symmetry must be broken simultaneously, consistent with earlier theoretical predictions [96,97]. Finally, in the optimized design, a rectangular cavity of side '*j*' was added, resulting in a structure capable of producing high CD values across three distinct wavelength regions.

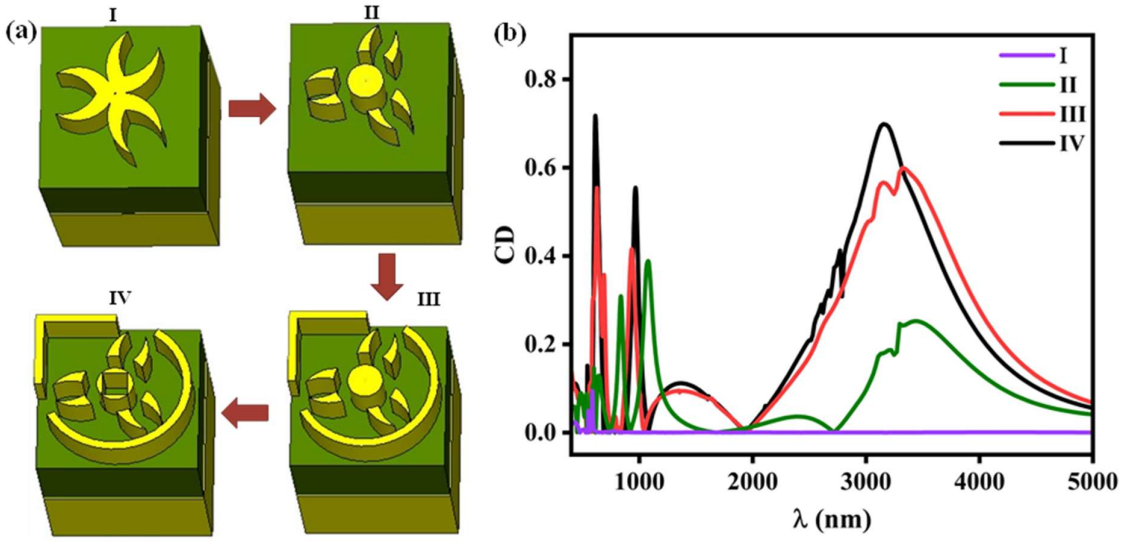

Fig. 4.2. Evolution of the (a) design of the proposed unit cell and (b) the corresponding CD.

The progressive improvement in chiroptical performance throughout this evolution is depicted in Fig. 4.2. The optimized structural parameters of the final unit cell are 'p' = 285 nm, 'd' = 25 nm, 'w' = 10 nm, 'j' = 50 nm, 'r_1' = 65 nm, 'r_2' = 85 nm, and 'r_3' = 130 nm. Numerical simulations were performed using CST Microwave Studio, where periodic boundary conditions were applied along the x- and y-directions, while the incident wave propagated along the z-axis. Since the presence of the metallic backplane leads to vanishing transmission, the analysis focused entirely on the reflection characteristics to quantify dichroism.

The optical activity of the designed metasurface is quantified in terms of circular dichroism, defined as:

$$CD = \left| A_L - A_R \right| \tag{4.1}$$

where A_L and A_R represent the absorption under left circularly polarized (LCP) and right circularly polarized (RCP) incidence, respectively.

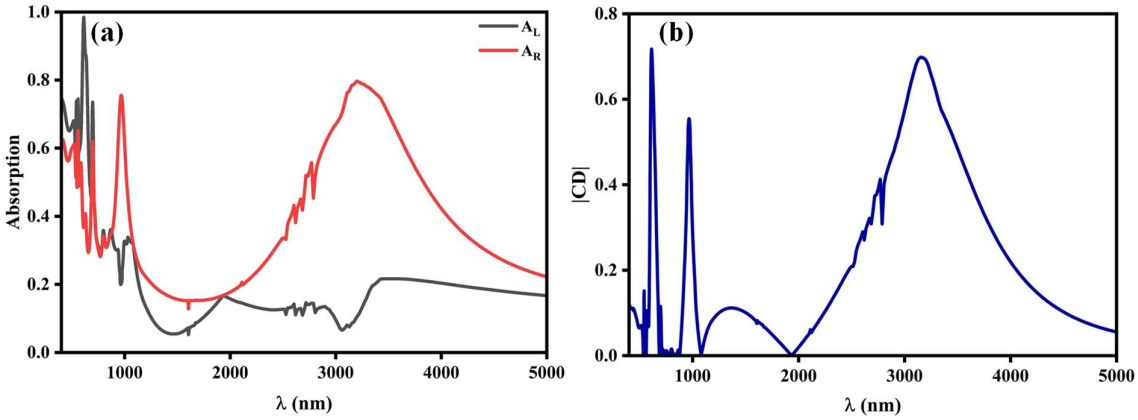

Fig. 4.3 (a) The absorption curve and (b) CD curve of the metasurface when subjected to circularly polarised light.

The results reveal that under LCP excitation, a strong absorption peak appears at 611 nm with a maximum absorption of 0.98, giving rise to a CD value of 0.72. Under RCP excitation, on the other hand, the structure exhibits two absorption peaks, one at 933 nm with absorption of

0.75 and another at 3151 nm with absorption of 0.79. These peaks correspond to CD values of 0.56 and 0.71, respectively, as shown in Fig. 4.3(a–b). Such strong and spectrally separated dichroism peaks highlight the versatility of the design across multiple spectral bands, extending from the visible into the infrared.

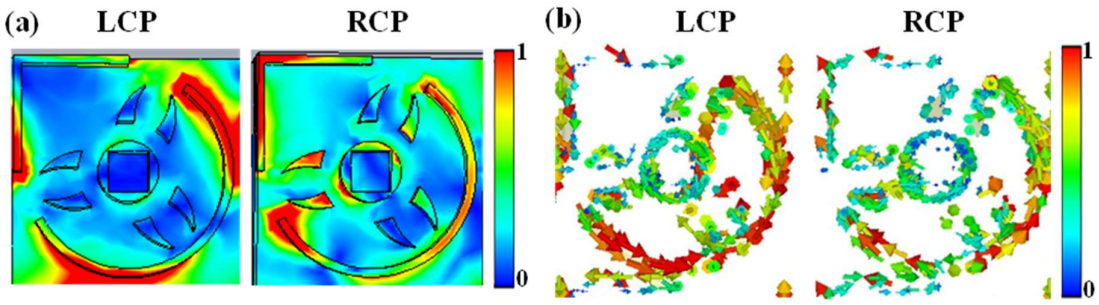

Fig. 4.4. (a) Electric field distribution and (b) Surface current distribution for the intended metasurface structure at 611 nm and 3151 nm under incoming LCP and RCP light respectively.

The physical origin of this pronounced dichroism can be understood by analysing the localized surface plasmon resonances and surface current distributions across the metasurface. At resonance, the incident light couples strongly to the engineered cavities, producing localized surface plasmon resonance (LSPR) modes. Fig. 4.4(a) illustrates that under LCP incidence, strong LSPR is concentrated along the far-right circular arc and the bottom semicircular arm of the resonator, while under RCP incidence these resonances are largely suppressed. This unequal distribution of localized fields results in distinctly different absorption for LCP and RCP waves. The analysis of surface current distribution further confirms this behaviour, as shown in Fig. 4.4(b). Under LCP incidence, the induced surface charges rotate following the handedness of the wave, whereas under RCP incidence the rotation direction is reversed, aligning with the field vector of the RCP light. This difference in the rotational direction of

charge carriers under opposite polarizations is the fundamental reason for the observed asymmetric absorption, which manifests as strong circular dichroism.

4.3. Parametric Analysis:

The performance of the proposed perovskite-based chiral metasurface was further investigated by carrying out a detailed parametric analysis, with the aim of understanding how individual geometrical parameters influence the chiroptical response. The starfish-shaped resonator contains several engineered cavities, each of which plays a critical role in shaping the resonance behavior of the device. These cavities act as miniature Fabry–Perot resonators, where incoming light undergoes multiple internal reflections at specific wavelengths, leading to constructive interference and enhancement of the localized electric field. Such resonance-driven amplification is the underlying reason for the strong circular dichroism values observed in the optimized design. The optical response of these cavity modes can be qualitatively described by the Fabry–Perot reflection model [99–101],

$$R(\omega) = \frac{R_0}{1 - Re^{-\frac{2i\omega z}{c}}} \tag{4.2}$$

where 'ω' denotes the angular frequency, 'z' is the effective cavity length, 'c' is the speed of light in vacuum, and 'R_0' represents the reflection amplitude of the cavity. Here, 'R' acts as the attenuation coefficient of the reflected wave. This formulation clearly shows that by varying the cavity length 'z', one can effectively tune the resonance wavelength, thereby controlling the spectral position of the dichroic peaks.

To systematically study this effect, the key geometrical parameters associated with the cavity dimensions were independently varied while keeping the remaining structural features constant. This ensured that the observed modifications in the optical response were solely attributable to the chosen parameter under study. Four parameters were identified as the most

influential: the periodicity of the unit cell 'p', the width of the angular cavity within the starfish arms 'o', the width of the semicircular arc 'w', and the side length of the rectangular cavity 'j', as shown in Fig. 4.1. Each of these parameters is associated with a distinct cavity region, allowing the effect of geometry on the three main resonance peaks to be clearly delineated.

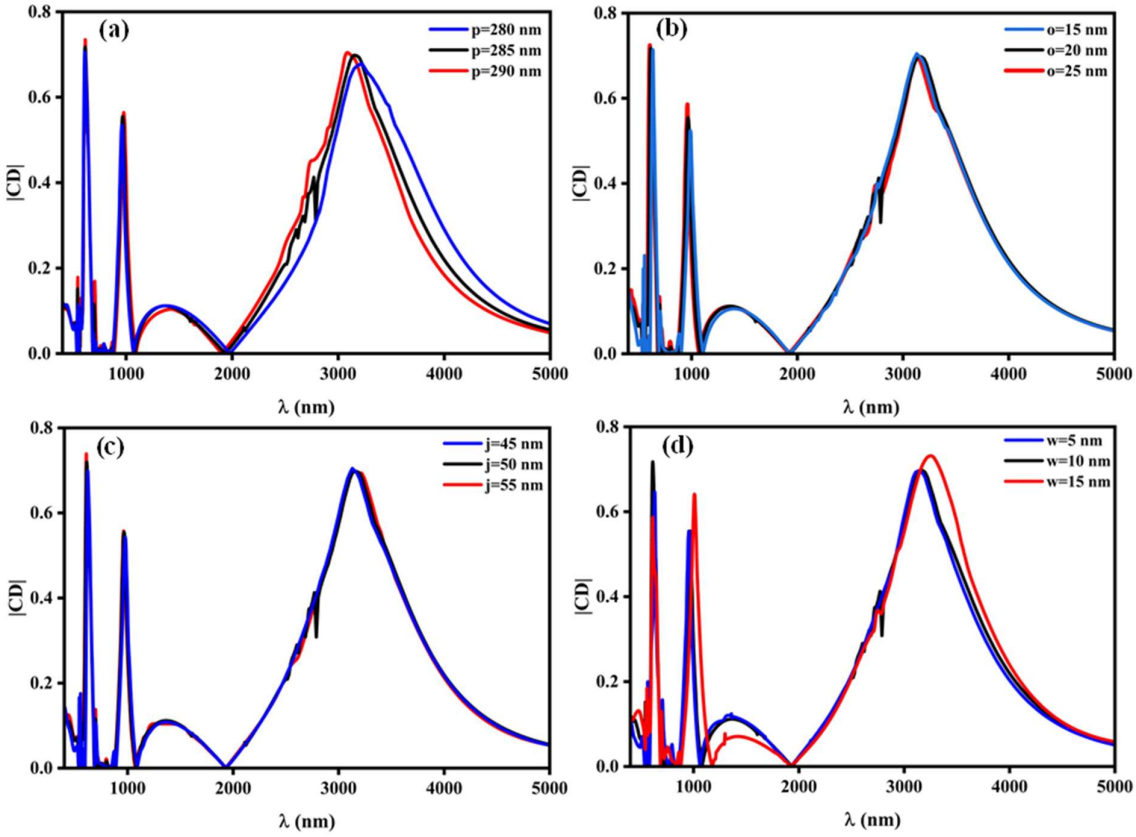

Fig. 4.5. Transitions in the CD versus wavelength curve with the change in geometric parameter (a) p, (b) o, (c) j, (d) w.

The variation of periodicity 'p' was first examined. Fig. 4.5(a) shows that modifying 'p' predominantly influences the third CD peak in the longer wavelength regime, producing a distinct blue shift in the resonance position. The maximum CD value was observed at 'p' = 290 nm, confirming that periodicity strongly governs the macroscopic Fabry–Perot condition by effectively scaling the entire unit cell. In contrast, the parameter 'o', which determines the

angular cavity width inside the starfish arms, was found to primarily affect the second resonance peak, as depicted in Fig. 4.5(b). Increasing the value of 'o' not only enhances the CD amplitude of this peak but also induces a blue shift in its resonance wavelength. This suggests that the angular cavity plays a dominant role in governing the intermediate spectral response of the metasurface.

The influence of the rectangular cavity side 'j' is illustrated in Fig. 4.5(c). Here, the effect is relatively moderate compared to 'p' and 'o'. The variation of 'j' causes a slight increase in the CD value of the first peak and introduces a minor red shift in the third peak, while leaving the second peak almost unaffected. This behaviour indicates that the rectangular cavity contributes locally to near-field confinement rather than driving large spectral shifts. On the other hand, the semicircular arc width 'w' exerts a much more pronounced effect, as shown in Fig. 4.5(d). Modifying 'w' strongly impacts all three peaks because the cavity region associated with this parameter interacts with both LCP and RCP modes simultaneously. As a result, variations in 'w' alter both A_L and A_R, leading to significant modifications in CD. The maximum CD for the first peak was achieved at 'w' = 10 nm, while for the second and third peaks, optimal enhancement was obtained at 'w' = 15 nm.

The outcomes of this analysis strongly support the Fabry–Perot cavity hypothesis, wherein the resonance wavelength scales linearly with the effective cavity length. While the parameter 'p' induces large-scale shifts across the spectrum by modifying the unit cell periodicity, parameters such as 'w', 'o', and 'j' act more locally, primarily tuning the field confinement and peak intensity within individual cavities. Together, this systematic study demonstrates that precise control over the dichroic response of the metasurface can be achieved by tailoring the cavity dimensions, thereby allowing fine adjustment of both resonance positions and peak magnitudes. Such tunability not only validates the robustness of the design strategy but also

highlights its adaptability for application-specific optimization in biosensing and multifunctional photonic devices.

4.4. Chiral Metasurface Biosensor:

Modifying the refractive index of the medium that fills the vacancies in the upper layer of the proposed metasurface directly alters the effective refractive index of the overall structure, thereby shifting the resonance frequency. Since the resonance spectrum strongly influences the CD response, even small changes in the surrounding refractive index lead to significant variations in the optical characteristics. This behaviour forms the foundation for refractive index-based sensing applications. The sensitivity of the device is quantitatively expressed as:

$$S = {}^{\Delta\lambda}/_{\Delta n} \text{ nm/RIU} \tag{4.3}$$

where 'Δλ' represents the resonance wavelength shift observed for a given change in refractive index 'Δn'. The larger the value of 'S', the more effective the metasurface is in detecting subtle variations in the analyte environment. In the present work, the sensing capabilities of the proposed metasurface have been examined in three different regimes: hemoglobin sensing in the visible band, glucose sensing in the near-infrared (NIR) region, and cancer cell detection in the mid-infrared (MIR) region. These case studies highlight the broad applicability of the metasurface platform.

4.4.1. Hemoglobin sensor:

Hemoglobin (Hb) concentration is a vital physiological parameter, with normal levels typically ranging from 130 g/L to 166 g/L in males and 100 g/L to 150 g/L in females [121]. Deviations from these ranges have serious clinical implications: reduced Hb concentration leads to conditions such as anaemia, fatigue, and nausea, while elevated concentrations increase blood

viscosity, raising the risk of coagulation and potentially causing heart attacks or strokes [122,123]. Therefore, a sensitive and reliable method for monitoring hemoglobin concentration is highly desirable.

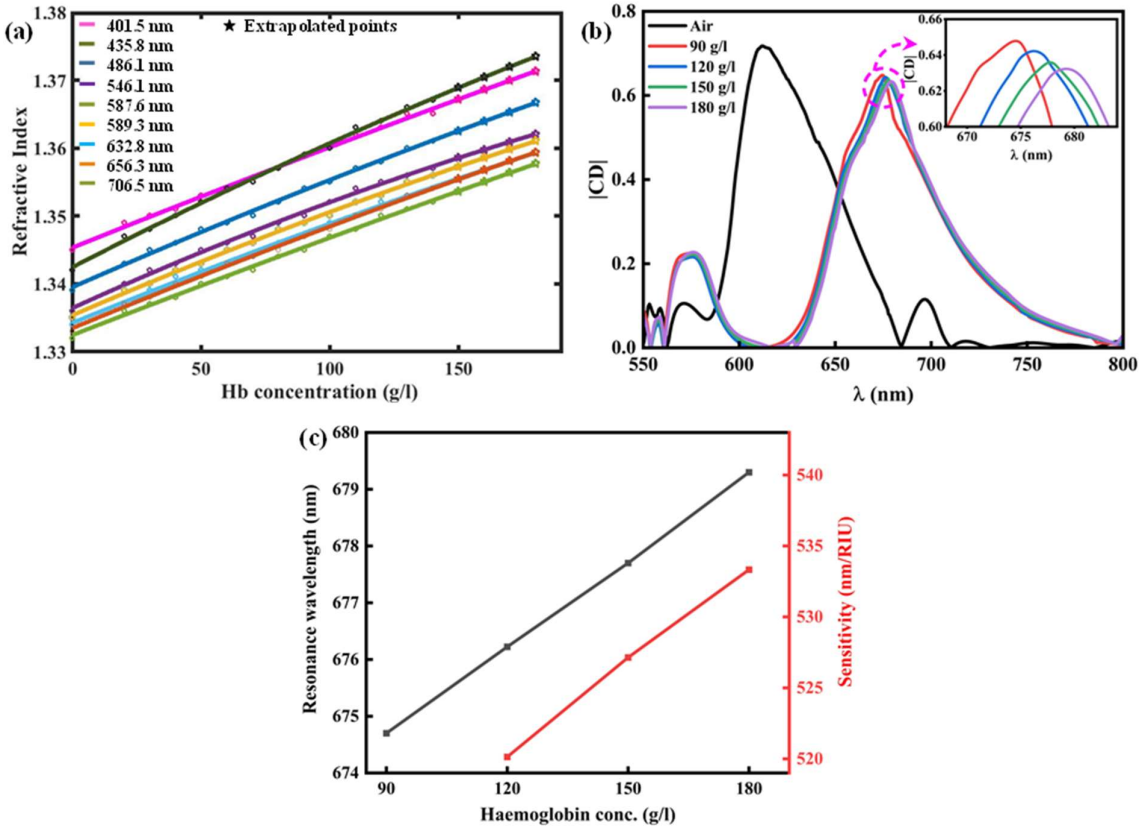

Fig. 4.6. (a) The linear curve fit and extrapolated values of refractive index of the blood with concentration for different wavelengths. (b) The variation of the CD curve for different concentrations of hemoglobin. (c) Variation of resonance wavelength and sensitivity with the concentration of hemoglobin.

In this work, hemoglobin concentrations of 90 g/L, 120 g/L, 150 g/L, and 180 g/L were studied to assess the biosensing ability of the proposed metasurface. The refractive index corresponding to each concentration was theoretically determined using least-square fitting to extrapolate hemoglobin's refractive index in the visible region [124], as shown in Fig. 4.6(a).

When blood samples with varying Hb levels were introduced into the metasurface cavities, distinct shifts were observed in the CD spectra. Fig. 4.6(b) illustrates the variation of CD with different concentrations, and the inset clearly shows the separation of CD curves corresponding to low, normal, and high Hb values. A systematic red shift in the resonance peak was observed as Hb concentration increased, reflecting the progressive change in refractive index.

Fig. 4.6(c) further quantifies this trend, showing the relationship between hemoglobin concentration, resonance wavelength, and sensitivity. As the concentration increased, both the resonance wavelength and the calculated sensitivity values also increased. Sensitivity was evaluated using the resonance wavelength shift method, where the difference in wavelength ($\Delta\lambda$) was normalized with respect to the refractive index change (Δn). Table 4.1 summarizes the results, showing sensitivity values of 520.1 nm/RIU, 527.1 nm/RIU, and 533.3 nm/RIU for different concentration levels. These results confirm that the designed chiral metasurface can act as an efficient biosensor for hemoglobin, enabling precise monitoring of its concentration through CD resonance shifts.

Table 4.1 Sensitivity Analysis

Conc. of hemoglobin (g/L)	Resonance Wavelength (nm)	n	$\Delta\lambda$ (nm)	Δn	Sensitivity (nm/RIU)
90	674.7	1.34847	-	-	-
120	676.2	1.35140	1.524	0.00293	520.1365
150	677.7	1.35420	1.470	0.00280	527.1429
180	679.3	1.35720	1.600	0.00300	533.3333

4.4.2. Glucose concentration sensor:

The determination of glucose concentration is of great importance not only in the medical domain but also in food processing industries, where precise sugar quantification is necessary to ensure quality and safety. For example, in medicinal diagnostics, monitoring glucose levels is crucial for the detection and management of diabetes, while in the food industry it plays an essential role in processes such as syrup preparation from natural sources like date juice. The proposed metasurface, when operated in the NIR spectral region, demonstrates significant potential for use as a glucose concentration sensor.

To establish its applicability, the refractive indices corresponding to different glucose concentrations were first determined and used to create a calibration curve. This was achieved through the refractometric method [125], where the refractive index of an aqueous glucose solution can be described as:

$$n = n_{H_2O} + \alpha C \tag{4.4}$$

where 'n_{H_2O}' is the refractive index of water, 'α' = 0.00143 is a proportionality constant, and 'C' is the concentration of glucose in g/100 ml. Using this relationship, the refractive indices of glucose solutions ranging from 0 g/100 ml to 30 g/100 ml were obtained and applied to the metasurface analysis.

Fig. 4.7(a) depicts the CD response of the proposed chiral metasurface for the different glucose concentrations. As the glucose concentration increases, a clear red shift in the resonance wavelength is observed, reflecting the strong dependence of CD spectra on the refractive index of the surrounding medium. This shift in resonance wavelength arises due to enhanced capacitance between adjacent ridges of the metasurface structure, a direct result of the increased permittivity and refractive index with rising glucose concentration.

The corresponding resonance wavelength shifts and calculated sensitivities are shown in Fig. 4.7(b). The results demonstrate a consistent increase in resonance wavelength with glucose concentration, validating the refractive index sensing mechanism. The sensitivity values confirm that the proposed metasurface provides a reliable platform for glucose concentration detection in the NIR region, making it suitable for applications in medical diagnostics and quality control in food manufacturing.

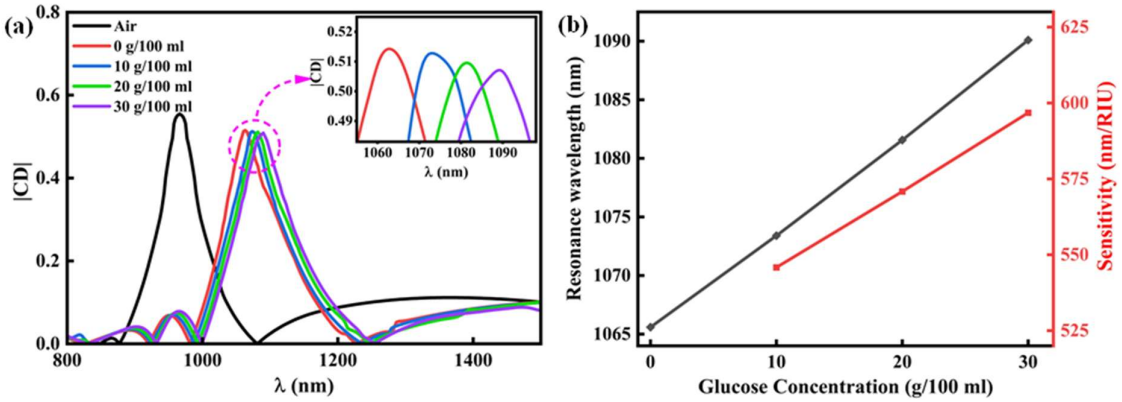

Fig. 4.7. Variation of (a) CD with the wavelength, (b) resonance wavelength and the relative sensitivity for the different concentrations of glucose mixture.

4.4.3. Cancer cell detection sensor:

In addition to hemoglobin and glucose sensing, the proposed metasurface has been further extended to cancer cell detection in the MIR spectral region. Spectroscopic biosensors operating in the MIR have long been recognized for their ability to detect disease signatures and hazardous compounds due to strong vibrational resonances in this wavelength range. Early detection of cancer cells is of paramount importance, as it can significantly improve treatment effectiveness and patient survival rates. Importantly, cancerous cells often exhibit distinct

optical signatures compared to healthy cells, including differences in refractive index, which can be exploited for highly sensitive detection.

For this study, three different types of cancer cells—skin cancer (Basal), breast cancer (MDA-MB-231), and cervical cancer (HeLa)—were investigated using the proposed metasurface. The refractive indices of these cells, along with those of corresponding healthy cells, are summarized in Table 4.2. Significant differences between normal and cancerous cells were observed in their refractive indices, highlighting the feasibility of optical refractive index-based detection.

Table 4.2. Refractive index of various normal and cancer cells

Cell type and Conc.	Name of cell	Refractive index	References
Skin Cancer(80%)	Basal	1.38	[126–128]
Skin Normal Cell (30-70%)		1.36	[126–128]
Breast Cancer(80%)	MDA-MB-231	1.401	[127–129]
Breast Normal Cell(30-70%)		1.387	[127–129]
Cervical Cancer(80%)	HeLa	1.392	[127–129]
Cervical Normal Cell(30-70%)		1.368	[127–129]

Fig. 4.8(a) shows the CD spectra for normal and cancerous cells, while Fig. 4.8(b) illustrates the corresponding resonance wavelength shifts. The results reveal a systematic red shift in the resonance wavelength when cancerous cells are introduced, accompanied by a slight reduction in the CD amplitude. These changes indicate the strong interaction between the incident polarized light and the distinct refractive index environment created by cancerous cells.

The calculated sensitivities for detecting the three types of cancer cells are remarkably high, with values of 2371.1 nm/RIU for breast cancer (MDA-MB-231), 2516.7 nm/RIU for skin cancer (Basal), and 2680.9 nm/RIU for cervical cancer (HeLa). These exceptionally high

sensitivity values underline the potential of the proposed perovskite-based chiral metasurface as a powerful diagnostic tool for early cancer detection. By enabling label-free, real-time monitoring of cancer cells through their refractive index signatures, the proposed design provides a pathway towards practical biomedical applications in disease diagnostics.

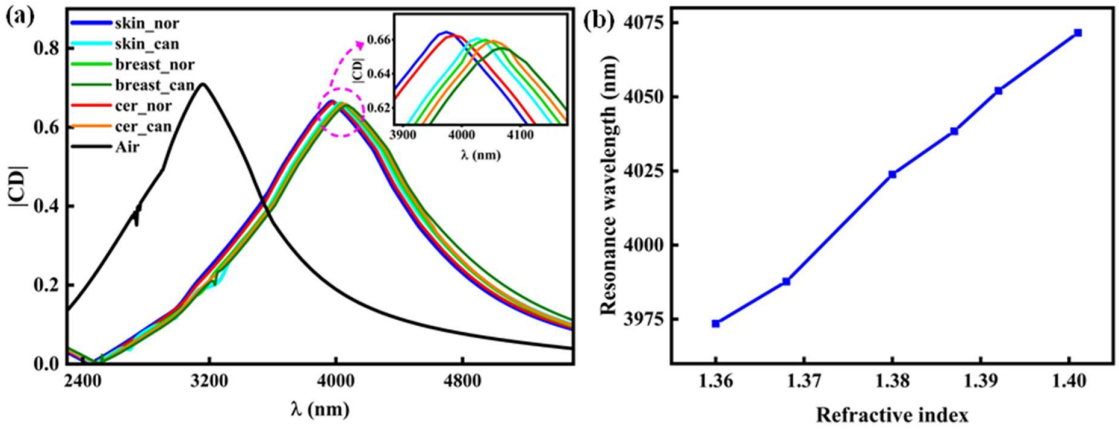

Fig. 4.8. Variation of (a) circular dichroism curve for the different types of cancer. (b) Variation of resonance wavelength with the increase in the refractive index.

The resonance wavelength shift and variation in CD response for different refractive indices were systematically investigated across the three operational wavebands of the proposed chiral metasurface, namely the visible, NIR, and MIR regions. The analysis reveals that the sensitivity of the structure exhibits a clear increasing trend with the resonance wavelength, demonstrating superior performance at longer wavelengths. This behaviour can be attributed to two fundamental reasons. First, as the operational wavelength increases, the evanescent field generated by the metasurface penetrates deeper into the surrounding medium, leading to enhanced overlap and stronger light–matter interaction with adjacent biomolecules. This enhanced coupling directly contributes to larger resonance wavelength shifts for a given change in refractive index. Second, sensitivity inherently scales with resonance wavelength, since longer wavelengths yield larger absolute resonance shifts even for small variations in the

refractive index. Together, these factors explain the progressive enhancement of sensitivity as the resonance wavelength transitions from the visible to the NIR and further into the MIR region.

The relationship between resonance wavelength and sensitivity is quantitatively illustrated in Fig. 4.9. The discrete star markers represent the sensitivity values obtained for different resonance peaks across the three regions, while the red line shows a linear curve fit applied to these data points. The shaded band surrounding the fit represents the confidence interval, indicating the statistical probability range within which sensitivities corresponding to additional observations or other biomolecular samples may be expected to lie for the proposed metasurface design. This graphical analysis highlights the robust correlation between resonance wavelength and sensitivity, thereby reinforcing the versatility of the proposed chiral metasurface biosensor.

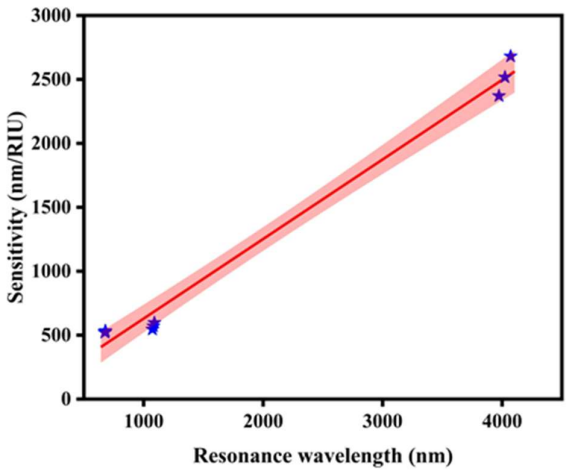

Fig. 4.9. Linear fit curve of the sensitivity values of the structure for different resonance wavelengths across three regions (shaded region represents the confidence band).

Furthermore, a comparative study of the proposed device with other reported chiral sensors is summarized in Table 4.3. From this analysis, it can be inferred that although some structures demonstrate higher sensitivity within a single operational region, the proposed metasurface provides the unique advantage of maintaining moderately high sensitivity while simultaneously operating across three distinct spectral bands. This multifunctionality significantly expands its application space, making it a strong candidate for next-generation biosensors that require a single device to monitor multiple biological parameters or processes.

Table 4.3. Comparison table for different chiral metasurface sensors

Reference	Type of metasurface	Type of sensing	Region	Max. sensitivity reported (nm/RIU)
[130]	Transmission based chiral metasurface	RI based	Visible	474
[131]	Helix shaped Chiral metasurface	Bio-Molecule	NIR	471
[132]	Chiral metasurface	RI based	NIR	750
[133]	Chiral	RI based	Visible	304
[134]	Half ring based chiral metasurface	Nano-fluids	THz	182.5
[135]	Helix based chiral metasurface	Fluids	NIR	761
[136]	Chiral metasurface	Chiral molecule	NIR	80.6
[137]	Chiral metasurface	Chiral molecule	NIR	220.9
	This work	Heomoglobin	Visible	533.3
		Glucose	NIR	596.7
		Cancer cell	MIR	2680.9

In real-world biosensing applications, environmental factors such as fluctuations in pH, temperature, and intermolecular interactions may cause slight variations in the refractive index of biological samples. However, such perturbations typically introduce only very small changes in refractive index, resulting in negligible resonance shifts that do not substantially affect the overall sensitivity of the sensor. Therefore, the proposed metasurface exhibits inherent stability under minor environmental variations. Nonetheless, larger deviations in environmental conditions may introduce undesired shifts in resonance, potentially leading to measurement inaccuracies. These limitations can be mitigated through practical strategies such as real-time referencing against control samples, implementing temperature stabilization protocols, or applying post-measurement correction algorithms. Such measures can ensure consistent sensor accuracy, making the proposed perovskite-based chiral metasurface a robust and reliable platform for practical biosensing applications in diverse environments.

4.5. Summary:

A chiral perovskite-based metasurface structure capable of generating strong circular dichroism (CD) in three distinct spectral regions—visible, near-infrared (NIR), and mid-infrared (MIR)—has been presented in this work. The observed dichroism originates from polarization-dependent interference produced by incident light interacting with neighboring nanostructures, where both the chirality of the design and the incorporation of multiple resonant cavities contribute to enhanced optical selectivity. By carefully tuning the geometric parameters associated with these resonant cavities, precise control over the magnitude and spectral position of CD has been demonstrated.

Beyond its fundamental optical response, the proposed structure has been explored for multifunctional biosensing applications. In the visible region, the metasurface functions as a

hemoglobin sensor, providing sensitivities of 520.1, 527.1, and 533.3 nm/RIU for different blood hemoglobin concentrations, thereby offering potential for monitoring clinically relevant conditions such as anemia or hypercoagulation. In the NIR region, the same device operates as a glucose concentration sensor, detecting sugar content in aqueous solutions with a maximum sensitivity of 596.7 nm/RIU, making it promising for medical diagnostics and food processing applications. Extending into the MIR region, the metasurface is shown to operate as a cancer cell detection sensor, achieving exceptionally high sensitivity, with a maximum value of 2680.9 nm/RIU for cervical cancer cells.

Taken together, these results establish that the perovskite-based chiral metasurface offers a highly versatile and multifunctional sensing platform. Unlike conventional sensors restricted to operation in a single wavelength region, the proposed structure demonstrates simultaneous applicability across visible, NIR, and MIR bands. This multifunctionality, combined with its strong CD response and high sensitivity, highlights the unique potential of perovskite chiral metasurfaces for next-generation biomedical sensing, where compact, integrated, and highly adaptive devices are increasingly in demand.

5

CHAPTER

Normal-Incidence Induced Chiral Metasurface for Perfect Absorbtion and Broadband Circular Dichroism

- *Introduces a concentric semi-circular ring–based chiral metasurface operating under normal incidence, moving beyond earlier oblique-incidence approaches.*
- *Demonstrates strong circular dichroism (CD ≈ 0.72) with near-perfect absorption (>99%) in the S and C optical bands through Fano resonances.*
- *Provides tunable control over resonance wavelength and CD magnitude by varying ring orientation and height.*
- *Confirms angular stability, maintaining high CD across incident angles from –25° to +25°.*
- *Establishes a 4×4 metasurface array with its mirror image for image encryption, polarization control, and noise suppression for secure optical communication.*

5.1. INTRODUCTION

In the preceding chapters, chiroptical responses were primarily engineered under oblique incidence, where extrinsic chirality is induced by the asymmetry between the illumination direction and the metasurface geometry. While this approach enables strong circular dichroism (CD), it also imposes practical limitations, as real-world optical communication and sensing systems generally operate under normal incidence[20,71,120,138,139]. For these applications, it becomes imperative to design metasurfaces that exhibit enhanced CD and perfect absorption at normal incidence, while also maintaining angular robustness.

Perfect absorption, achieved by suppressing both reflection and transmission, maximizes the confinement of optical energy within the device. This property underpins a wide range of functionalities including efficient photodetection, energy harvesting, and thermal emission control [140–142]. In parallel, strong CD ensures a distinct and differential response to left- and right-circularly polarized light, which is essential for polarization-sensitive optical communication, enantioselective biosensing, and advanced chiral photonics. Previous designs employing twisted nanostructures, L-shaped resonators, nanohole arrays, and cavity-based metasurfaces have demonstrated significant CD, but largely under oblique incidence [143–147].

For robust and scalable photonic platforms, achieving normal-incidence chirality with angular stability is a more practical and versatile route. Angular stability ensures that strong CD persists over a broad range of incidence angles, thereby reducing performance degradation in real-world operation. This capability is particularly critical for polarization multiplexing in communication systems, where distinct circular polarization channels are exploited to double

the data-carrying capacity, as well as for polarization-resolved imaging and sensing [74,75,105,138,148].

In this chapter, a semicircular concentric-ring-based chiral metasurface absorber is proposed, specifically optimized for normal incidence. The design operates across the optical S- and C-bands (1455–1557 nm) and achieves nearly perfect absorption alongside significantly enhanced CD. By introducing structural asymmetry through controlled variation of the ring height and rotational orientation, tunable control over resonance wavelength and CD magnitude is demonstrated. Importantly, the metasurface preserves strong CD over a broad angular range (–25° to +25°), validating its robustness. To extend the platform's potential, a 4×4 array composed of the unit cell and its mirror image is introduced, enabling functionalities such as polarization control, secure information processing, and dynamic signal manipulation across telecom-relevant bands.

5.2. Design parameters and Theory:

The designed metasurface chiral absorber is a three layer metal insulator metal (Au/SiO_2/Au) structure. Fig. 5.1 depicts the structural arrangement of the proposed metasurface absorber. The top layer, which consists of three Semi-Circular Rings (SCRs) is the key principle behind this conception. Fig. 5.1(a) shows the built of the three SCRs SCR 1, SCR 2, SCR 3 with parameters height h_1=305 nm, h_2=190 nm, h_3=30 nm, orientation angles α_1= 10°, α_2= -5°, α_3= 85°and width w_1=55 nm, w_2=95 nm, w_3= 90 nm respectively. The varying heights and alignment angles of these SCRs provide the necessary asymmetric factor leading to the strong CD. Fig. 5.1(b) shows the 3D view of the unit cell with a periodicity of 780 nm. Fig. 5.1(c) represents the incidence of left circularly polarized (LCP) and right circularly polarized (RCP) on the 5 x 5 array of the designed structure.

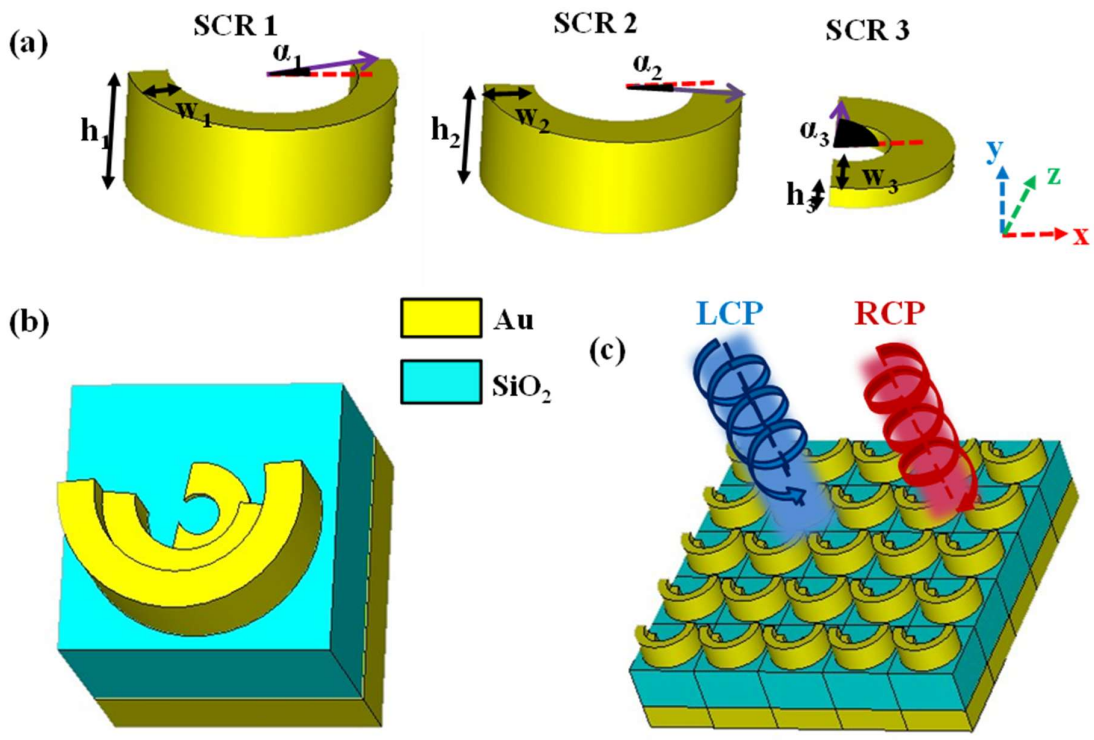

Fig. 5.1 (a) 3-d view of the three concentric SCRs being part of the unit cell (b) Perspective view of the proposed chiral metasurface unit cell (c) A 5 × 5 array of the SCRs based unit cells being incident to circularly polarized light.

The structure has a top layer made of gold, intermediate layer of SiO_2 which is 540 nm thick and a 300 nm thick gold layer is added to bottom to minimize the transmission. The dielectric functions of SiO_2 given by Ghosh et al.[149] and for gold(Au) given by Babar and Weaver et al.[88] have been used.

For circularly polarised incident light, the Jones matrix is employed to correlate the incident and reflected fields on a designated linear basis. The reflected field (E_r) is related to the incident field (E_i) and can be expressed as:

$$E_r = R_{CP} E_i \tag{5.1}$$

where R_{CP} denotes the reflection matrix. The Eq. 5.1 can be written in the form of matrix using Cartesian coordinate system as:

$$\begin{bmatrix} E_r^R \\ E_r^L \end{bmatrix} = \begin{bmatrix} r_{RR} & r_{RL} \\ r_{LR} & r_{LL} \end{bmatrix} \begin{bmatrix} E_i^R \\ E_i^L \end{bmatrix} \tag{5.2}$$

$$R_{CP} = \begin{bmatrix} r_{RR} & r_{RL} \\ r_{LR} & r_{LL} \end{bmatrix} \tag{5.3}$$

where $'r'_{ij}$ denotes the reflection coefficient with 'j' being the incident polarization and 'i' being the reflected polarization. The difference in the absorption of designed asymmetrical structure under two different rotationally circularly polarised light sources is referred to as circular dichroism calculated as:

$$CD = A_R - A_L \tag{5.4}$$

where A_L and A_R denote LCP and RCP light absorptions, respectively.

5.3. Results and Discussion:

5.3.1. Structural Design Analysis:

CST Microwave Studio has been used to model and study the suggested metasurface. The unit cell's periodic boundary conditions are applied along the x and y axes, and the wave propagation is along the z-axis. The Finite Element Method (FEM) is employed using a tetrahedral mesh, with a mesh density corresponding to 10 mesh lines per wavelength to ensure accurate field resolution. The structure is excited using left- and right-circularly polarized (LCP/RCP) light to analyze its chiral response. Since the metasurface with a metal backplane has zero transmission coefficients, a detailed analysis of its reflection properties is adequate. The circularly polarized field is incident along the negative z axis direction.

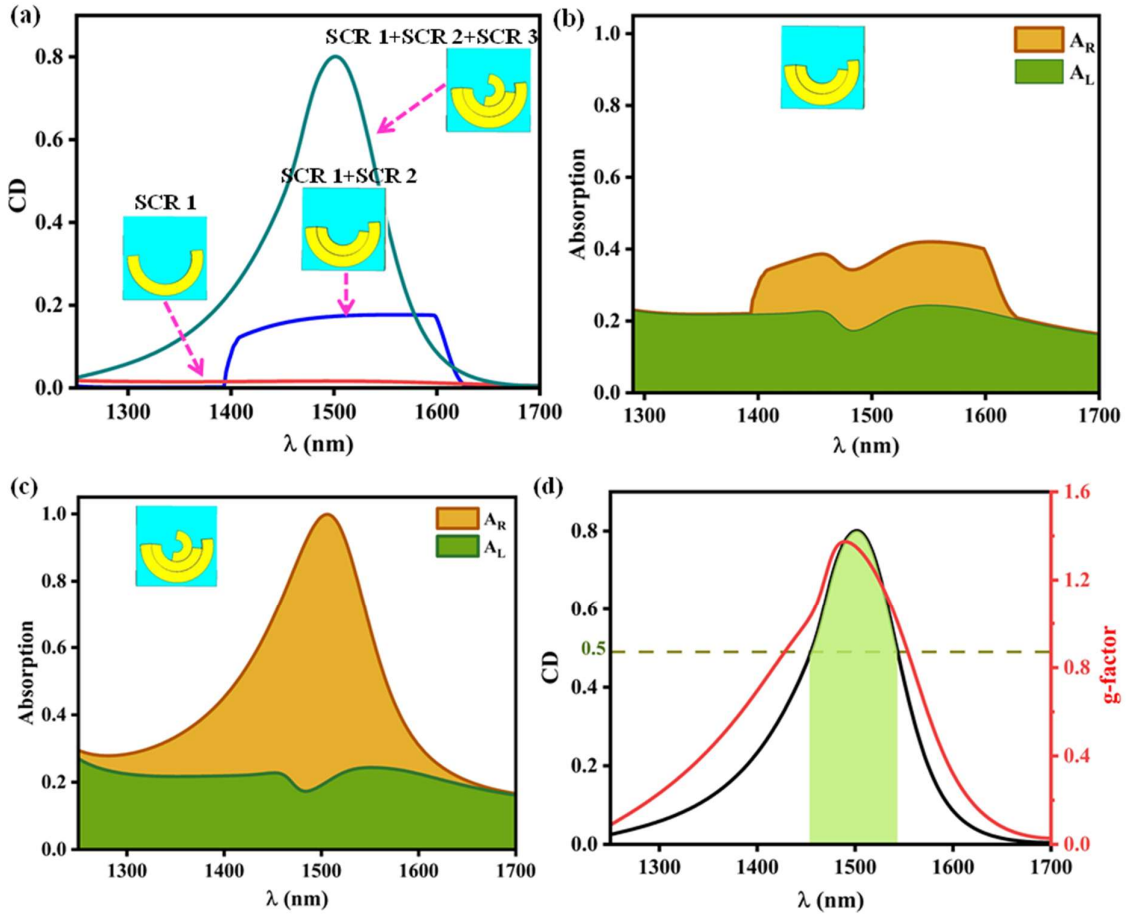

Fig. 5.2 (a) Structural examination of the unit cell culminating in the proposed design. (b) The absorption curve for SCR 1+ SCR 2 (c) The absorption curve for SCR 1+ SCR 2 + SCR 3 (d) CD curve and the g-factor of the metasurface for SCR 1+ SCR 2 + SCR 3

By altering the number of concentric SCR that influence the structure's asymmetry, a geometric investigation of the proposed metasurface was conducted. Fig. 5.2(a) shows the variation of CD with the structural variation of the unit cell as shown in inset figures. Clearly, the CD value for the SCR 1 + SCR 2 is higher (~0.2) compared to first configuration as the SCR 1 represents C4 symmetry with induced perturbation whereas for SCR 1 + SCR 2 symmetry breaking perturbation is introduced. Fig. 5.2(b) shows the absorption curve for SCR 1 + SCR 2 when

subjected to LCP and RCP light. Further, the third semicircular ring was added to the structure which efficiently increased the value of CD with maximum value being 0.82.

The absorption of the chiral proposed structure SCR 1 + SCR 2 + SCR 3 when subjected to LCP and RCP light is shown in Fig. 5.2(c) with A_R being the reason for high CD. At 1510 nm, a perfect absorption value of 100% is noted. Perfect absorption refers to a normalized absorptance value approaching 1 (or 100%) as A=1-T-R, where the sum of reflection(R) and transmission(T) is effectively zero. Also, high value of CD (>0.5) was obtained for the wide range i.e 1455 nm to 1557 nm covering the S and C bands leading to its potential applications in this optical window as shown by shaded region in Fig. 5.2(d). Additionally, to measure the differential absorption intensity holistically, CD is combined with the '*g-factor*' parameter. Fig. 5.2(d) shows the variation of *g-factor*[150,151] with wavelength for the complete structure where *g-factor* is the differential absorption intensity and is given by:

$$g - factor = \frac{A_R - A_L}{(A_R + A_L)/2} \tag{5.5}$$

5.3.2. Incident Angle Variation:

Fig. 5.3(a) and (b) show colour map of CD for various incident angle 'θ' and azimuthal angle 'φ'. The results show that the structure offers strong CD over wide incidence angle (θ) of -25° to 25°. As can be seen from Fig. 3(a) increasing the incident angle 'θ' generates second CD peak at lower wavelengths. The appearance of a second CD peak at higher incident angles is attributed to additional symmetry breaking induced by oblique illumination, which modifies mode coupling and allows new resonant interactions within the metasurface. This behavior is consistent with angle-dependent mode hybridization in asymmetric chiral structures. On the other hand, the structure offers great stability when the azimuthal angle is varied from -180° to 180° showing no effect of the change in azimuthal angle 'φ' as shown in Fig. 5.3(b). Essentially

because the projection of the incident wave vector onto the grating remains similar across azimuthal angles, preventing abrupt changes like Wood's anomalies.

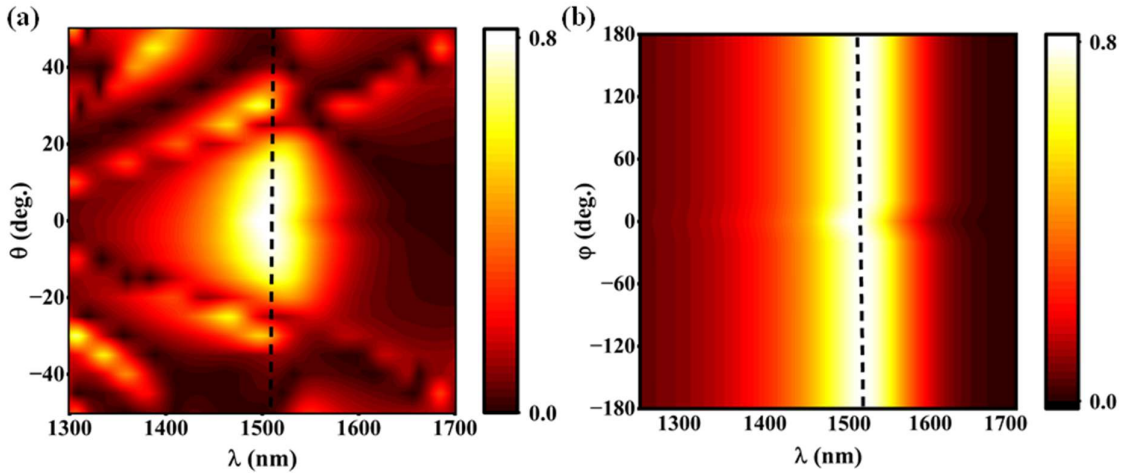

Fig. 5.3 The colour map of CD for the designed structure for different (a) incident angle (θ) (b) azimuthal angle (φ) of incident light.

The designed chiral metasurface offers high CD over the wide wavelength range with a greater angular stability in comparison to other previously designed chiral structures. Table 5.1 summarises the performance of the designed structure with the previous works designed for the similar wavelength region. The proposed metasurface employs a metal–dielectric–metal (MDM) architecture, which can be categorized as a hybrid design. Hybrid structures leverage the strong field enhancement capabilities of metal layers while using dielectric spacers to tune resonance conditions and improve absorption bandwidth. Compared to all-metal designs that suffer higher ohmic losses, or all-dielectric structures that often require larger dimensions to achieve comparable field confinement, hybrid metasurfaces provide a balanced approach. While dual-band metasurfaces can increase functionality, they typically involve greater design complexity and may exhibit lower CD in each band. Our MDM design offers a favourable trade-off between fabrication feasibility and broadband chiroptical performance.

Table 5.1 Comparison of performance with various chiral absorbers

Ref.	Operating Range	Central frequency	Bandwidth (BW)	BWxCD (nm)	Max. CD	Angular Stability
[152]	(1308-1323) nm	1315 nm	~10 nm	9.9	0.99	Not available
[139]	(1040-1200) nm	1110 nm	~50 nm	32.5	0.65	0^o to 10^o
[153]	(900-1500) nm	989 nm, 1404 nm	~40 nm	39.2	0.98	0^o to 40^o
[154]	(2100-2400) nm	2274nm, 2359 nm	~60 nm	42	0.7	Not available
[74]	(1550-1700) nm	1625 nm	~100 nm	70	0.70	Not available
This work	(1400-1600) nm	1510 nm	102 nm	82.62	0.81	-25^o to 25^o

5.4. Parametric Variation:

The Finite Element Method has been used to analyse and refine the suggested chiral metasurface in 1300-1700 nm wavelength range. In the designed metallic structure, Fano resonances are the dominant mechanism for achieving strong and wide range CD. The interference between a narrow discrete resonance and a wide resonance or continuum that overlap spectrally is an essential requirement for a Fano resonance[89,138,155–158]. Electric field distributions as shown in Fig. 5.4(a) at the resonance wavelength (1510 nm) and off-resonance wavelengths (1350 nm) reveal distinct modal behaviour. At the resonant wavelength of 1510 nm, strong near-field asymmetry and hybridized field patterns are observed, indicating strong interference. Whereas off-resonance profile at 1350 nm shows more isolated field localization. This supports the presence of Fano-like resonance driven by structural asymmetry. The Fano resonance perceived in the absorption spectra was quantitatively assessed by fitting both left circularly polarised (LCP) and right circularly polarised (RCP) responses as shown in Fig. 5.4(b) utilising the Fano formula:

$$I = I_0 \frac{(q\beta+\lambda-\ _0)^2}{(\lambda-\lambda_0)^2+\beta^2} \quad (6)$$

where 'λ_0' and 'β' are conventional parameters that indicate the position (resonance wavelength) and broadening of the resonance, respectively, 'I_0' being the normalization factor and 'q' is the designated Fano parameter, which characterises the degree of asymmetry. The solid lines represent the simulated resulted of the absorption whereas the dashed lines represent the fano fit absorption curves. For LCP light, the fit revealed a narrow linewidth (β = 0.46 nm) and weak asymmetry (q = 0.19), supporting the presence of Fano-like interference due to the broken symmetry in the metasurface. In contrast, RCP incidence exhibited stronger asymmetry with q = 5.44 centered around 1505 nm and a broad resonance with β = 94.38 nm. These results are consistent with prior reports where structural asymmetry was shown to trigger Fano resonances in chiral metasurfaces. This fano resonance can be tuned by varying the asymmetry parameters i.e. rotational angles of SCRs(α_1, α_2, α_3) and height of SCRs(h_1, h_2, h_3).

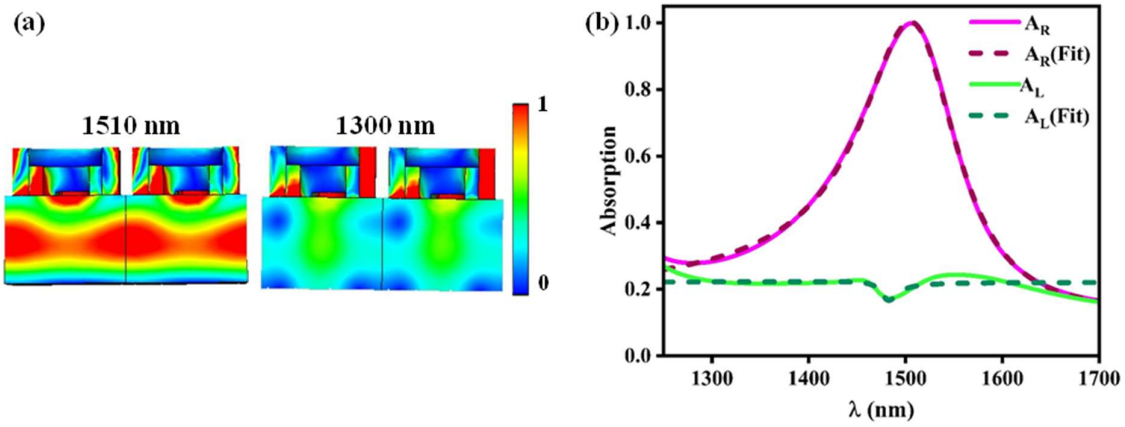

Fig. 5.4 (a) Side view of the Electric field distribution in the designed structure for the resonance wavelength 1510 nm and off resonance wavelength 1300 nm under RCP light incidence. (b) Fano fitting of the absorption curves A_R and A_L.

5.4.1. Effect of Rotational Angle of SCRs:

Fig. 5.5 illustrates the analysis of varying the rotational angles of SCRs (α_1, α_2, α_3). In the structure the localized surface plasmon resonance (narrow mode) from the SCRs interacts with the wider plasmonic scattering or delocalized modes of the overall structure and the variable rotational angles (α_1, α_2, α_3) regulate this interaction, boosting CD over a broad spectrum range. Varying the rotational angles majorly affect the width of the CD curve. Fig. 5.5(a) shows the variation in CD by varying rotational angle α_1. By increasing the value of α_1 from -15° to 5° CD value first increases and then decreases by further increasing the value of α_1. Rotational angle α_2 directly affects the width of the CD curve as by increasing the value of α_2 from -20° to 0°, CD value increases and then decreases by further increasing the value of α_2 giving the maximum peak value of CD for α_2= -10° shown in Fig. 5.5(b). Varying the rotational angle α_3 not only affects the peak value but also enormously shifts the resonance wavelength as shown in Fig. 5.5(c). The analysis shows by varying the rotational angles of the SCR, the resonance can be majorly tuned leading to the greater value of CD with wider bandwidth.

5.4.2. Effect of Height of SCRs:

Fig. 5.5 (d), (e), and (f) illustrate the analysis of varying the geometric height of the SCRs. Three SCRs of variable heights, instead of the SCR of equal heights provide an extra asymmetry factor enhancing the value of CD and finely tuning the resonance peak value. By varying h_1 the value of CD initially increases with the maximum value for 305 nm and then decreases as shown in Fig. 5.5(d). When h_2 is varied the value of CD remains almost constant with maximum value for 190 nm as shown in Fig. 5.5(e). Further, the value of CD and the bandwidth increase with variation in h_3, giving the maximum value at h_3 = 30 nm with a red

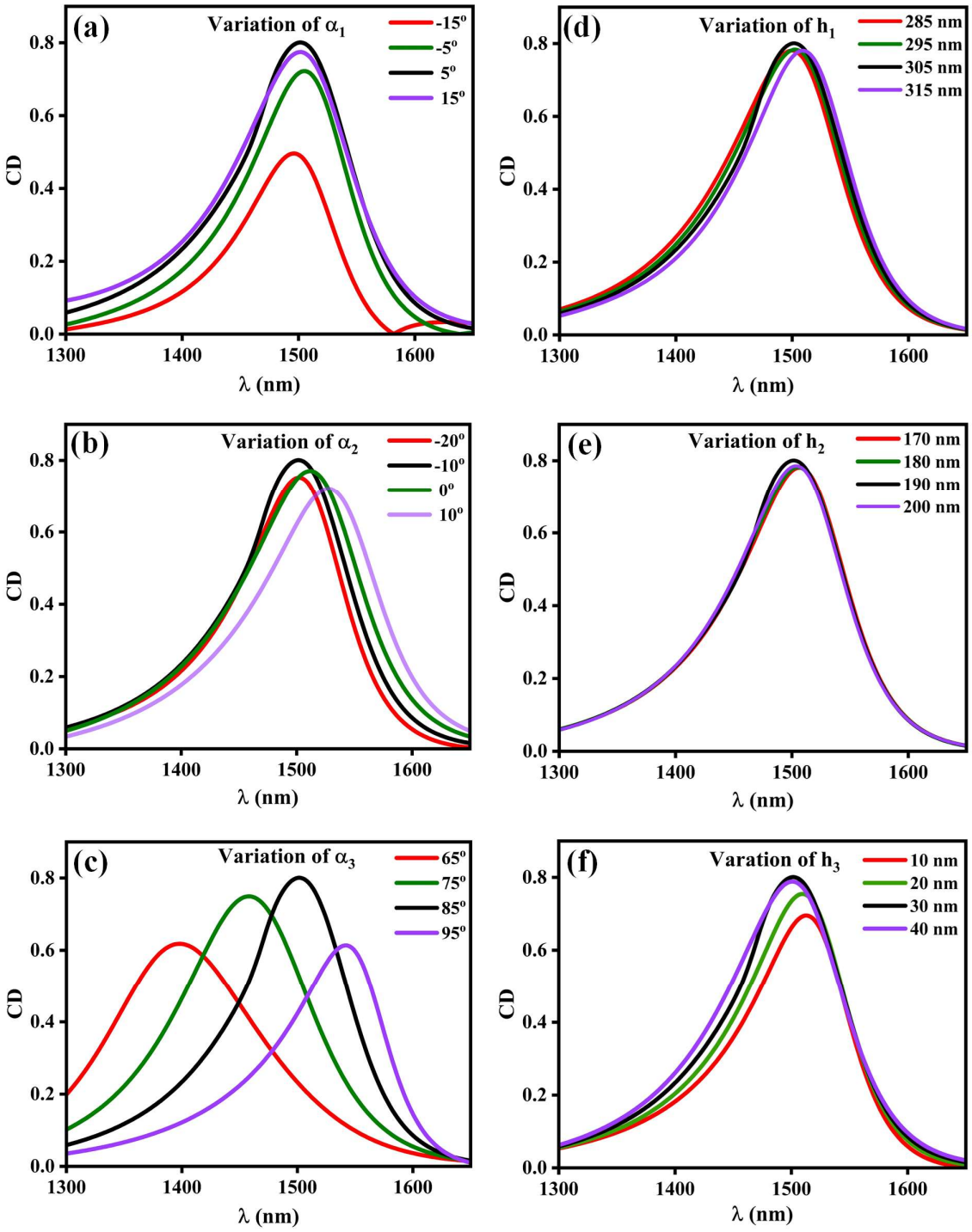

Fig. 5.5 Variation of circular dichroism with wavelength by varying rotational angles of SCRs (a) α_1, (b) α_2, (c) α_3 and height of SCRs (d) h_1, (e) h_2, and (f) h_3 for the proposed structure.

shift in the resonance wavelength. The analysis shows by varying the heights of the SCR the resonance can be finely tuned and leading to the higher peak value of CD.

The effect of the change in rotational angles and height of SCRs is quantitatively analysed in Fig. 5.6. The solid lines represent the shift in resonance wavelength with the change in parameter and dashed lines represent the shift in CD value with the variation in parameters. The third ring shows the strongest impact on the CD peak's spectral position and amplitude out of all the characteristics. Strong tunability through the manipulation of α_3 is shown by the significant spectrum shift of the resonance wavelength across a broad range. Variations in h_3 also efficiently alter the CD amplitude, but with a less influence on the resonance location. Conversely, alterations in α_1, α_2, h_1, and h_2 produce slight modifications. The results affirm that the third ring is essential to establish the optical chirality of the structure.

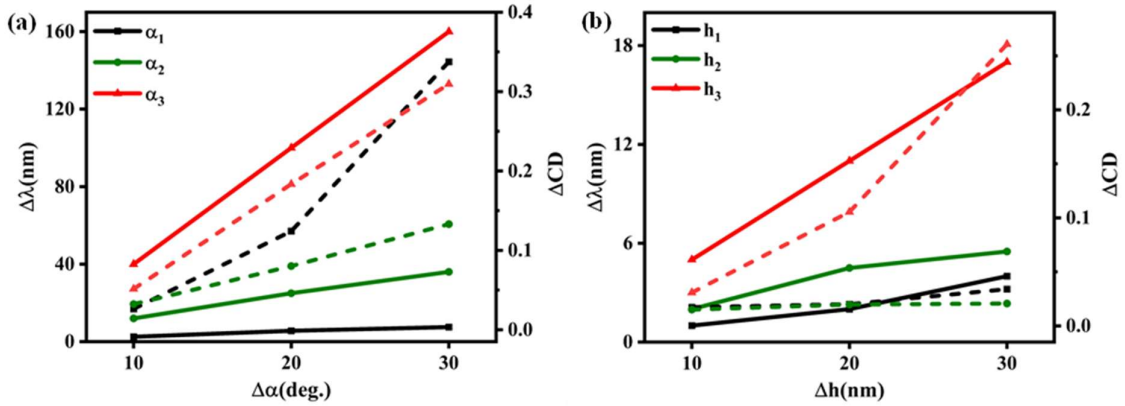

Fig. 5.6 Shift in resonance wavelength and circular dichroism by varying (a) rotational angles of SCRs α_1, α_2, α_3 and (b) height of SCRs h_1, h_2, h_3 for the proposed structure.

The proposed structure for the metasurface can be fabricated using well-established nanofabrication techniques. Thermal evaporation or sputtering can be used to produce the bottom layer of gold, and then plasma-enhanced chemical vapour deposition (PECVD) can be used to deposit SiO_2 dielectric. A multi-step electron beam lithography (EBL) procedure may

be used to print the top concentric gold arcs with different heights[159]. Each arc can be written in a distinct step, and overlay correction and lithographic marks are used to guarantee exact alignment. Height variation can be achieved by using resists of different thicknesses or through selective etching and controlled metal deposition[160,161]. Previous studies have demonstrated the feasibility of fabricating nanostructures with vertical step resolutions of ~30 nm and overlay accuracies better than 100 nm using advanced nanofabrication techniques and resist planarization techniques[162,163].

To better capture the realistic material behaviour of gold in the NIR regime, additional Drude–Lorentz dispersion model was implemented in CST simulations using FDTD method. Compared to the previously used experimental (n, k) data from Babar and Weaver using FEM model, the dispersion model more accurately accounts for inter-band transitions and increased damping. Parameters used were plasma frequency $\omega_p = 1.37\times10^{16}$ rad/s and collision frequency $\gamma = 1.2\times10^{14}$ 1/sec. This led to a blueshift in the resonance wavelength with minor decrease in CD value as shown in Fig. 5.7, demonstrating the robustness of the design even under realistic loss assumptions. Further, to assess the robustness of the metasurface under realistic fabrication errors, a Monte Carlo tolerance analysis was conducted. In this study, absolute variations of ±3 nm in the arc heights and periodicity, and ±3° in the angular orientations (α_1, α_2, α_3) were randomly introduced across 100 simulation iterations. For each iteration, the resonance wavelength was extracted, and the mean and standard deviation were computed. The resonance wavelength under tolerance variation yields a mean of 1504.5 nm with a standard deviation of ±4.6 nm, indicating that the proposed design maintains stable optical performance despite practical fabrication tolerances.

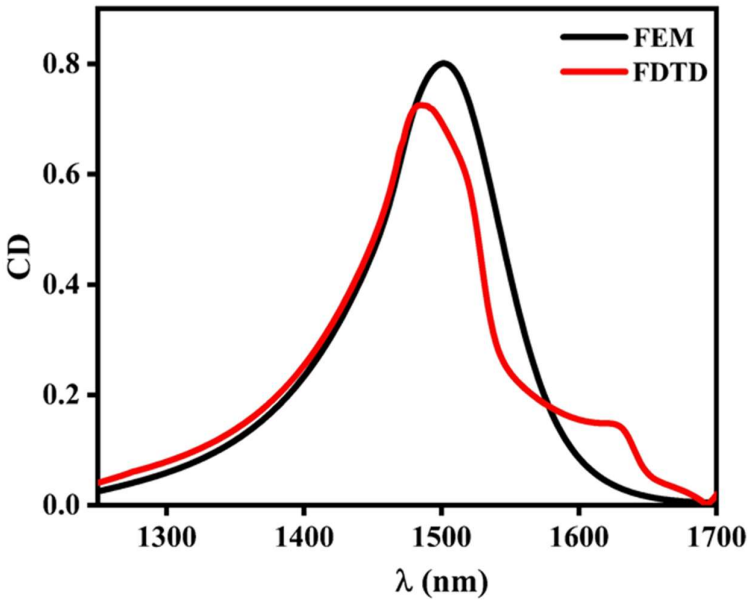

Fig. 5.7 Comparison of CD spectra obtained using FEM method and FDTD (Drude–Lorentz dispersion model) method.

5.5. Application:

From the analysis, it is comprehended that the basic principle of the designed chiral metasurface designated as Model I is to absorb RCP and reflect LCP providing high value of CD over wide range covering S and C bands. Similarly, its mirror image designated as Model II absorbs LCP and reflects RCP over the same range. The electric field intensity distribution of the Model I and Model II were analysed, considering the weak field response (<0.5) as '0' and strong field response (>0.5) as '1'. Table 5.2 shows the logical response of the designed metasurfaces Model I and Model II for the three different regions based on the polarization of the incident light.

Fig. 5.8(a) depicts a periodic structure with a 4 × 4 layout of the Model I and its mirror image designated as Model II. Fig. 5.8(b) represents the 3-dimentional view of the designed metasurface array projected to circularly polarized light. The first and third rows made of Model I absorb RCP and, second and fourth rows made of Model II absorb LCP. This chiral

metasurface may be used for near-field image encryption, polarization conversion and noise cancellation by utilising the periodic unit structure.

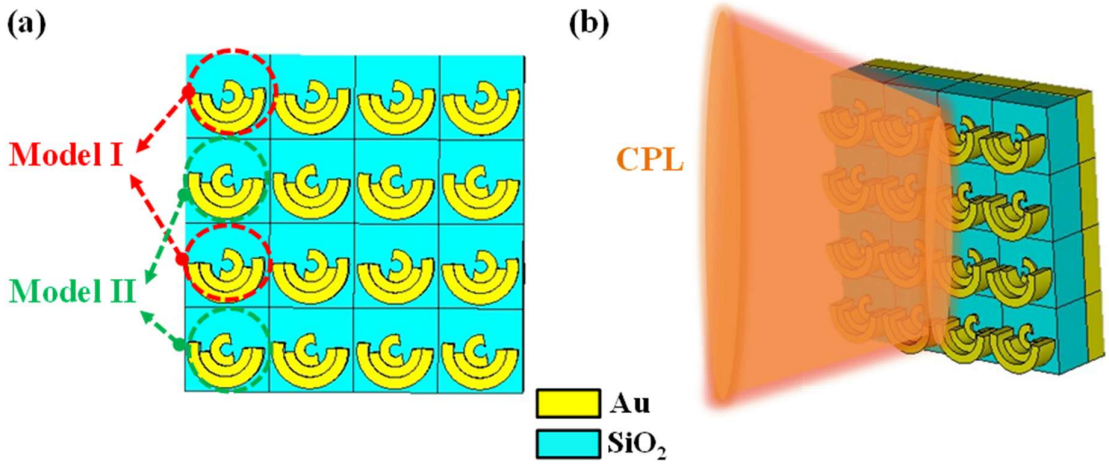

Fig. 5.8 (a) 2-d view of the designed 4x4 metasurface array where the first and third row consists of designed unit cell (Model I) and second and fourth row consists of its mirror image (Model II). (b) 3-d view of the designed array being projected to circularly polarized light (CPL).

Table 5.2. Logic response of the metasurface based on the polarization of incident light

Operating Range	Incident Light	Output	
		Model I	Model II
<1455 nm	LCP	1	1
	RCP	1	1
1455 nm-1557 nm	LCP	1	0
	RCP	0	1
>1557 nm	LCP	1	1
	RCP	1	1

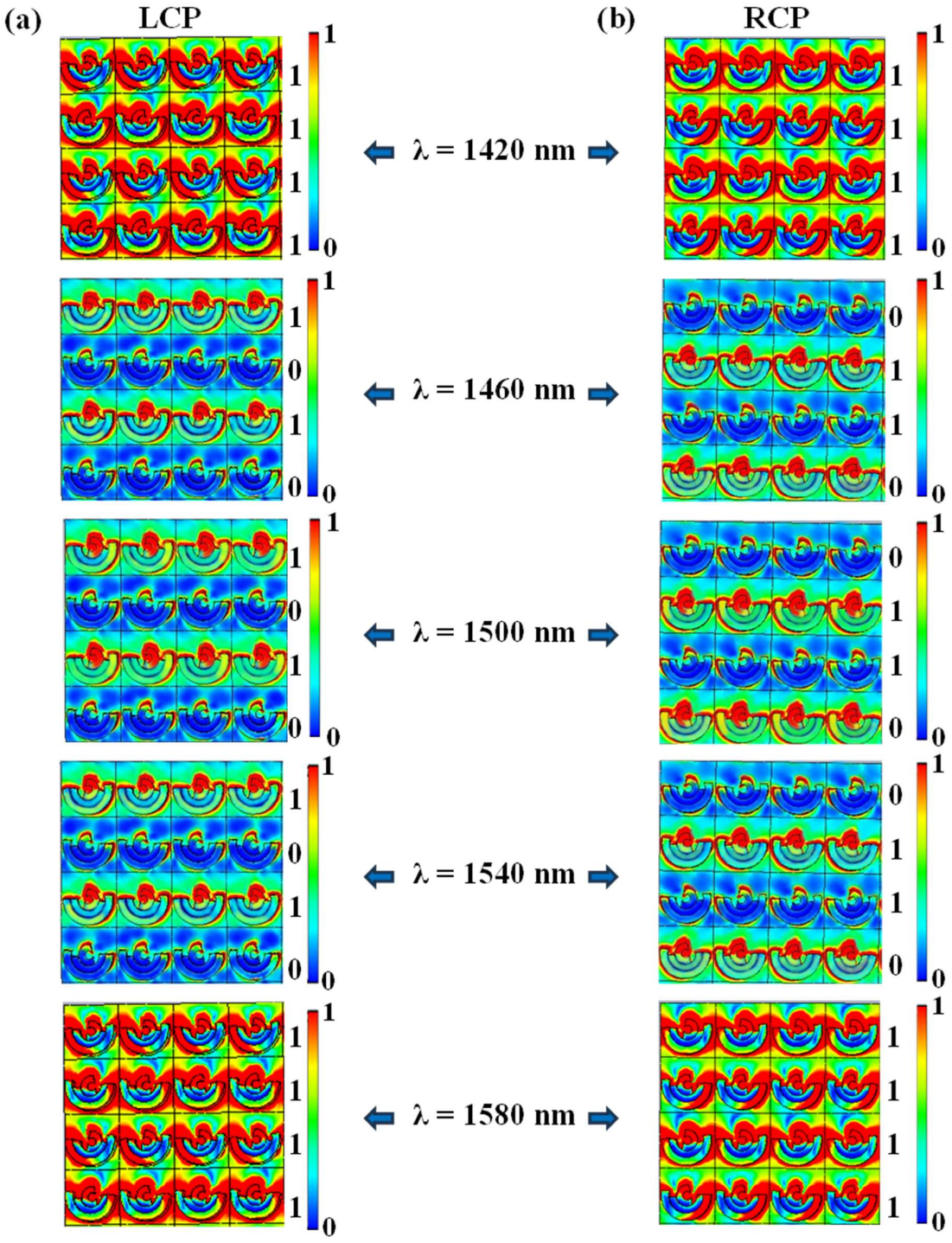

Fig. 5.9 (a) Electric field intensity distribution when the incident light is LCP, (b) Electric field intensity distribution when the incident light is RCP at different wavelengths.

Fig. 5.9(a) and 5.9(b) shows the electric field intensity response of the array for different wavelengths when incident light is LCP and RCP respectively. For incident LCP light the result is '1010' for wavelength range 1460 nm to 1540 nm and '1111' for remaining region as shown for λ=1420 nm and λ=1580 nm. And for incident RCP light the result is '0101' for wavelength range 1460 nm to 1540 nm and '1111' for remaining region as shown for λ=1420 nm and λ=1580 nm. This demonstrates how external dynamic modulation might interfere with the visual signal and thus encrypt it. Also it could be further used to filter out the noise/signal over broad range giving wide range of possible applications in optical communication. Further, the proposed metasurface encryption scheme operates in the near field, relying on evanescent field distributions for logic differentiation rather than far-field diffraction.

5.6. Summary:

In this chapter, an Au–SiO_2–Au chiral metasurface composed of concentric semicircular rings of varying heights was presented to achieve strong circular dichroism (CD) and perfect absorption under normal incidence. The structure demonstrated broadband performance with a maximum CD value of 0.81 and complete absorption at 1510 nm. Parametric analysis revealed that CD is highly sensitive to the rotational orientation of the rings and moderately influenced by their relative heights. Furthermore, the design exhibited remarkable angular stability, maintaining high CD across incidence angles from –25° to +25° and azimuthal variations from –180° to 180°.

To illustrate potential applications, a 4×4 metasurface array combining the unit cell and its mirror image was employed for near-field digital imaging, highlighting opportunities in optical communication, image encryption, and polarization control. While fabrication challenges such as multi-height patterning and orientation precision may introduce practical constraints, these

limitations are manageable within existing nanofabrication techniques. Future prospects include the incorporation of active or tunable materials to dynamically modulate CD, extending the applicability of the platform to real-time reconfigurable systems for communication, encryption, and advanced photonic sensing.

6

CHAPTER

Spin-Multiplexed Reflective Metalens Based on Chiral Metasurfaces

- *Provides a reflective chiral metasurface using enantiomeric Ω-shaped resonators in an Au–SiO_2–Au trilayer, achieving high circular dichroism (CD ≈ 0.78).*
- *Establishes spin-multiplexed metalensing, where left- and right-circularly polarized beams are focused into spatially distinct spots at (−10 μm, 0) and (+10 μm, 0).*
- *Demonstrates broadband focusing performance with peak efficiencies of 76.4% (LCP) and 75.8% (RCP), stable across the mid-infrared regime.*
- *Integrates selective absorption, polarization conversion, and wavefront shaping into a compact reflective platform with inherent background suppression.*
- *Exhibits dual-beam operation under mixed polarization input, supporting polarization-multiplexed imaging, secure optical communication, and spin-controlled information routing.*

6.1. INTRODUCTION:

The evolution of metasurfaces has reached a stage where the integration of multiple functionalities within a single platform is both desirable and increasingly feasible. The preceding chapters have established two complementary research pathways: the use of achiral metasurfaces to achieve broadband, polarization-insensitive metalensing, and the development of chiral metasurfaces capable of exhibiting strong circular dichroism (CD) under both oblique and normal incidence. Together, these directions reveal the dual potential of metasurfaces: achiral designs provide robust, broadband focusing without polarization sensitivity, while chiral architectures enable selective manipulation of spin-polarized light, offering functionalities such as polarization discrimination, enantioselective sensing, and spin-dependent imaging. A natural next step is the integration of these capabilities into a single compact platform that can simultaneously perform wavefront shaping and spin-selective light routing.

Traditional metalenses have already proven to be capable of high numerical aperture (NA) focusing, achromatic performance, and wide spectral operation. However, they remain largely limited in terms of polarization selectivity, treating incident light states equivalently. Conversely, chiral metasurfaces offer strong circular dichroism (CD), asymmetric transmission, and optical activity, yet most designs focus on selective absorption and spin filtering rather than phase-controlled imaging. Bringing these two classes together creates the opportunity to not only focus light but to encode and discriminate spin states at the same time, enabling a powerful set of functionalities within a single subwavelength-thick platform [164–170].

Building on these ideas, a spin-multiplexed reflective metalens that unifies chiroptical absorption with engineered phase control is designed. Enantiomeric Ω-type meta-atoms are arranged to impart opposite phase profiles for left- and right-circularly polarized inputs, steering them to spatially separated foci while maintaining low background via reflective perfect-absorber behaviour. The result is a single, planar platform that enables polarization-multiplexed focusing and spin-encoded image formation with resilience to bandwidth variations, capabilities that directly support next-generation optical communication and secure information processing. By combining principles of perfect absorption, chiroptical dichroism, and metalens-based wavefront engineering, this chapter establishes a multifunctional photonic device that not only advances the physics of light–matter interaction but also paves the way for applications in secure imaging, optical communication, and polarization-multiplexed information processing.

6.2. Device Configuration and Theoretical Framework:

6.2.1 Metasurface Architecture

The proposed device is a planar chiral metasurface designed to operate in reflection mode for spin-selective wavefront control and polarization-multiplexed focusing. It comprises a 40 × 40 array of subwavelength unit cells. Each unit consists of either an Ω-shaped designed meta-atom(DOM) or its mirror-symmetric counterpart i.e mirrored Ω-shaped meta-atom(MOM), arranged in a checkerboard configuration to achieve polarization-resolved functionality. The detailed geometry and optical properties of the constituent DOM and MOM unit cells are discussed in Section 6.3.1.

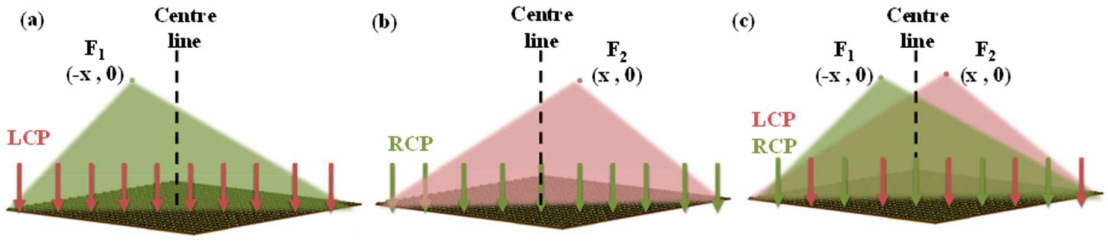

Fig. 6.1. Metasurface schematic showing polarization-resolved focusing: (a) LCP incident, (b) RCP incident, and (c) combined LCP–RCP illumination.

A schematic illustration of the metasurface layout and polarization-resolved focal behavior is presented in Fig. 6.1. Under left-handed circularly polarized (LCP) illumination, the original DOM elements selectively convert the incident spin state into right-handed circularly polarized (RCP) light and reflect it toward a focal spot located at $F_1(-x, 0)$. Simultaneously, the MOM elements absorb the LCP light, suppressing unwanted reflections as shown in Fig. 6.1(a). Conversely, for right-handed circularly polarized light, the MOM units become active, reflecting the converted LCP beam toward a distinct focus at $F_2(x, 0)$, while the DOM absorb the incoming RCP as shown in Fig. 6.1(b). When the incident field is a combination of LCP and RCP components, both channels operate concurrently: the DOM elements direct the LCP component to F_1, while the MOM elements route the RCP component to F_2. This results in the simultaneous formation of two spatially separated focal spots, each corresponding to its respective spin channel, with negligible cross talk due to the inherent spin selectivity and background suppression of the metasurface.

This spin-dependent routing mechanism enables the metasurface to operate as a dual-focus, polarization-multiplexed lens, effectively isolating and directing circular polarization channels to independent spatial locations. The integrated absorption of the orthogonal polarisation state

ensures background suppression, enhancing contrast and fidelity in polarization-encoded imaging or communication applications.

6.2.2. Analytical Model and Phase Engineering

The spin-dependent optical response of the proposed chiral metasurface is characterized by circular dichroism (CD) and geometric-phase-based wavefront shaping. Circular dichroism quantifies the difference in reflected intensity between right- and left-handed circularly polarized (RCP and LCP) light and is defined as:

$$CD = A_R - A_L \tag{1}$$

where A_{LCP} and A_{RCP} represent the absorption under left- and right-circularly polarized illumination, respectively. Each is computed as:

$$A_{R(L)} = 1 - R_{R(L)} \tag{2}$$

Here, R_R and R_L quantities are derived from the reflection Jones matrix:

$$R_{CP} = \begin{bmatrix} r_{RR} & r_{RL} \\ r_{LR} & r_{LL} \end{bmatrix} \tag{3}$$

where $'r'_{ij}$ denotes the reflection coefficient with 'j' being the incident polarization and 'i' being the reflected polarization.

The reflected electric field for circularly polarized incident light is given by:

$$E_{Out} = R(\theta).E_{In} \tag{4}$$

where R(θ) is the reflection matrix that depends on the meta-atom's geometry and rotation angle θ. The phase imparted to the reflected wave is determined by full-wave electromagnetic interactions and numerically calculated for each rotation angle[171]. To enable spin-selective wavefront shaping, the metasurface is composed of meta-atoms rotated according to a position-

dependent prescription. The target phase profile for focusing at a point (x_f, y_f) with focal length f is given by:

$$\varphi = \frac{2\pi}{\lambda}\left(\sqrt{(x - x_f)^2 + (y - y_f)^2 + f^2} - f\right) \quad (5)$$

where λ is the design wavelength and (x, y) are the in-plane coordinates of each meta-atom. Each unit is rotated by a specific angle θ, pre-determined via simulation to produce the required phase response upon reflection for a given spin state.

Because the metasurface contains alternating original and mirror-image meta-atoms, LCP and RCP incident light experience different reflection pathways: one handedness is converted and focused, while the other is absorbed. This architecture enables spatial separation of spin components while suppressing unwanted background light.

6.3. RESULT AND DISCUSSION:

6.3.1. Structural Design and Chiroptical Response:

The proposed metasurface is composed of an array of chiral Ω-shaped plasmonic meta-atoms engineered to perform polarization-selective reflection and focusing in the mid-infrared regime. Each unit cell consists of a tri-layered structure comprising a 200 nm thick gold ground plane, a dielectric spacer SiO_2 of ~400 nm thickness, and a patterned gold top layer forming the functional meta-atom. This reflection-mode configuration ensures zero transmission, allowing precise tailoring of reflected spin channels via structural asymmetry.

Fig. 6.2(a) shows the layout of the unit cell, featuring an Ω-shaped resonator with tailored asymmetry to break both mirror and n-fold rotational symmetries, essential for inducing strong circular dichroism. The meta-atom consists of a curved horseshoe-like outer loop intersected

asymmetrically with arm extensions and gaps to introduce optical chirality. The structure's geometry promotes spin-selective plasmonic resonances, enabling one polarization to be reflected and converted efficiently while the opposite is absorbed. Its mirror-image counterpart, shown in Fig. 6.2(b), exhibits an identical magnitude of optical response but reversed spin selectivity. Together, these enantiomeric unit cells form the basis of the spin-multiplexed metasurface. The proposed Ω-shaped resonator array is readily fabricable using standard electron-beam lithography, metal deposition, and lift-off processes on a SiO_2 dielectric spacer with an Au backplane. Similar chiral plasmonic elements have been experimentally realized and reported in [172,173], confirming practical feasibility. The feature dimensions (arm width ≈ 50 nm, gap > 40 nm) and a moderate aspect ratio below (defined as metal thickness / arm width) ensure structural robustness and reliable pattern transfer. Moreover, the reflective Au–

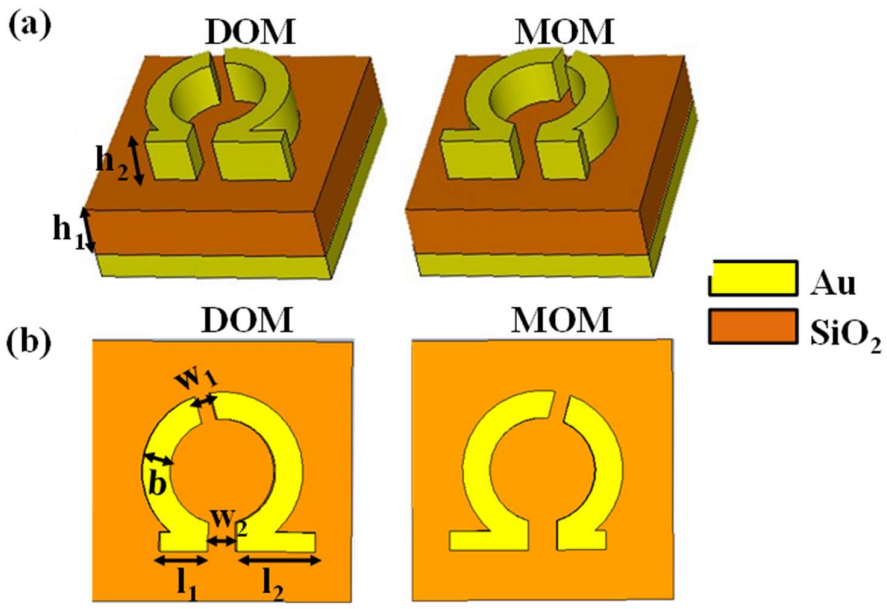

Fig. 6.2. Ω-shaped (DOM) and mirror-Ω (MOM) meta-atom designs: (a) 3D view of the unit cells, highlighting structural asymmetry for chiroptical response, and (b) 2D top view with labelled geometric parameters.

SiO_2–Au architecture simplifies alignment and enhances durability. Hence, the proposed design is compatible with established nanofabrication infrastructure and robust under typical process tolerances.

A corresponding two-dimensional top view is shown in Fig. 6.2(b), where all geometric parameters are labeled. The unit cell dimensions include the periodicity 'p', width of cavities 'w_1' and 'w_2', thickness of Ω resonator 'b' and length of left and right arms 'l_1' and 'l_2'. These parameters were optimized to maximize absorption asymmetry at the design wavelength in the mid-infrared regime. The dielectric constants for gold and SiO_2 are taken from experimentally validated sources given by Babar and Weaver et al.[88] and Ghosh et al.[149] respectively to ensure simulation accuracy.

The electromagnetic response of the unit cells was simulated using CST Microwave Studio, applying the frequency-domain solver based on the Finite Element Method (FEM). Periodic boundary conditions were implemented along the x- and y-axes, and the structure was excited by left- and right-handed circularly polarized (LCP/RCP) plane waves incident from the negative z-direction. Fig. 6.3(a) and 6.3(b) present the reflection S-parameters and corresponding absorption and CD spectra for the designed Ω-shaped meta-atom (DOM), while Fig. 6.3(c) and 6.3(d) display the same for its mirrored counterpart (MOM). These results are obtained under circularly polarized illumination and provide insight into the spin-resolved electromagnetic behavior of the unit cells. As shown in Figure 3(a), the DOM structure exhibits dominant cross-polarized reflection r_{rl}, where incident LCP light is efficiently converted to RCP upon reflection. The co-polarized term r_{ll} remains significantly suppressed across the operating bandwidth, confirming strong polarization conversion efficiency. This behaviour is consistent with the underlying chiral asymmetry in the geometry, which induces spin-selective

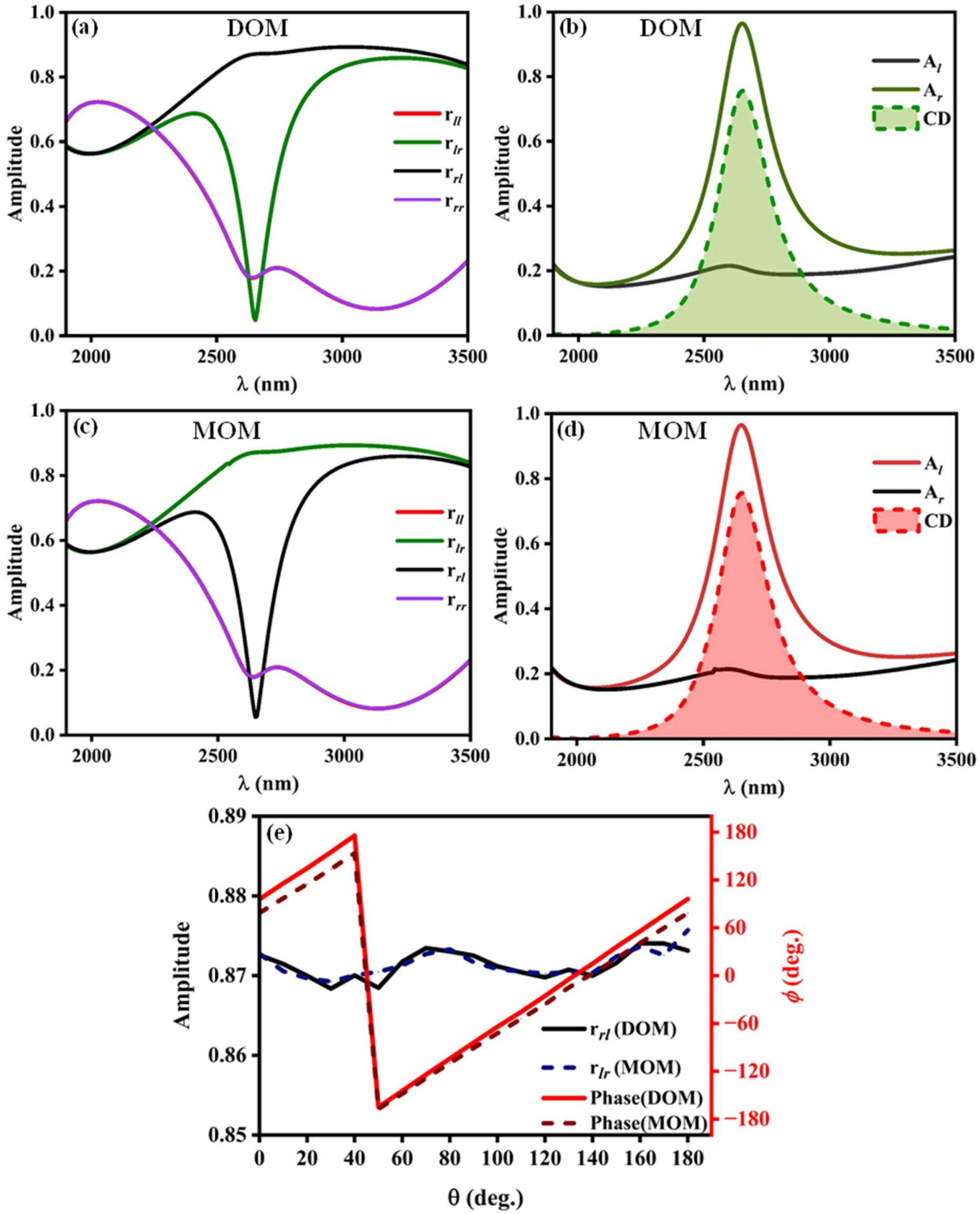

Fig. 6.3. Optical response of the designed meta-atoms: (a) reflection S-parameters and (b) corresponding absorption and CD spectra of DOM. (c) Reflection S-parameters and (d) corresponding absorption and CD spectra of MOM, and (e) cross-polarized reflection amplitude $r_{rl/lr}$ and phase ϕ as functions of rotation angle θ for both DOM and MOM, demonstrating full phase coverage with stable amplitude.

interference and anisotropic current pathways. In contrast, the response to RCP illumination is minimal, with reflection largely absorbed due to the metallic backplane and dissipative losses in the structure.

The corresponding absorption and circular dichroism characteristics for DOM are plotted in Fig. 6.3(b). Absorption is calculated as A=1-R, with transmission being zero due to the reflective design. A clear asymmetry is observed between LCP and RCP absorption, resulting in a peak CD value of approximately 0.78 at the design wavelength. This strong chiroptical activity is indicative of highly spin-selective light–matter interaction, with DOM preferentially interacting with one handedness while suppressing the other.

Fig. 6.3(c) and 6.3(d) demonstrate the complementary optical response of the MOM structure. As seen in Fig. 6.3(c), the mirror-image unit cell exhibits strong cross-polarized reflection r_{lr}, indicating efficient conversion of RCP to LCP. The corresponding co-polarized term r_{rr} remains negligible, and LCP input is largely absorbed. The mirrored design maintains the same geometric parameters but reverses chirality, thus responding to the opposite spin state. The absorption and CD spectra in Fig. 6.3(d) further validate this behavior. The CD curve mirrors that of the DOM structure in shape and magnitude but with an opposite handedness, peaking at ~0.78, confirming polarization-opposite selectivity.

This reciprocal behaviour between DOM and MOM meta-atoms underpins the metasurface ability to function as a dual-channel spin router. By spatially encoding these two unit cells across the aperture, the metasurface achieves simultaneous polarization conversion, background suppression, and spin-resolved focusing, all critical functionalities for next-generation optical systems involving polarization multiplexing, secure communication, and chiral photonic logic.

To achieve complete phase coverage, the top resonator of each meta-atom is rotated in-plane, enabling continuous modulation of the reflected wavefront. Fig. 6.3(e) presents the resulting cross-polarized reflection amplitude $r_{rl/lr}$ and phase ϕ as functions of the rotation angle θ for both DOM and MOM unit cells. The phase response spans the full 0°–360° range, ensuring that any required local phase shift can be implemented across the metasurface aperture. Throughout this tuning range, the reflection amplitude remains nearly constant at ~0.87 for both

enantiomeric designs, indicating minimal insertion loss variation. Such a combination of full-phase tunability and amplitude stability is essential for precise spatial wavefront engineering and high-efficiency focusing in both spin channels.

6.3.2. Spin-Selective Phase Profile Design:

To realize polarization-multiplexed focusing, the metasurface was engineered to impart two spatially distinct reflection phase profiles, each tailored to a specific circular polarization state. The design objective is to focus incident LCP light to the point (–10 μm, 0) and RCP light to (+10 μm, 0), thereby enabling spatial separation of spin states within a single compact platform.

Using the focusing phase formalism described previously in Section 6.2.2, two target phase distributions were calculated, corresponding to the desired focal positions for LCP and RCP beams as shown in Fig. 6.4(a) and (b) respectively. These phase profiles were then discretized and mapped onto the metasurface layout by assigning appropriate meta-atom geometries at each spatial location. The Ω-shaped unit cells were used to implement the LCP-specific phase profile, while the mirror-Ω structures were assigned to the RCP profile. Each meta-atom thus locally imposes the required phase delay to steer the reflected beam toward its designated focal point.

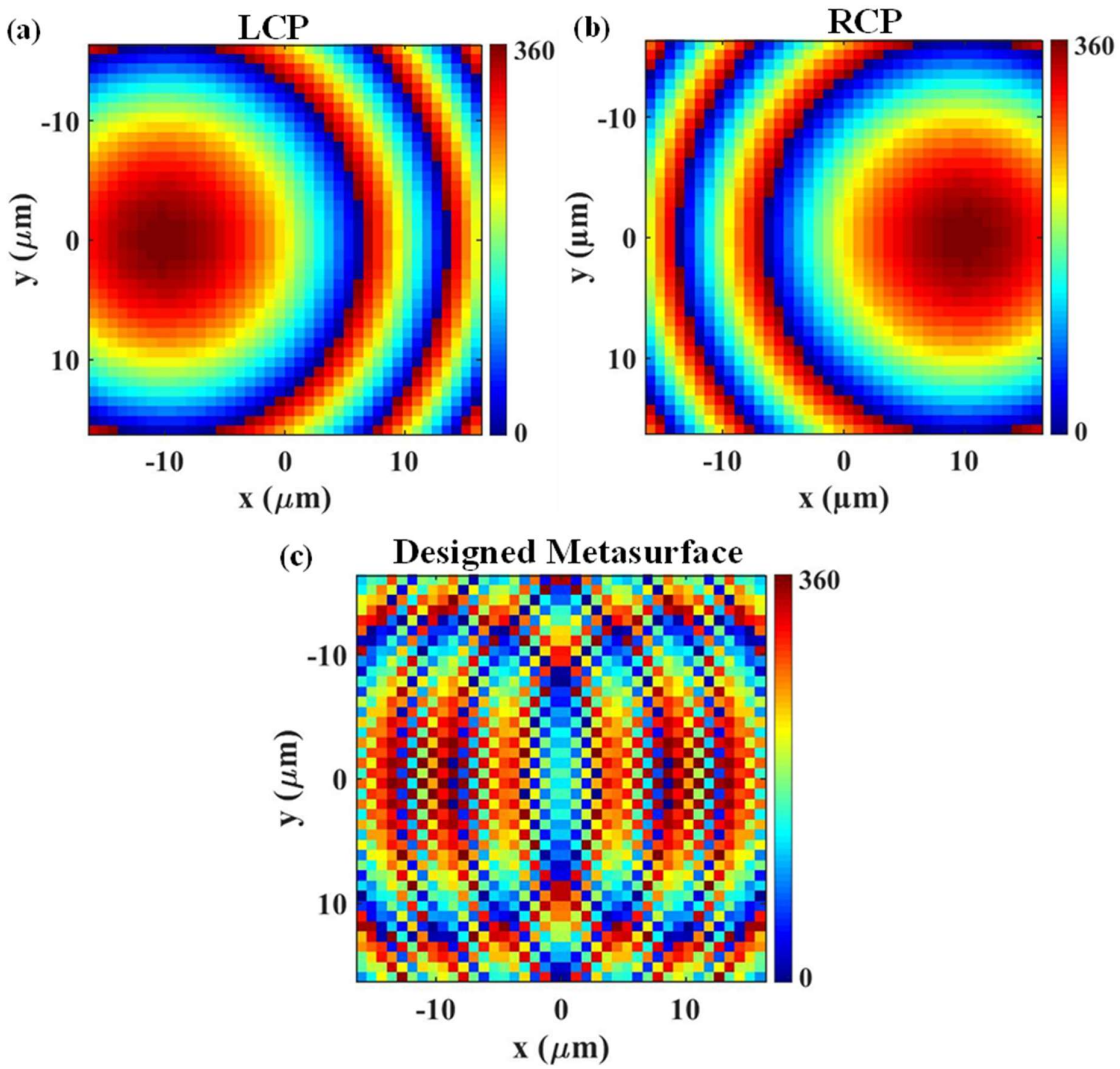

Fig. 6.4. Target phase distribution (a) for LCP focusing at F_1(-x, 0), (b) for RCP focusing at F_2(x, 0). (c) Designed phase distribution from the combined interleaved DOM and MOM unit cells enabling dual-beam polarization-multiplexed focusing.

The final metasurface layout consists of alternating Ω and mirror-Ω unit cells arranged across a 40 × 40 grid. Under LCP illumination, the DOM elements dominate the optical response, reflecting and converting the incident light to RCP and directing it toward the left focal point. Simultaneously, the mirror-symmetric meta-atoms MOM passively absorb the LCP component, minimizing unwanted scattering and enhancing contrast. Conversely, under RCP illumination, the MOM elements become the active contributors, converting RCP to LCP and

focusing it to the right-side focal position, while the DOM cells absorb the incident RCP. Fig. 6.4(c) presents the combined phase distribution that results from the spatially interleaved arrangement of enantiomeric unit cells. The resulting metasurface thus enables dual-beam spin-selective focusing with built-in polarization filtering, offering promising functionality for polarization-multiplexed imaging, secure optical communications, and parallel information encoding systems.

6.3.3. Focal Field Distribution and Polarisation Discrimination:

To verify the spatial and spectral performance of the spin-multiplexed metalens, the reflected electric field intensity was simulated at the focal plane under LCP and RCP incidence conditions respectively. The spin-dependent focal spots are visualized in Fig. 6.5, where Fig. 6.5(a) and 6.5(b) show the field intensity maps for the DOM and MOM-based focusing, respectively. Each structure selectively redirects the incident circularly polarized light to its corresponding focus: the DOM routes LCP light to (−10 μm, 0) while the MOM routes RCP light to (+10 μm, 0), consistent with the encoded phase profiles and spin-channel discrimination strategy.

To further evaluate the broadband spectral response of the metasurface, Figs. 6.5(c) and 6.5(d) present the normalized field intensity distributions at selected wavelengths (2630 nm, 2654 nm, 2670 nm, and 2690 nm) for the LCP (DOM) and RCP (MOM) channels, respectively. Across both spin channels, the focal spots remain sharply localized along the transverse axis, with minor shifts in the peak position as the operating wavelength deviates from the design wavelength of 2654 nm.

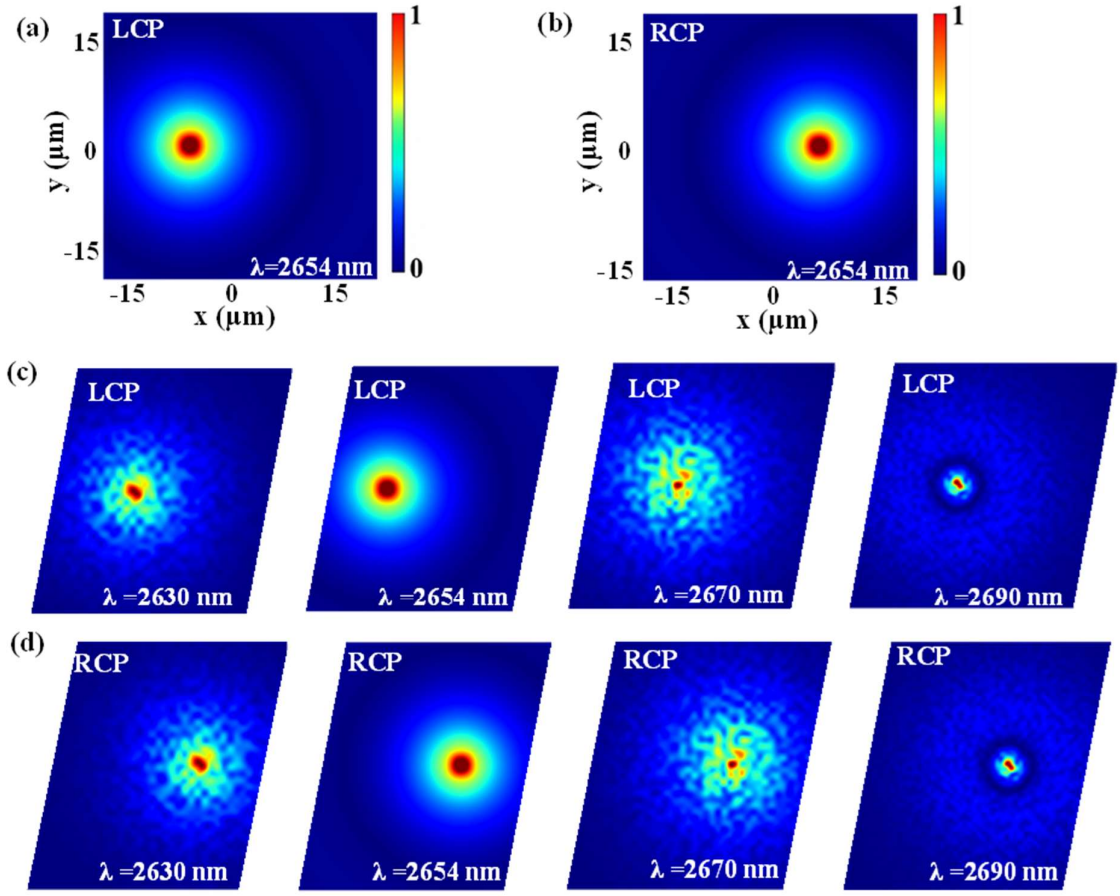

Fig. 6.5. Focal spot profiles under circularly polarized excitation. The top row shows well-confined focal spots at the design wavelength λ = 2654 nm for LCP (left) and RCP (right) incidence. The bottom two rows present the broadband response across nearby wavelengths (2630, 2654, 2670, and 2690 nm), demonstrating stable focusing performance with slight variations in confinement and intensity for both polarization channels.

The focusing performance of the metasurface is first evaluated at the design wavelength of 2654 nm. As shown in Figs. 6.6(a) and 6.6(b), the transverse intensity distributions corresponding to the DOM (LCP) and MOM (RCP) channels exhibit sharply confined focal spots with symmetric profiles and negligible sidelobes. This clean and isolated focusing response highlights the strong spin-selectivity of the metasurface, with minimal background contributions or undesired cross-polarization leakage at the design point.

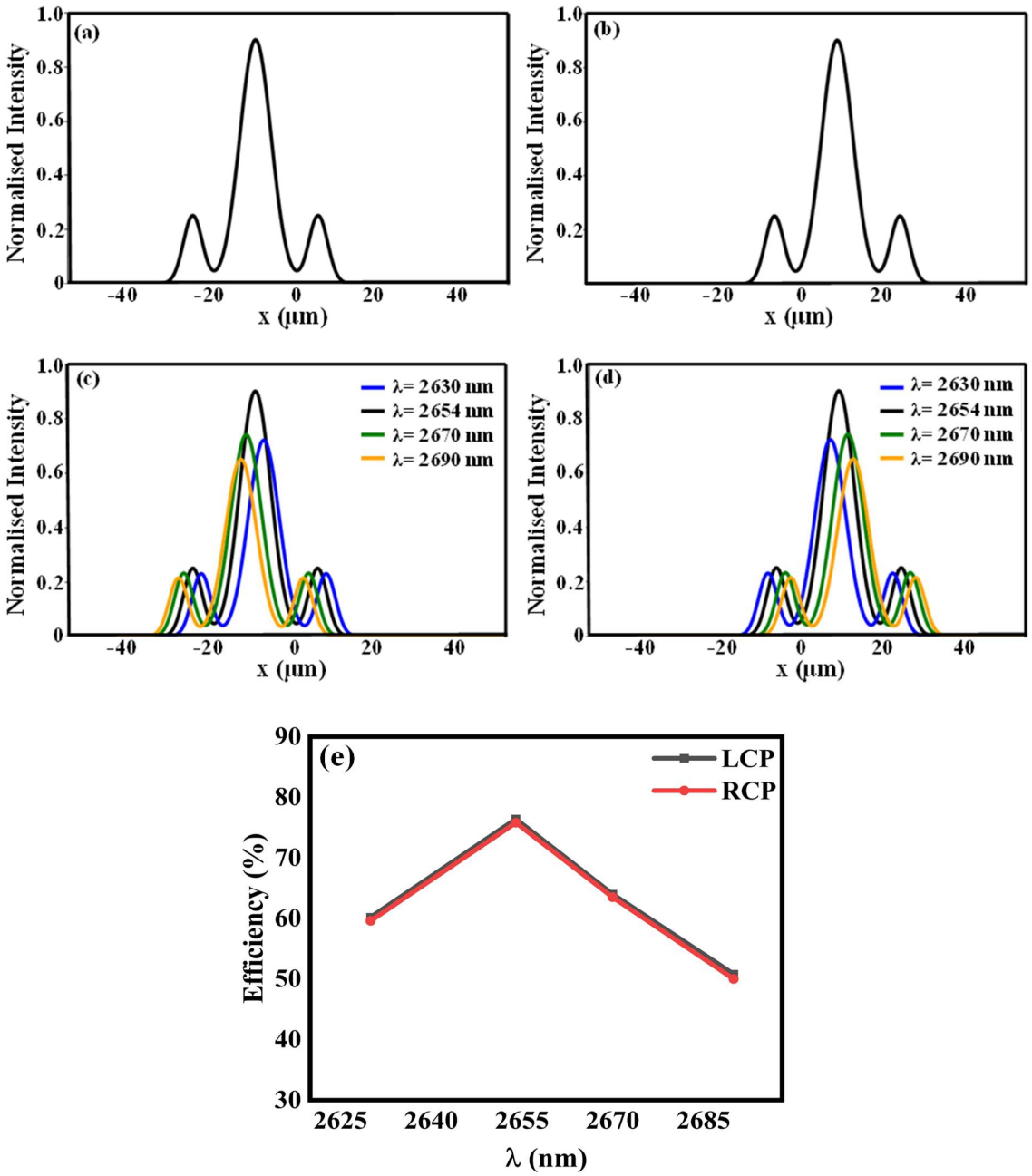

Fig. 6.6. Spin-resolved focusing performance of the proposed metasurface. (a) and (b) Normalized intensity distributions at the focal plane for incidence LCP and RCP excitation respectively for the target wavelength 2654 nm. (c) and (d) Wavelength-dependent normalized field intensity profiles along the transverse x-axis for LCP and RCP incidence, respectively, demonstrating stable confinement with slight shifts in peak position. (e) Variation of diffraction efficiency with wavelength for both channels, confirming comparable broadband performance across the mid-infrared regime.

To further assess the spectral robustness, the normalized intensity distributions at multiple nearby wavelengths (2630 nm, 2654 nm, 2670 nm, and 2690 nm) are presented in Figs. 6.6(c) and 6.6(d). Across both spin channels, the focal spots remain well localized and symmetric, with only minor shifts in the peak position as the operating wavelength deviates from resonance. Importantly, the separation between the LCP and RCP foci shows a weak wavelength dependence: shorter wavelengths (2630 nm) bring the focal spots slightly closer together, while longer wavelengths (2670–2690 nm) lead to marginally wider separation. This effect arises from the dispersion of the metasurface phase profile, where the wavelength-dependent optical path length alters the constructive interference conditions that define the focal position[174,175].

The diffraction efficiency (η_d) was evaluated as the ratio of the optical field energy enclosed within a circular area of radius three times the full width at half maximum (3×FWHM) around the focal spot to the total optical power across the focal plane[176]. The corresponding diffraction efficiency as a function of wavelength is summarized in Fig. 6.6(e). Both LCP and RCP channels display nearly identical responses, with peak efficiencies of 76.4% for LCP incidence and 75.8% for RCP incidence at the design wavelength of 2654 nm. A gradual decrease is observed toward the spectral edges, yet the efficiency consistently remains above 50% across the investigated range. Physically, this demonstrates that the device not only maintains efficient spin discrimination but also suppresses chromatic dispersion, making it highly attractive for practical applications requiring robust performance, such as polarization-multiplexed imaging, spin-controlled information routing, and broadband mid-infrared optical interconnects.

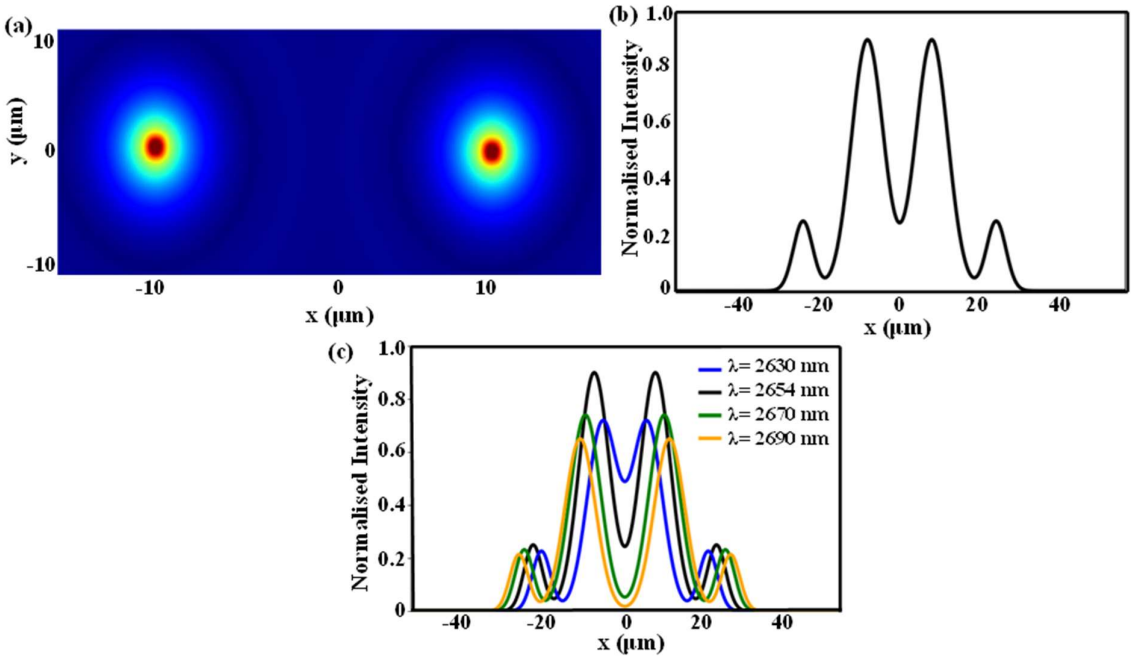

Fig. 6.7. Dual-channel focusing behavior under combined LCP and RCP illumination. (a) Intensity distribution at the focal plane showing two well-separated spots corresponding to polarization-resolved foci. (b) Normalized transverse intensity profile at λ = 2654 nm confirming symmetric dual peaks with negligible crosstalk. (c) Broadband response for λ = 2630 nm, 2654 nm, 2670 nm, and 2690 nm, demonstrating consistent dual-beam focusing with slight spectral variation in peak intensity and position.

The metasurface response under simultaneous excitation by LCP and RCP illumination is shown in Fig. 6.7(a). The reflected field distribution exhibits two well-resolved focal spots symmetrically positioned at (−10 μm, 0) and (10 μm, 0), corresponding to the selective routing of LCP and RCP components by the DOM and MOM elements, respectively. The normalized transverse intensity profile in Fig. 6.7(b) confirms the presence of two distinct peaks with negligible overlap, demonstrating efficient channel isolation and strong spin discrimination. This clean separation indicates that the metasurface functions as a polarization-division

multiplexer, where each spin state is independently mapped to its designated spatial channel without cross-talk or background interference.

The broadband performance under dual-spin excitation is further analyzed in Fig. 6.7(c), where the normalized intensity distributions at the focal plane are plotted for wavelengths 2630 nm, 2654 nm, 2670 nm, and 2690 nm. Across this spectral range, both focal spots remain sharply defined and nearly symmetric, with only minor reductions in peak intensity away from the design wavelength. Importantly, the relative spacing between the two focal spots exhibits a systematic trend with wavelength: as the wavelength decreases below 2654 nm, the focal spots shift slightly closer together, whereas at longer wavelengths, the spots move farther apart. This behaviour originates from the intrinsic wavelength dependence of the phase gradient imparted by the metasurface, where shorter wavelengths accumulate a larger effective phase shift per unit cell, resulting in reduced focal separation, while longer wavelengths produce the opposite effect.

Despite these spectral variations, the dual-spot profile is preserved throughout, confirming the robustness of spin-selective focusing. Physically, this implies that the metasurface maintains reliable spatial encoding of polarization channels even under spectral detuning, a property highly beneficial for polarization-multiplexed imaging, optical interconnects, and logic operations. The negligible overlap between channels ensures minimal cross talk, thereby enabling the metasurface to operate as a functional analog of a two-output logic gate, where distinct spin inputs are deterministically routed to separate output locations.

The functional response of the proposed metasurface can be interpreted as a polarization-controlled binary decoder. As summarized in Table 6.1, the two input states correspond to the presence or absence of LCP and RCP illumination, while the outputs represent the focal spots

F_1 and F_2. When no polarization is applied, no output is generated (0,0). For single-spin excitation, only the corresponding focal spot is activated: LCP produces F_1 while RCP produces F_2. Under dual-spin excitation, both outputs are simultaneously generated, yielding (1,1). This direct mapping realizes a 2-to-2 decoding operation, where the metasurface translates the polarization basis of the input into distinct spatial channels without crosstalk. Such a decoder-like functionality highlights the deterministic spin selectivity of the design and demonstrates its potential as a building block for polarization-encoded information routing and optical logic.

Table 6.1. Polarization-controlled binary decoder response of the metasurface

Operating Range	Incident Light		Output	
	Input A(LCP)	Input B(RCP)	F1	F2
2620 - 2690 nm	0	0	0	0
	1	0	1	0
	0	1	0	1
	1	1	1	1

This dual-channel reflective metasurface combines high chiroptical contrast, directional focusing, and spectral robustness within a geometrically compact design. A comparative analysis with previously reported multiplexed metasurfaces is presented in Table 6.2. The proposed Ω-resonator reflective metasurface outperforms prior designs by achieving a higher diffraction efficiency (≈76 %) and stronger CD (≈0.78) while simultaneously providing intrinsic suppression of unwanted background and crosstalk. Its selective spin-routing behaviour makes it a promising candidate for mid-infrared applications including spin-resolved information encoding, polarimetric scene separation, and polarization-division multiplexing.

The use of mirror-enantiomeric unit cells enables passive background suppression without requiring multilayer cascades or external tuning.

Table 6.2. Comparison table for Proposed Spin-Multiplexed Reflective Metalens Against Reported Works

Reference	Configuration/ Multiplexing type	Bandwidth (nm)	Diffraction efficiency (%)	CD	Background/ crosstalk suppression
[177]	Dielectric polarization multiplexed meta-hologram	-	51	0.60	Moderate
[178]	Three-channel spin-multiplexed metasurface	100	25	0.3	Low
[179]	Dual-wavelength achromatic metalens	-	35	0	-
[180]	Dual-band transmission metasurface for spin selection	100	15	0.3	High
This work	Wideband spin multiplexed reflective metasurface	70	76	0.78	High

Further improvements in diffraction efficiency and background suppression can be obtained by targeted electromagnetic optimizations that preserve the enantiomeric chiral mechanism. First, minor tuning of the dielectric spacer thickness can adjust the near-field coupling between the Ω resonators and the metallic ground plane, improving impedance matching for the cross-polarized channel and reducing unwanted reflective leakage. Second, selectively increasing dissipative loss only in the absorbing enantiomers can deepen background suppression without degrading the converting units. Finally, performing co-optimization using adjoint or inverse-

design methods enables simultaneous maximization of diffraction efficiency and circular dichroism while respecting fabrication constraints. Collectively, these approaches provide practical pathways to higher throughput and clear focal spots while maintaining intrinsic spin selectivity. While the current implementation is passive and static, future directions may involve incorporating tunable or nonlinear materials to achieve dynamic polarization control, real-time beam steering, or adaptive photonic logic. The general design principle—encoding polarization-dependent functionality through spatial meta-atom arrangement—offers a scalable pathway toward intelligent spin-photonic devices.

6.4. Summary:

This chapter has presented a spin-multiplexed reflective metalens that unifies polarization-selective absorption, spin conversion, and wavefront shaping within a compact Au–SiO_2–Au trilayer platform. By utilizing Ω-shaped and mirror-Ω-shaped resonators as enantiomeric meta-atoms, the device achieves strong spin discrimination, steering left- and right-circularly polarized beams to distinct focal spots while effectively suppressing background reflections. Numerical simulations confirm high circular dichroism, broadband spectral tolerance, and diffraction efficiencies exceeding 75%, demonstrating the robustness of the design across the mid-infrared regime. The metasurface further supports dual-spin operation, allowing simultaneous two-channel focusing with negligible overlap, an essential capability for polarization-multiplexed imaging and optical information routing.

Overall, the results establish a multifunctional reflective metasurface that bridges chiral light–matter interaction with lensing functionality. The demonstrated approach provides a scalable pathway toward compact, integrated platforms for advanced photonic applications, including

secure imaging, optical communication, and sensing, where precise spin control and spatial separation are of central importance.

7

CHAPTER

All-Dielectric Meta-Coded Firewall for Polarization-Selective Optical Authentication

- *Introduces an all-dielectric chiral metasurface operating under normal incidence, shifting the focus from earlier reflection-based architectures to a transmission-dominant platform.*
- *Demonstrates dual circular dichroism (CD) resonances with peak values 0.85 at 1239 nm (RCP) and -0.93 at 1250 nm (LCP), enabling spin-selective optical gating.*
- *Establishes a 41 × 41 metasurface array that encodes a hidden "V"-shaped pattern, which becomes visible only under the correct polarization–wavelength conditions (LCP at 1250 nm, RCP at 1239 nm).*
- *Provides dynamic tunability of the optical response via graphene Fermi energy modulation, enabling reconfigurable spectral–polarization logic and establishing a robust meta-coded optical firewall for secure authentication, friend-or-foe identification, and photonic encryption in communication and defence systems.*

7.1. INTRODUCTION:

In the preceding chapters, the focus was placed on reflection-based chiral metasurfaces, where spin-selective absorption and wavefront control were harnessed for applications ranging from dichroism engineering to spin-multiplexed imaging and encryption. While these reflective platforms demonstrated strong circular dichroism (CD), perfect absorption, and spin-resolved focusing, their reliance on reflective geometries naturally restricted the range of functionalities. Many real-world scenarios, particularly in optical communication and secure tagging, demand devices that operate in transmission mode, enabling selective visibility and polarization-gated information display without the need for bulky reflective backplanes.

In the rapidly advancing landscape of electromagnetic security, optical communication, and defence photonics, the demand is shifting from invisibility cloaks to intelligent optical systems that can dynamically reveal or conceal information depending on polarization and wavelength. Rather than suppressing visibility altogether, metasurfaces can act as gatekeepers that permit information access only under pre-defined illumination conditions (polarization and spectral channels) while maintaining concealment otherwise [167,168,170,181,182]. This transition from reflection to transmission opens new avenues for compact, scalable, and spectrally agile photonic devices.

Recent progress in chiral metasurfaces has enabled unprecedented spin-selective wave manipulation, where left- and right-circularly polarized light (LCP and RCP) are treated asymmetrically [13,20,74,183,184]. Such spin discrimination provides a foundation for polarization-gated encoding schemes, critical for applications like friend-or-foe identification, secure authentication, and anti-counterfeiting. Unlike traditional cloaking approaches that demand bulky materials or complex tunable structures [185–187], meta-coded transmission

surfaces composed of subwavelength resonators provide a lightweight, integrable solution for polarization-domain encryption [9,108,188–192]. By exploiting asymmetric transmission and dual-wavelength selectivity, they enable encoded patterns to remain concealed under general illumination but revealed under precisely defined spin–spectral conditions.

In this chapter, we present a transmission-based chiral meta-coded firewall that marks a natural extension of the concepts established in earlier reflective metasurface studies. The device consists of a 41 × 41 array of double-sided semicircular-ring meta-atoms, engineered to produce strong dual-wavelength CD: reflecting LCP at 1250 nm and RCP at 1239 nm, while remaining transparent otherwise. This design not only enhances spin selectivity but also enables dual-spin operation within the same metasurface—an ability rarely demonstrated in prior single-sided architectures. The encoded "V"-shaped image is revealed exclusively under the appropriate polarization–wavelength combinations, ensuring high-contrast, polarization-dependent visibility.

Furthermore, the optical response of the metasurface can be dynamically tuned via graphene Fermi energy modulation, providing reconfigurable spectral–polarization logic for real-time applications. By combining amplitude and phase control in transmission, the proposed strategy introduces a secure, physically encrypted optical mechanism ideally suited for friend-or-foe identification, authentication, and situational awareness in photonic communication systems.

7.2. Concept and Design of Spin-Selective Meta-Firewall:

Fig. 7.1 illustrates the concept of a spin- and wavelength-selective optical firewall using a chiral metasurface integrated with a tunable graphene layer. The metasurface consists of an array of chiral meta-atoms, designed to reflect LCP light at 1239 nm and RCP at 1250 nm while

remaining transparent to other off-resonant illumination. The visibility of the encoded image is further modulated by the Fermi level (E_f) of the graphene layer.

Fig. 7.1(a) shows the illumination of the drone covered with uniform surface imparting no identifiable pattern. Whereas Fig. 7.1(b, c) demonstrate the illumination of the drone enclosed with the metasurface. In Fig. 7.1(b) when the surface is illuminated with RCP at 1239 nm or LCP at 1250 nm, the metasurface selectively reflects the encoded "V" pattern, enabling positive identification. In contrast, Fig. 7.1(c) shows the response under all other wavelengths and spin states. In this case, no recognizable image is formed, and the surface remains effectively concealed. This confirms that the system can dynamically toggle between identification and concealment states, offering a reconfigurable platform for secure optical recognition and polarization-dependent encryption.

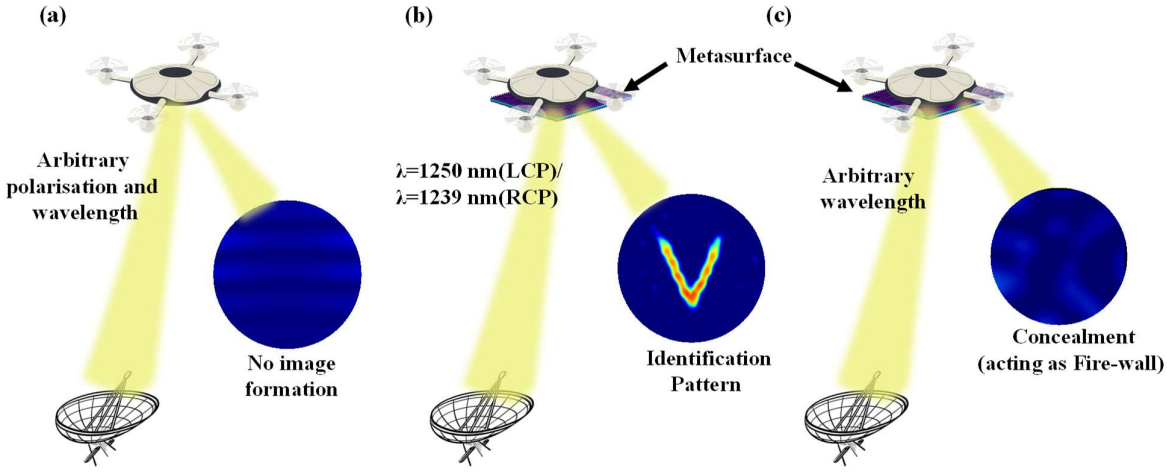

Fig. 7.1 Schematic diagram of a chiral metasurface-based optical firewall. (a) Electromagnetic interrogation of a uncoated drone without any metasurface showing no encoded response. (b) Drone coated with metasurface showing "V" image under LCP at 1250 nm or RCP at 1239 nm enabling authentication. (c) Metasurface-coated drone showing no image under all other conditions ensuring metasurface acts as a fire-wall for concealment of drone.

The design of a phase-engineered metasurface for structured image formation is based on the principle of wavefront reconstruction through coherent back-propagation. The metasurface comprises a 41×41 array of meta-atoms arranged with a uniform lattice periodicity of 890 nm, yielding a total lateral extent of 36.5 µm. Each element imparts a local phase shift ϕ (x_m, y_m) to the reflected wave. The far-field E_s (x, y, z) at an arbitrary observation point (x, y, z) can be expressed as the coherent superposition of secondary spherical wavelets emitted from the metasurface elements[193]:

$$E_s(x,y,z) = \frac{1}{i\lambda}\sum_{m=1}^{M} A(x_m,y_m)cos\theta_m \frac{e^{i[k_0 r_m+\varphi(x_m,y_m)]}}{r_m^2} \quad (7.1)$$

Here, $r_m = \sqrt{(x-x_m)^2+(y-y_m)^2+z^2}$ is the distance from the m[th] element to the field point, θ_m denotes the angle between the surface normal and the vector to the observation point (accounting for the inclination factor), and A(x_m, y_m) represents the amplitude response of each meta-atom.

To determine the required phase distribution, inverse field propagation(back-propagation) strategy is adopted in which the desired field at the focal plane is prescribed in the form of a binary "V"-shaped pattern[194–196]. The metasurface is then designed such that the reflected field contributions from all meta-atoms interfere constructively at these focal points. Mathematically, this is achieved by summing spherical wavefronts emanating from each active pixel in the target image, treated as virtual point sources:

$$E(x,y) = \sum_{n=1}^{N_f} \exp\left(-ik_0\sqrt{(x-x_n)^2+(y-y_n)^2+z^2}\right) \quad (7.2)$$

where (x_n, y_n, z) are the coordinates of each "on" pixel in the target pattern and N_f denotes the number of such pixels.

The required local phase shift at each metasurface position is obtained from the argument of the total field:

$$\varphi(x, y) = \arg[E(x, y)] \tag{7.3}$$

Fig. 7.2 illustrates the computed phase profile, obtained using this procedure for a focal distance z = 50 μm and an operating wavelength of 1250 nm under left-circularly polarized (LCP) illumination. It is worth noting that this formulation neglects the inclination factor $cos\theta_m$ and assumes a constant amplitude response for all meta-atoms. These assumptions are used to simplify the design without significantly impacting accuracy for moderate deflection angles. This approach provides a computationally efficient and physically intuitive method for designing phase-only metasurfaces that project arbitrary structured images in free space.

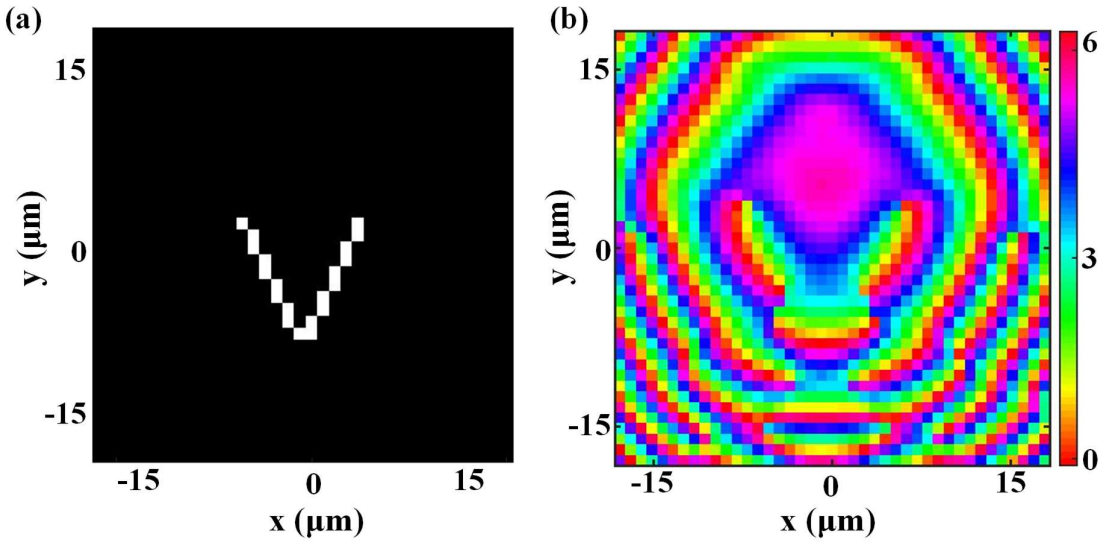

Fig. 7.2 (a) Target image (b) Phase profile of the 41x41 metasurface to generate the target image.

7.3. Meta-Atom Design and Spin-Selective Response:

To realize the desired spin-selective visual response, each meta-atom within the metasurface is engineered to exhibit strong spin selective reflection at specific wavelength while maintaining high transmission for other wavelengths. This chiral asymmetry is achieved by carefully breaking both in-plane mirror symmetry and rotational symmetry, ensuring non-zero circular dichroism[96,97]. Fig. 7.3 depicts the structural arrangement of the proposed meta-atom. The designed chiral meta-atom is an all-dielectric structure. The top and bottom layer made of Si, which consists of three Semi-Circular Rings (SCRs) is the key principle behind this conception. Fig. 7.3(b) shows the built of the three SCR with parameters height h_1 = 305 nm, h_2 = 190 nm, h_3 = 30 nm, orientation angles α_1 = 5°, α_2 = -10°, α_3 = 115° and width w_1 = 55 nm, w_2 = 95 nm, w_3 = 90 nm of the designed SCR respectively. The substrate is composed of TiO_2 of height H_1 = 200 nm and the graphene layer of height H_2 = 10 nm is induced between the bottom layer and the substrate to further increase the degree of freedom for spin selectivity of the meta-atom.

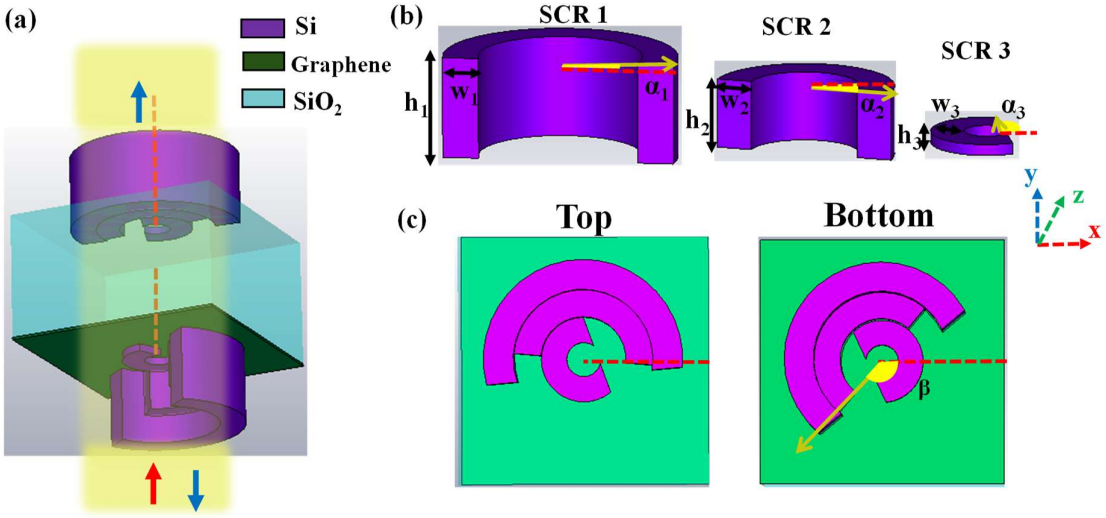

Fig. 7.3 Structural design of the chiral meta-atom. (a) 3D view of the meta-atom (b) Arrangement of the three semicircular rings being part of the top and bottom resonator (c) 2D view of the top and bottom resonators.

The bottom layer is the replica of top layer with the orientation angle β = 135° as shown in Fig. 3(c). The varying heights, widths and alignment angles of these SCRs provide the necessary asymmetric factor leading to the strong CD.

The dielectric functions of TiO_2 given by Devore et al.[197] and for Si is given by Pierce and Spicer et al.[198] have been used. The incorporation of a graphene layer beneath the chiral meta-atom plays a critical role in enabling active and tunable control over the optical properties of the metasurface. Graphene, a two-dimensional material with extraordinary electronic and optical tunability, introduces a dynamic component into an otherwise passive resonant system. As active component of the metasurface, graphene has a tunable surface conductivity which can be described by the well-known Kubo model. Its conductivity is mainly determined by the interband and intraband transition, which can be expressed as[199,200]:

$$\sigma = \sigma_{intra} + \sigma_{inter}$$

$$= \frac{ie^2 k_B T}{\pi\hbar^2 (w + i\tau^{-1})}\left[\frac{E_f}{k_B T} + 2\ln\left(\exp\left(-\frac{E_f}{k_B T}\right) + 1\right)\right] + \frac{ie^2}{4\pi\hbar}\ln\left[\frac{2|E_f| - (w + i\tau^{-1})\hbar}{2|E_f| - (w + i\tau^{-1})\hbar}\right] \quad (7.4)$$

In equation 7.4, ω represents the angular frequency, T is the temperature, e corresponds to the elementary charge, $\hbar$ is the reduced Planck constant, k_B represents the Boltzmann constant, E_f is the Fermi level (chemical potential), which is determined by the carrier concentration and τ represents the relaxation time. Here, we assume T = 300K, τ = 1ps, and the Fermi level varies between 0 eV and 1 eV. The meta-atom has two different states, that is the "on" and "off" state. When the single layer graphene obtains high conductivity due to electrical doping (E_f = 1 eV), the metasurface is in “on” state, which works as a chiral device. When graphene is not doped E_f = 0 eV, the metasurface can be seen as an ordinary surface and is in the "off" state, both LCP and RCP waves will be totally transmitted. To verify the effectiveness of the proposed spin-

selective metasurface, full-wave simulations were conducted using CST Microwave Studio in the Finite Element Method domain. A normally incident circularly polarized plane wave is used as the excitation source. The boundary conditions are set to open (add space) in z direction and periodic in x and y direction.

A key feature of the proposed metasurface is its dual-sided structural configuration, which plays a central role in enabling the dual circular dichroism (CD) peaks with opposite handedness. Unlike single-layer or planar chiral designs, the dual-sided architecture allows for asymmetric coupling between the incident light and the resonant elements on each side of the structure. This vertical asymmetry—combined with the chiral geometry of the meta-atoms—creates distinct interaction pathways for left- and right-handed circularly polarized (LCP and RCP) light. As a result, LCP light is strongly reflected at wavelength 1250 nm, while RCP light exhibits a separate resonance at a slightly shorter wavelength 1239 nm. The presence of two independent CD peaks with opposite spin preference is thus a direct consequence of the dual-surface asymmetry, which breaks mirror symmetry both in-plane and out-of-plane.

Fig. 7.4 represents the transmission and reflection amplitudes of the meta-atom for the 'on' and 'off' states of meta-atom for the incident LCP and RCP light. Simulated results show that the when the structure is in 'on' state i.e E_f =1 eV, there is sharp decline of the co-polarised transmission amplitude(t_{ll}) and increase in cross polarized component of reflected light(r_{rl}) under LCP incidence at 1250 nm whereas, for RCP incidence the transmission(t_{rr}) declines and cross reflection(r_{lr}) exhibits a narrowband peak at 1239 nm as shown in Fig. 7.4(a, b). Further for the structure with E_f=1 eV, the sharp decline of the transmission amplitude and increase in cross polarized component of reflected light is greatly reduced either for incident LCP or RCP light, implying the meta-atom is in 'off' state as shown in Fig. 4(c, d). Whereas, at 1239 nm

RCP reflection spectrum exhibits a narrowband peak and the RCP reflection remains near-zero. Results show by altering the fermi level E_f of graphene the resonance peak can be controlled giving an extra degree of freedom for the concealment or identification of the information. This asymmetric spectral behavior is used to modulate the image visibility in wavelength and polarization resolved manner.

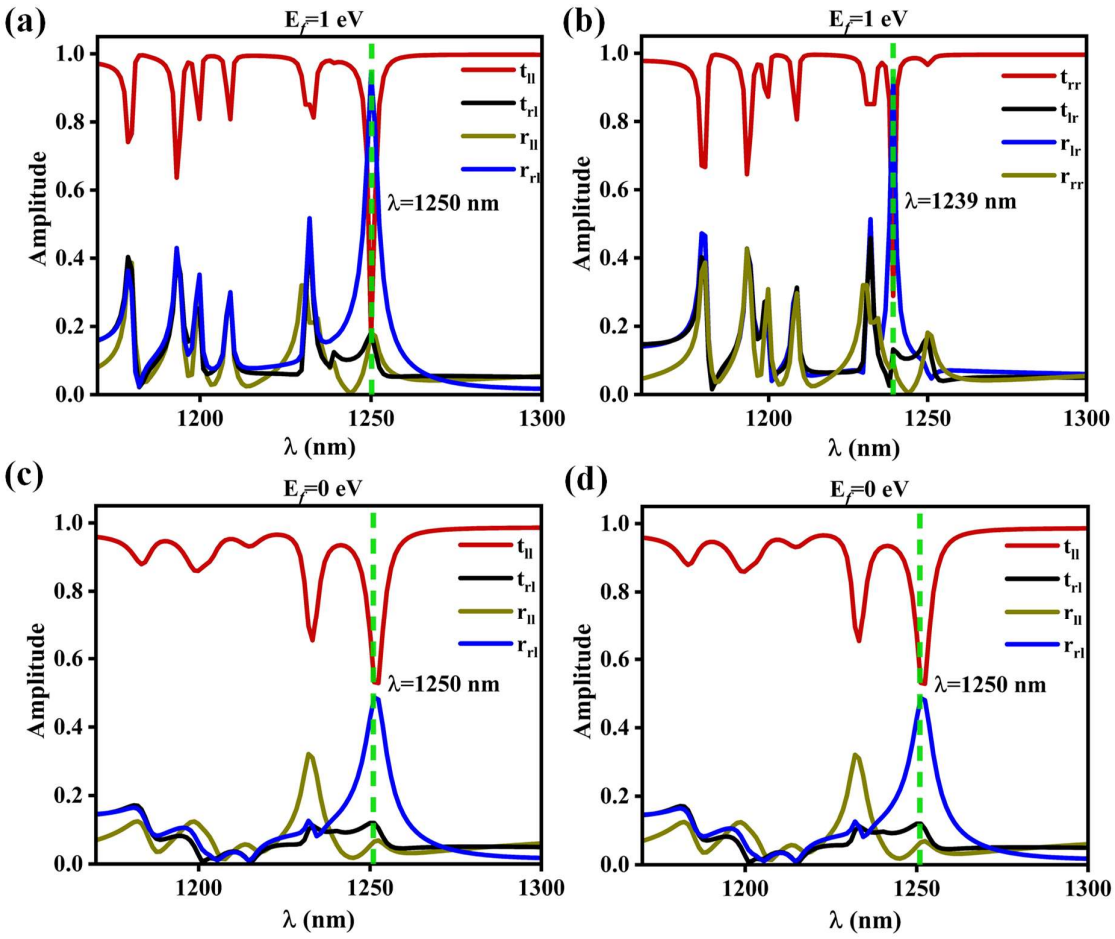

Fig. 7.4 The transmission and reflection amplitudes of the chiral meta-atom for the incident (a) LCP and (b) RCP when E_f=1 eV. The transmission and reflection amplitudes of the chiral meta-atom for the incident (c) LCP and (d) RCP when E_f=0 eV.

The chirality-induced transmission contrast for the 'on' and 'off' state of the meta-atom enables strong dual and opposite handedness CD peaks. The spin-selective scattering can be characterized by the transmission and reflection coefficients t_{ll}, t_{rl}, t_{rr}, t_{lr}, r_{ll}, r_{rl}, r_{rr}, r_{lr} where[201]:

$$CD = (t_{ll}^2 + t_{rl}^2) - (t_{rr}^2 + t_{lr}^2) \tag{7.5}$$

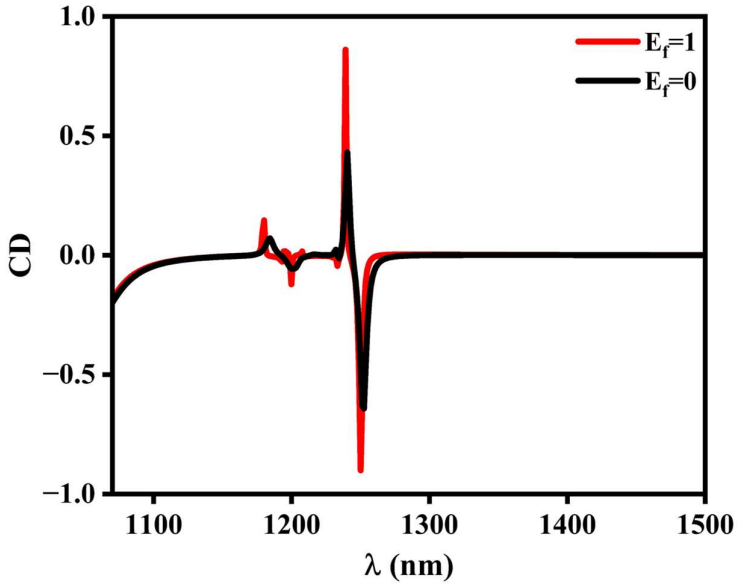

Fig. 7.5 Display of the dual CD peaks for different fermi energy of graphene layer.

Fig. 7.5 represents the dual CD peaks with opposite handedness for different state of the structure. The CD reaches value of -0.93 at 1250 nm and 0.85 at 1239 nm for E_f=1 eV. Whereas for E_f=0 eV CD values reduce to -0.54 at 1250 nm and 0.38 at 1239 nm. The variation in the Ef directly impacts the complex permittivity of graphene and thus its interaction with the localized electromagnetic fields of the meta-atom. As a result, both the amplitude and spectral sharpness of the circular dichroism (CD) response become tunable. At higher E_f, the resonance is stronger and more spectrally confined, leading to higher CD peak values and narrower linewidths, while at lower E_f, increased damping causes the peaks to broaden and weaken,

offering dynamic control over both visibility and spectral selectivity. The dual peaks with opposite chirality of the meta-atom ensure that the structure is not limited to single polarization state(LCP/RCP) but works for both polarization states of the incident light.

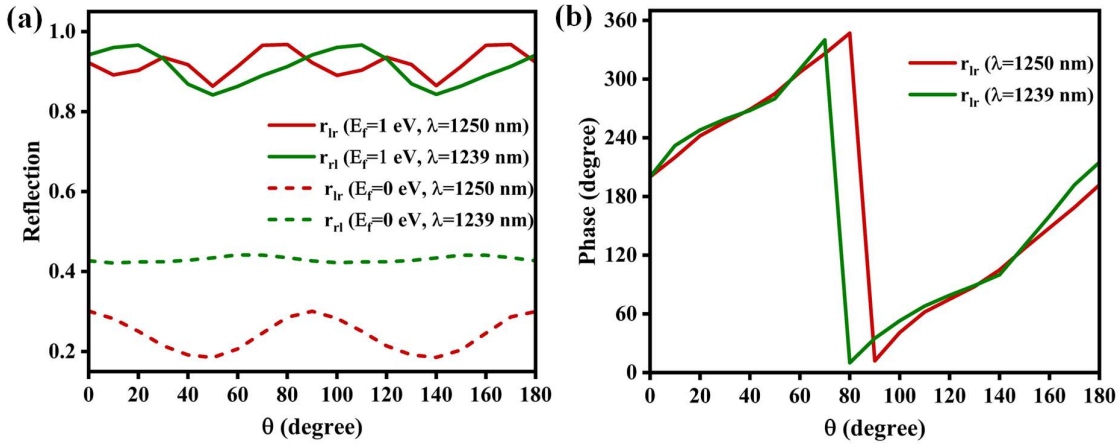

Fig. 7.6 (a) The cross polarized reflection amplitudes for E_f=1 and E_f=0 of the graphene layer. (b) The phase profile of r_{rl} and r_{lr} at λ=1250 nm and λ=1239 nm respectively while rotating the meta-atom.

To achieve precise spin-dependent optical control, a discrete set of meta-atoms have been developed by rotating the chiral meta-atom. Each meta-atom is designed to exhibit strong reflection at the designated wavelength, enabling spatial encoding of the desired image. The controlled rotation allows modulation of the reflected phase across the metasurface while maintaining consistent amplitude response. Fig. 6(a) illustrates the variation of cross reflection amplitudes r_{rl}, r_{lr} with the rotation the meta-atom at λ=1250 nm and λ=1239 nm for different fermi energy E_f=1 and E_f=0. The results show that the values of r_{rl}, r_{lr} remain nearly constant (~0.9) and high with the rotation of the structure for E_f=1 whereas for E_f=0 eV extremely low being r_{rl}~0.4 and r_{lr}~0.3. Complete phase coverage is achieved for both the cross-polarized r_{rl} component at λ=1250 nm and the cross-polarized r_{lr} component at λ=1239 nm through controlled rotation of the chiral meta-atom structure, with only a minor phase offset observed,

as shown in Fig. 7.6(b). This confirms that the metasurface, originally designed to encode a "V" image in reflection under LCP incidence at λ=1250 nm, can similarly operate under RCP incidence at λ=1239 nm, thereby enabling dual-polarization functionality.

7.4. Results and Discussion:

7.4.1. Field Propagation and Pattern Evaluation:

To verify the effectiveness of the proposed spin-selective metasurface, full-wave simulations were conducted using the FDTD method. Fig. 7.7(a) displays the reflected normalized electric field intensity distribution from the metasurface plane under LCP illumination at 1250 nm at focal distance z = 50 μm when the E_f is kept 1 eV. As expected, the "V" pattern becomes clearly visible due to the high reflectance from meta-atoms encoded within the image region, while the surrounding background remains non-reflective. This creates a high-contrast spin-gated visual signature. In contrast, as shown in Fig. 7.7(b), when the metasurface is illuminated with RCP light, the reflected field shows no recognizable image, confirming the helicity-selective response and optical firewall behavior. The spectral dependence of the image visibility is evaluated by varying the incident wavelength. As shown in Fig. 7.7(c,d), the pattern emerges only near 1250 nm, where LCP reflectance is maximized. The image contrast deteriorates rapidly away from resonance wavelength, demonstrating a narrowband chiral window for secure optical access. Similarly, under RCP illumination at 1239 nm the normalized reflected electric field intensity distribution showcase the "V" pattern at focal distance z = 50 μm while under LCP illumination at this wavelength no image is formed as shown in Fig. 7.7(e,f).

To further analyze the metasurface's optical behavior beyond the aperture, the simulations are performed for the propagation of the reflected field(r_{rl}) at various distances from the metasurface plane at λ = 1250 nm. Fig. 7.7(g) shows the intensity profile at different focal

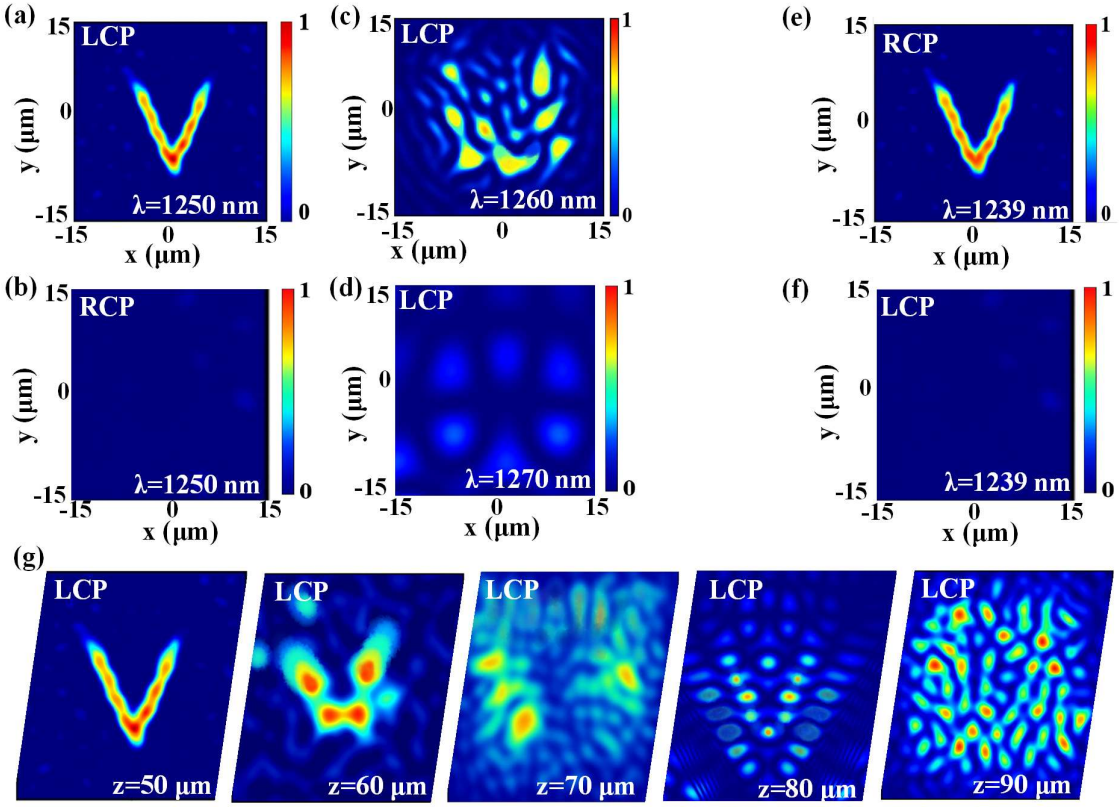

Fig. 7.7 Results demonstrating spin-selective image projection and concealment. (a) Reflected "V" image at a distance of 50 μm under LCP illumination (authentication mode) while (b) no reflection/image formation under RCP excitation at λ = 1250 nm. (c) Distortion of image at λ = 1260 nm and (d) no focusing of field happening at further wavelengths. Similarly (e) "V" image under RCP illumination (authentication mode) while (f) no reflection/image formation under LCP excitation at λ = 1239 nm. (g) Additional simulated intensity patterns at z = 50, 60, 70, 80 and 90 μm illustrating field evolution from the aperture to the focal plane.

distance from the metasurface plane. The "V" image remains sharp and well-defined, indicating strong constructive interference from the phase-aligned reflective meta-atoms at z = 50 μm. As the observation distance increases from the focal plane, the image undergoes gradual blurring due to diffraction and spatial spreading of the wavefront. Despite this degradation, the pattern remains recognizable up to a moderate imaging distance, highlighting the viability of

the system for near-field to intermediate-range optical recognition. This confirms that the encoded image is not only localized but also robust to short-range propagation under spin-selective excitation. In contrast, under RCP illumination, the metasurface remains largely transparent, and the reflected intensity is negligible at all distances. Further, when the E_f is kept at 0 eV of the graphene layer no image is formed under LCP/RCP illumination at the resonance wavelength as shown in Fig. 8. These results validate the metasurface function as a spin-gated visual encoding platform, where both polarization and wavelength must match specific conditions to reveal the hidden pattern. The system thus acts as a meta-coded optical firewall, suitable for friend-or-foe identification, encrypted tagging, and secure signaling.

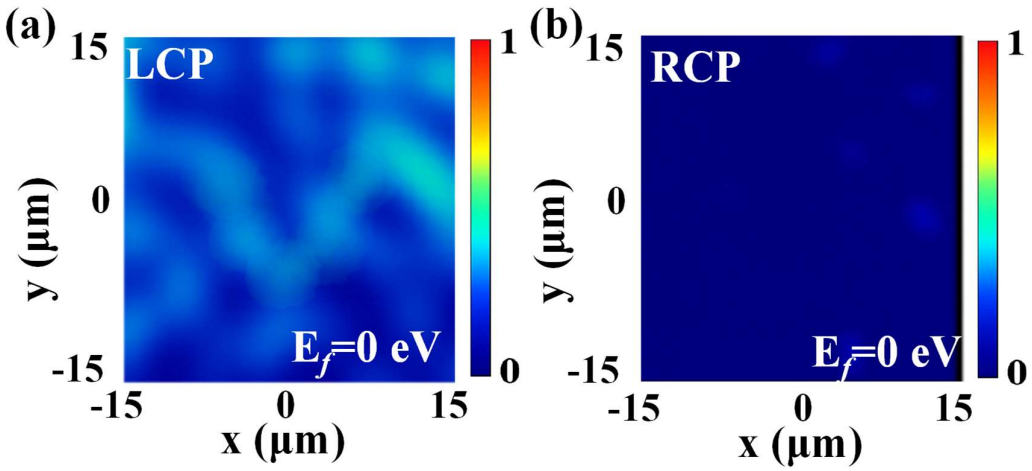

Fig. 7.8 Full concealment of the object at all wavelengths when E_f=0 eV for incident (a) LCP and(b) RCP illumination.

To quantify the image fidelity with distance, the image intensity distribution along the propagation axis is extracted. As shown in Fig. 7(f), the "V" image exhibits high contrast within 40–60 μm but gradually fades beyond 80 μm due to diffraction-limited spreading. This defines a spin- and distance-constrained secure viewing window for image detection.

These results demonstrate that the proposed metasurface does not merely reflect polarization-filtered light but actively encodes and projects a readable image, which is accessible only through precise matching of spin, wavelength, and observation geometry—the fundamental principle of the meta-coded optical firewall.

7.4.2. Performance Metrics:

To evaluate the effectiveness of the spin-gated metasurface beyond visual inspection, key optical performance metric i.e. diffraction efficiency has veen analysed. The diffraction efficiency (η) is defined as the ratio of reflected power directed into the encoded "V" pattern to the total incident power under LCP illumination[202]:

$$\eta = \frac{P_{image}}{P_{total}} \tag{6}$$

Here, P_{image} is the integrated power in the bright regions of the reflected image (e.g., within the "V"), and P_{total} is the total input power incident on the metasurface. Simulations indicate that the metasurface achieves a high diffraction efficiency $\eta = 60.6\ \%$ and image visibility crucial for secure detection.

7.5. Summary:

In this chapter, a reconfigurable transmission-based chiral metasurface has been demonstrated as a spin-selective optical firewall for secure, polarization-dependent image projection. The device, composed of a 41 × 41 array of chiral meta-atoms, is engineered to project a distinct "V"-shaped pattern that appears only under left-handed circularly polarized light at 1250 nm and right-handed circularly polarized light at 1239 nm. By achieving full 2π phase coverage through orientation modulation of the meta-atoms, the metasurface enables dual-polarization, dual-wavelength operation without requiring geometric variation, ensuring compact and simple

design. The proposed system exhibits strong circular dichroism at both resonance wavelengths while remaining optically silent under all other illumination conditions, thereby ensuring selective visibility and concealment. Importantly, active tunability is introduced through modulation of the graphene Fermi energy, which allows dynamic switching between visible and concealed states. This adaptability provides an additional layer of security, making the platform programmable for real-time applications.

Overall, the results establish a compact, scalable, and polarization-gated metasurface platform that extends the thesis narrative from reflection-based chiral systems to transmission-based security architectures. The demonstrated optical firewall offers promising applications in secure photonic tagging, anti-counterfeiting measures, and friend-or-foe recognition, underscoring its relevance in advanced communication and defense-oriented photonics.

8

CHAPTER

Conclusion, Future Scope and Social Impact

- *This chapter provides an overview of the research conducted in this thesis.*
- *It further presents a brief discussion of the key conclusions drawn from the results.*
- *Finally, it identifies possible avenues for future research and examines the societal impacts of the research work.*

8.1. CONCLUSION

This thesis presents a comprehensive investigation into the design, analysis, and application of optical metasurfaces, advancing from fundamental principles to multifunctional chiral architectures capable of complex light manipulation. The research establishes a unified framework for achieving amplitude, phase, and polarization control using subwavelength nanostructures, thereby bridging the gap between conventional photonic components and next-generation flat-optical systems.

Beginning with achiral dielectric metasurfaces, the work demonstrated efficient phase modulation and broadband achromatic focusing through low-aspect-ratio designs inspired by natural optical systems. By integrating diverse dielectric materials and achieving full 2π phase coverage, these metasurfaces provide scalable, fabrication-friendly platforms for compact imaging and optical processing.

Building upon this foundation, the study transitioned toward chiral and polarization-sensitive metasurfaces that leverage geometric asymmetry, multilayer hybrid compositions, and extrinsic chirality. The introduction of perovskite-based and metallic–dielectric–metal architectures enabled tunable circular and linear dichroism across visible to mid-infrared wavelengths. These designs exhibited high sensitivity to environmental refractive index variations, demonstrating their promise for biosensing and polarization-controlled detection applications.

A major advancement was achieved through the development of strongly chiral metasurfaces operating under normal incidence, including concentric semi-circular ring and Ω-shaped resonator configurations. These architectures combined strong circular dichroism, near-perfect absorption, and angular stability, offering versatile control over spin-dependent light

propagation. Their ability to encode optical information and achieve spin-multiplexed focusing highlights their relevance for secure imaging, encryption, and optical communication systems.

Finally, the realization of a transmissive chiral metasurface functioning as a meta-coded optical firewall exemplified the convergence of material engineering, geometric design, and polarization selectivity for security-oriented photonic technologies. The device achieved dual circular dichroic resonances, dynamic tunability, and polarization-dependent visibility of encrypted patterns, demonstrating a novel approach to secure authentication and anti-counterfeiting.

Overall, this thesis establishes a systematic progression from achiral to multifunctional chiral metasurfaces, integrating concepts of spin–photon interaction, broadband dichroism, and wavefront shaping. The developed metasurfaces not only deepen the understanding of light–matter interaction at the nanoscale but also pave the way for practical applications in flat optics, polarization-multiplexed communication, biosensing, and defence-related photonic security. Through innovative geometrical design and material integration, the work contributes to the evolution of metasurfaces as compact, reconfigurable, and highly efficient building blocks for next-generation photonic technologies.

8.2.FUTURE SCOPE OF THE WORK

While the designs and results presented in this thesis have contributed significantly to the understanding and application of metasurfaces, there remain several promising directions for future research:

- Integration with Tunable Materials: Incorporating phase-change materials (e.g., GST), liquid crystals, or 2D materials beyond graphene could enable dynamic and real-time modulation of CD, absorption, and phase. Such integration would expand functionalities toward adaptive communication networks and programmable optical encryption.
- Integration with Photonic Circuits: Embedding metasurfaces into on-chip photonic circuits can open avenues for miniaturized communication systems, integrated quantum optics, and compact biosensors.
- Advanced Security Applications: Building upon the meta-coded firewall concept, metasurfaces can be explored for multi-layered security schemes, where information is encoded simultaneously in polarization, wavelength, angle, and orbital angular momentum channels. This multidimensional encryption can substantially enhance data protection.
- Biomedical Implementation: Translating the biosensing designs into practical diagnostic tools requires experimental validation with real biological samples. Developing metasurface-based lab-on-chip devices for point-of-care applications could have transformative impacts in healthcare.
- Quantum and Nonlinear Regimes: Extending metasurface functionalities into quantum optics (e.g., photon spin manipulation, entangled photon routing) and nonlinear processes (e.g., harmonic generation under spin-selective excitation) represents a fertile ground for next-generation photonic technologies. A detailed review of existing literature will be performed to enhance knowledge and understanding of the current topic.

8.3.SOCIAL IMPACT

The research work presented in this thesis extends beyond academic advancement, offering meaningful contributions to technological innovation and societal well-being. By addressing global priorities such as secure communication, accessible healthcare, sustainable energy, and ethical production, the outcomes of this work resonate strongly with several United Nations Sustainable Development Goals (SDGs). The key social and sustainable impacts are summarized as follows:

1. Secure Communication Networks: The demonstrated chiral metasurfaces and meta-coded firewalls enable polarization- and wavelength-gated encryption, ensuring safer and more efficient optical communication. By enhancing data protection and infrastructure resilience, these technologies support SDG 9 (Industry, Innovation and Infrastructure) and SDG 16 (Peace, Justice and Strong Institutions) through secure digital systems.
2. Healthcare and Diagnostics: Perovskite-based metasurface biosensors offer compact, highly sensitive, and cost-effective platforms for early detection of hemoglobin, glucose, and cancer biomarkers. These innovations enhance healthcare accessibility and diagnostic precision, advancing SDG 3 (Good Health and Well-being) and SDG 9 (Industry, Innovation and Infrastructure).
3. Data Protection and Anti-Counterfeiting: Spin-selective image projection and polarization-multiplexed authentication provide new routes for secure tagging and counterfeit prevention. By improving authenticity and transparency across supply chains, these methods promote SDG 12 (Responsible Consumption and Production) and foster innovation aligned with SDG 9.

4. Energy and Sustainability: The metasurface designs achieve strong light–matter interaction and high absorption in ultra-thin layers, reducing material use and improving energy efficiency. These advances contribute to sustainable device design and renewable energy integration, supporting SDG 7 (Affordable and Clean Energy) and SDG 12.
5. Integration into Next-Generation Technologies: The compact and multifunctional metasurfaces developed here enable next-generation platforms such as quantum communication, photonic computing, and secure IoT systems. By lowering energy demands and system footprint, they drive SDG 9 (Industry, Innovation and Infrastructure) and SDG 13 (Climate Action).

In summary, this research is positioned to advance the field of metasurfaces with broad technological and societal implications. The ability to engineer achiral and chiral metasurfaces for applications ranging from secure optical communication and biosensing to imaging and information encryption highlights their transformative potential. These innovations hold promise for improving healthcare diagnostics, strengthening defence and authentication systems, enabling sustainable photonic technologies, and expanding the capabilities of modern communication networks. Ultimately, the outcomes of this thesis underscore the potential of metasurfaces not only to enrich scientific knowledge but also to enhance quality of life, security, and connectivity at a global scale.